



HORIZON 2020

**HORIZON 2020 RESEARCH AND INNOVATION
FRAMEWORK PROGRAMME OF THE
EUROPEAN ATOMIC ENERGY COMMUNITY**

Nuclear Fission and Radiation Protection 2018 (NFRP-2018-4)

Project acronym: **SANDA**

Workpackage N°: **WP5**

Identification N°: **D5.11**

Type of document: **Deliverable**

Title: **Report on integral experiments at the LR-0 reactor**

Dissemination Level: **PU**

	Name	Partner	Date	Signature
Prepared by:	Michal Kostal	7	10-06-2024	
WP leader:	Robert Jacqmin	3	10-06-2024	
IP Co-ordinator:	E. González	1	10-06-2023	

Report on Integral Experiments at the LR-0 Reactor

Prepared by:

M. Kostal, E. Losa, T. Peltan, M. Schulc

Research Centre Rez, Hlavni 130, Husinec-Rez 250 68, Czech Republic

Contents:

Contents:.....	3
Introduction:	4
1 LR-0 reactor	5
1.1 Characterization of critical parameter	7
1.2 Characterization of the neutron flux profile	10
1.3 Characterization of neutron and gamma spectrum	13
1.4 Characterization of the fission density profile.....	24
2 Reference neutron benchmark field for dosimetry cross section measurements	30
3 Spectrum averaged cross-sections	37
4 Pile noise experiment.....	39
4.1 Detectors and acquisition systems	39
4.2 Irradiation runs and flux monitoring	40
4.3 Power spectral densities and associated uncertainties	43
4.4 Analytical model, data fitting and reproducibility.....	44
4.5 Impact of the detector's distance in the reflector.....	45
4.6 Kinetic parameters of LR-0 reference core configuration.....	47
4.7 Conclusions and outlooks.....	47
5 Measurements of spectrum-averaged cross sections in high-purity graphite moderation environment.....	49
5.1 Reaction rate measurement.....	53
5.2 The effect of graphite on the neutron flux distribution	55
5.3 Fast neutron spectrum evaluation	56
5.4 Experiment with single graphite insertion.....	61
5.5 Mapping of the neutron flux distribution in the graphite prism	62
5.6 MCNP calculation and reaction rate determination	63
6 Summary	70
7 References.....	71
Appendix: gamma spectrometry data.....	77
Appendix: data fitting results	83

Introduction:

A reference neutron field is defined as a permanent reproducible neutron field with well-defined neutron fluence rate and neutron energy spectrum. The standard reference field has neutron spectrum characterized employing neutron spectrum measurements by means of time-of-flight measurements. Historically, only one standard neutron reference field was established, $^{252}\text{Cf}(\text{s.f.})$. In 2017, $^{235}\text{U}(\text{n}_{\text{th}}, \text{fis})$ was included among neutron standards and became secondary neutron standard.

Standard neutron fields are less rigorously characterized, but still acceptable as a measurement reference by a community of users. This work reports on the development of a reference neutron benchmark field in a special core placed in the LR-0 reactor. Fission density distribution across the driver core was validated to confirm the spatial distribution of the neutron field. Neutron and gamma spectra were precisely measured using stilbene spectrometry in this reference neutron benchmark field. It was observed that neutron spectrum above 6 MeV is nearly identical with ^{235}U prompt fission neutron spectrum (PFNS), and it was confirmed that the gamma reactions have a negligible contribution to the measured neutronic quantities. Namely, the impact of the photo-nuclear reactions (γ, n) competing with $(n, 2n)$ in the production of the same residual nucleus was shown to be negligible.

The precise characterization of the core is important and usable for another research as well and among others it can be an excellent tool for validation of neutronic properties of materials inserted into the center of the core or by surrounding it. As an insertion can serve sand, for example, whose neutronic parameters are important not only in space programs but also for spent fuel management, because the SiO_2 is the major material of the Earth crust. Or, the most recent application was the validation of neutronic description of iron and stainless-steel, which is important in criticality safety issues as stainless steel is the major component of water moderated reactors internals.

The essential results, namely criticality, flux distribution, neutron spectra and some of the measured spectral averaged cross section evaluated as spectrum-averaged cross sections (SACS) averaged in ^{235}U PFNS were benchmarked in the IRPhEP database. This database is the most reliable one and is used for tuning of nuclear cross sections. The described field became one of the IRDFF-II reference benchmark neutron fields and the measured data were used for improving the newly developed IRDFF-II neutron dosimetry library.

It was reported in periodic report covering 1/09/2019 to 28/02/2021 that among the various possible experiments under consideration, priority was given to a pile noise experiment (HLUK), from which the delayed neutron fraction (β_{eff}) and prompt neutron lifetime (ℓ) could be inferred. Results of these experiments are summarized in chapter 4.

The work summarized in this report and referred in more details in referenced journal papers contributed to the new releases of nuclear data libraries IRDFF-II [1], FENDL-3.2b [2], and prepared ENDF/B-VIII.1, where the LR-0 team members are mentioned as coauthors of the libraries.

1 LR-0 reactor

The reference neutron field was found in a specifically designed core assembled in the LR-0 reactor. The LR-0 is a zero-power light water pool type reactor operated by the Research Centre Řež (Czech Republic). Continuous nominal power is 1 kW with a thermal neutron flux of about $10^9 \text{ cm}^{-2}\cdot\text{s}^{-1}$ and a fast neutron flux (above 1 MeV) of $2 \times 10^8 \text{ cm}^{-2}\cdot\text{s}^{-1}$. An illustration of the LR-0 reactor and a scheme of the core configuration for this experiment are shown in Figure 1. The first criticality was reached in December 1982.

The main reactor feature that allows these experiments to be performed is the versatility of the core. The experiments are conducted at atmospheric pressure and room temperature. The change of the moderator level or control-cluster position is used to control reactor power. The LR-0 fuel elements are radially identical with those used in VVER NPPs, axially, the active part is shortened to 125 cm.

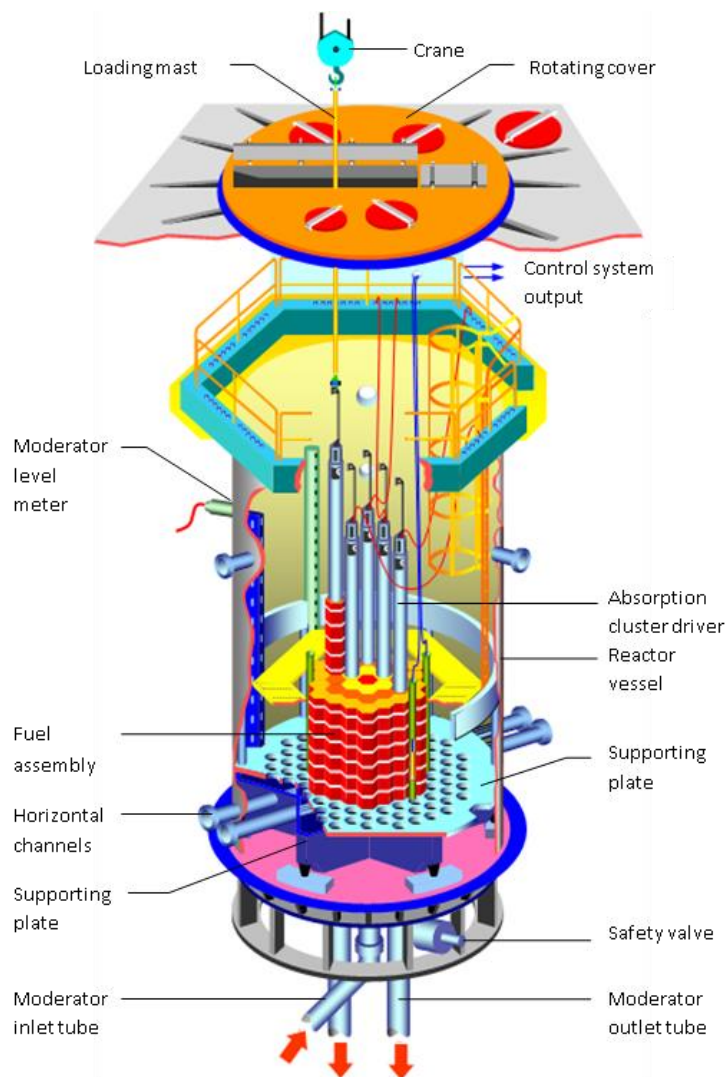


Figure 1: Scheme of LR-0 reactor [3]

The main objective of the projects on the LR-0 reactor is to create the experimental databases, which could be utilized for verification of codes and libraries used for neutronic calculations in safety analyses of the criticality of cores, storage, and transport-cask lattices for VVER type reactors [4]. In combination

with VVER-1000 Mock-Up with full scale simulators of internals, downcomer, reactor pressure vessel, and even biological shielding. It is also used as a validation tool in criticality issues [4], reactor dosimetry of internals [5], reactor pressure vessel [6], and also validation tool for mathematical models focused on concrete biological shielding [7].

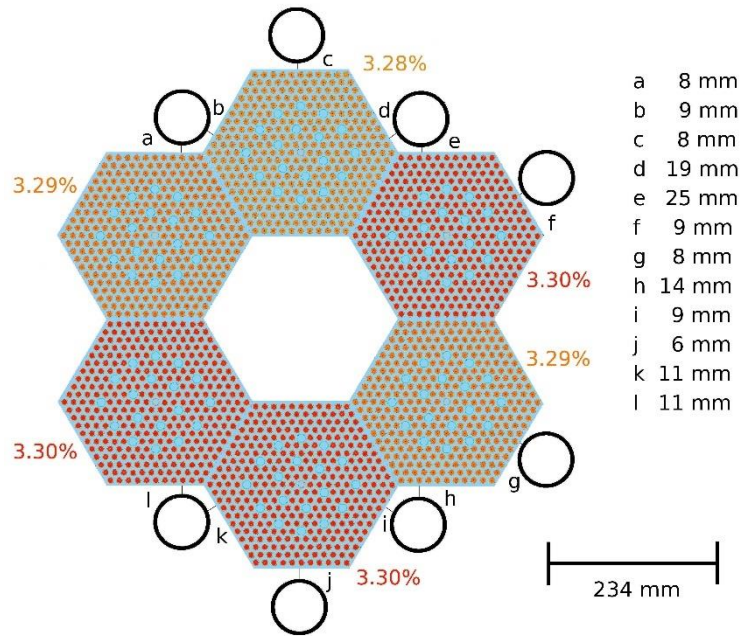


Figure 2: Radial cross-section of the core with specified enrichment, the distances are upright from pin [3]

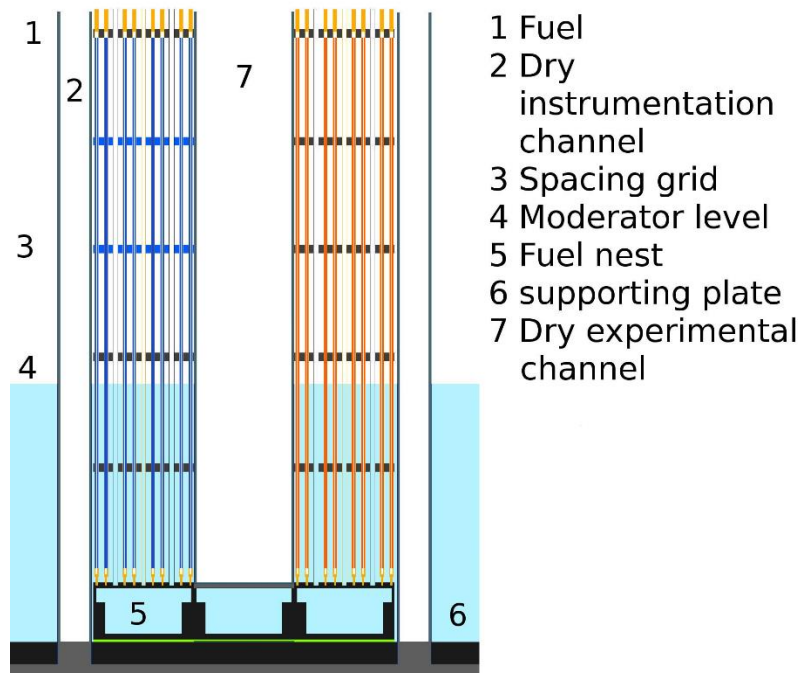


Figure 3: Axial section of core [3]

The reference benchmark neutron field was identified in a dry channel surrounded by six fuel assemblies enriched to 3.3 wt. %. This geometry is simple and easily to repeatable. This simplicity also allows usage in different validations of transport cross sections, where the studied material is inside of the core, or surrounds it. The radial section of used geometry is plotted in Figure 2, the axial plot in Figure 3

1.1 Characterization of critical parameter

The reactivity in the LR-0 reactor can be driven by water level as well as by control clusters with rods filled by B_4C . These control clusters are essential in VVER-1000 Mock-Up[8], where the fuel is fully flooded. This fully flooded core is important for deep penetration experiments, where the upper water reflector decreases leakage flux, thus minimizing unwanted room effect [9].

In smaller cores, the reactivity is driven exclusively by the water moderator level. In that case, the moderator level (H_{cr}) acts as a critical parameter. If the moderator level slightly exceeds the H_{cr} , the one-group asymptotic approximation [3] may be used to express the reactivity.

Criticality is obtained by adjusting the moderator level (H_{cr}) for a given core map and enrichment of the fuel assemblies. When the moderator level is slightly above H_{cr} , reactivity may be expressed via one-group (asymptotic) approximation as (1) (see ref. [10]).

$$\rho(H) = \frac{C}{(H_{cr} + \lambda_z)^2} \left[\frac{1}{\left(1 + \frac{H - H_{cr}}{H_{cr} + \lambda_z}\right)^2} - 1 \right]; \rho = \frac{k_{eff} - 1}{k_{eff}}; k_{eff} = \frac{k_{\infty}}{1 + M^2 B^2}; \quad (1)$$

Where C is constant; $C = \frac{M^2 \pi^2}{k_{\infty}}$; B^2 geometry buckling, M^2 migration area, and λ_z is the axial extrapolation length.

If reactivity is less than 25 ¢, Taylor expansion of relation (2) around H_{cr} may be used. Reactivity for various moderator heights above the critical level was measured using the inverse kinetics method with time-dependent neutron counts. The digital reactimeter and data acquisition were implemented using an independent EWS computer system described in [11].

$$\rho(H) = f(H, a_1, a_2) = a_1 \cdot (H - a_2) \cdot \left(1 - \frac{3}{2} \frac{H - a_2}{a_2 + \lambda_z} \right) \quad (2)$$

where $a_1 = \frac{\delta\rho}{\delta H}$; $a_2 = H_{cr}$

The tolerance of the measured H_{cr} for the LR-0 reactor, based on level meter manufacturer technical data, is 0.003 cm. The total uncertainty of H_{cr} at the 1σ level is determined from the tolerance of the level meter and its calibration. The uncertainty of the level meter calibration is determined by the precision at which the electrical needle is positioned. This is an electric contact used for repeated level meter tests, which is fixed on the vessel wall at the height of 10.0 cm with the uncertainty of 0.05 cm. The combined uncertainty of the critical water level value H_{cr} , which is the uncertainty of the needle

level combined with uncertainty from statistical regression analysis, is approximately 0.058 cm (see [12]). This value is taken as the standard uncertainty for critical water-level height.

The measured critical height was used as a parameter in the computation model describing the critical core. As the core is exactly critical at the experiments, experimental k_{eff} is considered as 1. When k_{eff} obtained using of the computation model is very close to 1, it can be assumed that the developed theoretical description of the core is valid in terms of criticality.

The criticality was measured in various core arrangements (see Figure 4) containing reference case used for measurement of cross sections and arrangement where the core is surrounded by stainless steel. The experimental results are summarized in Table 1 and results of calculations in Table 2. Tests of the different component evaluations are in Table 3.

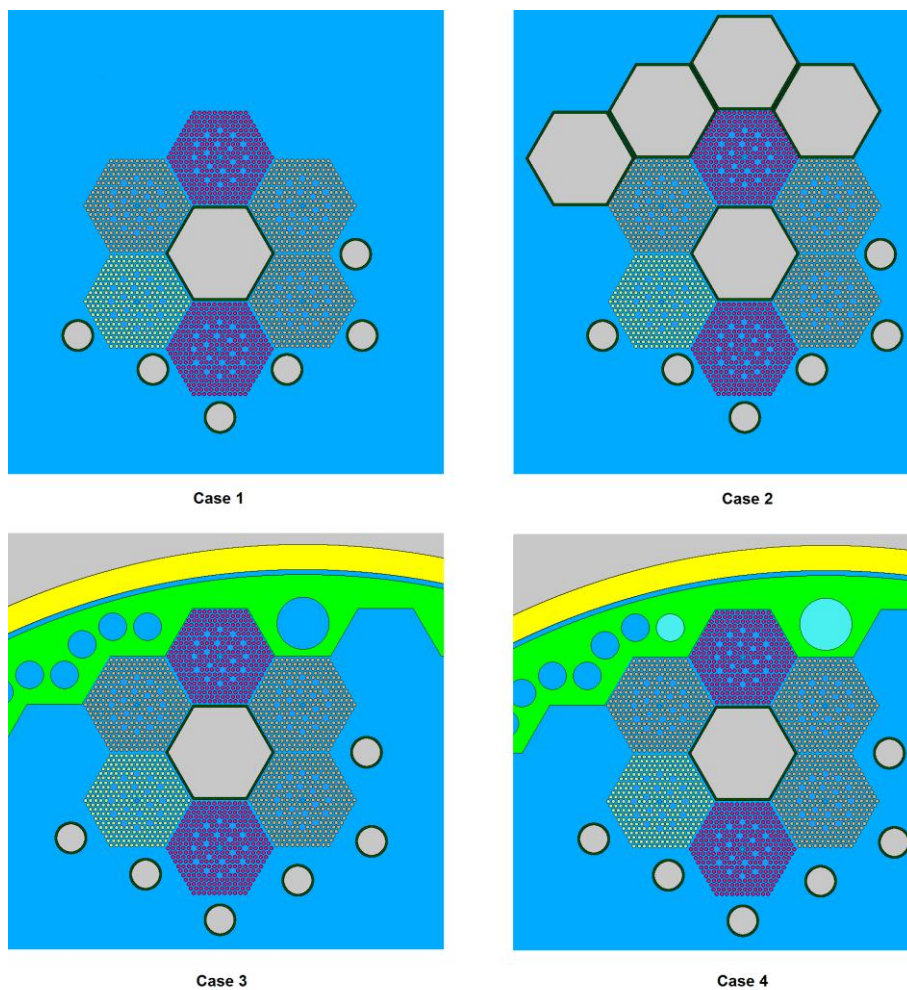


Figure 4: The experimental configurations with various stainless steel reflector designs

When the core is surrounded by water, good agreement is reached, confirming the accurate description of the driver core. However, when the core is surrounded by stainless steel notable discrepancies are reported. This leads to the conclusion that the stainless steel needs to improve its description. It's worth noting, during testing of stilbene apparatus, neutron leakage spectrum from stainless steel block was measured [13]. The results confirm satisfactory performance of stainless steel in INDEN evaluation, which will become part of ENDF/B-VIII.1.

Table 1: Critical levels and following k_{eff} calculated with MCNP6 and ENDF/B-VIII.0.

		H_{cr} (mm)	unc. (mm)	ENDF/B-VIII.0
Water reflected core	Case 1	549.39	0.41	0.99987
4 void assemblies	Case 2	621.78	0.17	0.99969
Near baffle	Case 3	540.70	0.72	0.99774
Near baffle + steel in channels	Case 4	527.47	0.04	0.99797

Table 2: K_{eff} calculated with MCNP6 and various data libraries.

	ENDF/B-VIII.0	ENDF/B-VII.1	ENDF/B-VI.2	JEFF-3.3	JENDL-4	ROSFOND-2010	CENDL-3.1
Case 1	0.99987	1.00072	0.99266	1.00092	1.00032	1.00007	0.99916
Case 2	0.99969	1.00032	0.99253	1.00083	1.00001	0.99968	0.99894
Case 3	0.99774	0.99838	0.99085	0.99895	0.99818	0.99769	0.99657
Case 4	0.99797	0.99873	0.99126	0.99931	0.99843	0.99807	0.99678
$\langle \Delta k_{eff} \rangle$	0.00095	0.00094	0.00798	0.00091	0.00081	0.00096	0.00182

Table 3: K_{eff} calculated with MCNP6 and ENDF/B-VIII.0 with changed evaluations for iron, chromium and oxygen.

	Fe INDEN	Fe, Cr INDEN	Fe INDEN; O ENDF/B-VII.1	Fe, Cr INDEN; O ENDF/B-VII.1
Case 1	0.99985	0.99973	1.00122	1.0011
Case 2	0.99965	0.99945	1.00099	1.00073
Case 3	0.99772	0.99734	0.99897	0.99857
Case 4	0.99803	0.99758	0.99936	0.99897
$\langle \Delta k_{eff} \rangle$	0.00096	0.00122	0.00104	0.00106

1.2 Characterization of the neutron flux profile

The neutron flux density spatial distribution is an important parameter describing neutron field [14], [15]. Especially when irradiated samples have non-point character, the field is strongly connected with neutron flux gradient in the sample [16].

Neutron flux can be monitored by both active and passive methods. Monitoring by passive measures is highly important in applications where the active measurements are infeasible. These applications include, for example, absolute measurements for reactor dosimetry (e.g., behind reactor pressure vessel in NPP) or fusion applications. Therefore, it is necessary to use especially materials with known properties (namely activation cross section) in a given energy spectrum [17], [18]. In the case of the benchmark reference field, the profile has been characterized by means of the calculations in the MCNP model [19] and corresponding activation experiments.

The reaction rates were evaluated using gamma activity determined by means of semiconductor gamma spectrometry. The efficiency curve has been determined by calculation using a validated mathematical model [16]. The model has been compiled using geometrical parameters obtained from radiography (see Figure 6) and experimentally determined insensitive layer [20].

The gamma activity is determined after the irradiation using following formulas:

$$\frac{A(\underline{P})}{A_{Sat}(\underline{P})} = \sum P_{rel}^i \times (1 - e^{-\lambda \cdot T_{ir}^i}) \times e^{-\lambda \cdot T_{end}^i} \quad (3)$$

$$q(\underline{P}) = \left(\frac{A(\underline{P})}{A_{Sat}(\underline{P})} \right)^{-1} \times NPA(T_M) \times \frac{\lambda}{\varepsilon \times \eta \times N} \times \frac{t_{real}}{(1 - e^{-\lambda \cdot T_m})} \times \frac{1}{e^{-\lambda \cdot \Delta T}} \times \frac{1}{k_{CSEF}} \times k_{SSEF} \quad (4)$$

where:

$\frac{A(\underline{P})}{A_{Sat}(\underline{P})}$ is relative portion of saturated activity induced during irradiation experiment,

P_{rel}^i is relative power on the i-th day of irradiation, $P_{rel}^i = \frac{P^i}{P}$,

$q(\underline{P})$ is reaction rate of activation foil during power density \underline{P} ,

T_{ir}^i is irradiation time on i-th day of irradiation,

T_{end}^i is time from the end of i-th day of irradiation to end of all irradiations,

λ is decay constant of corresponding material,

T_m is the time of activation foil measurement by HPGe,

ΔT is the time between the end of irradiation and the start of HPGe measurement,

$NPA(T_m)$ is the measured number of counts,

ε is gamma branching ratio of activation material – depending on the material,

η is detector efficiency - the result of MCNP calculation,

N is number of target isotope nuclei in activation foil,

t_{real} is the real-time of counting system of the HPGe ($= T_m$),

t_{live} is the live time of the counting system of the HPGe ($< t_{real}$),

k_{CSEF} is the coincidence summing effect correction,

k_{SSEF} is the resonance self-shielding effect correction determined by MCNP.

The activation foils with well-defined dosimetry reactions ($^{58}\text{Ni}(n,p)$, $^{197}\text{Au}(n,\gamma)$, $^{181}\text{Ta}(n,\gamma)$) were placed in geometrically well-defined positions to the reactor core Figure 5, Figure 7. The reactions were selected to cover the thermal, epithermal, and fast part of neutron spectra.

The experimental data were compared with the developed calculation model. Due to satisfactory agreement between both, it can be concluded that the developed model is valid in the meaning of flux distribution. The details can be found in [16]. The reaction rate ratio essential for spatial flux characterization is in Table 4. The calculated gradient for $^{58}\text{Ni}(n,p)$ reaction together with C/E comparison is in Table 5. Due to the good agreement, it can be stated that developed calculation model is usable for characterization of spatial distribution of neutron flux in special core.

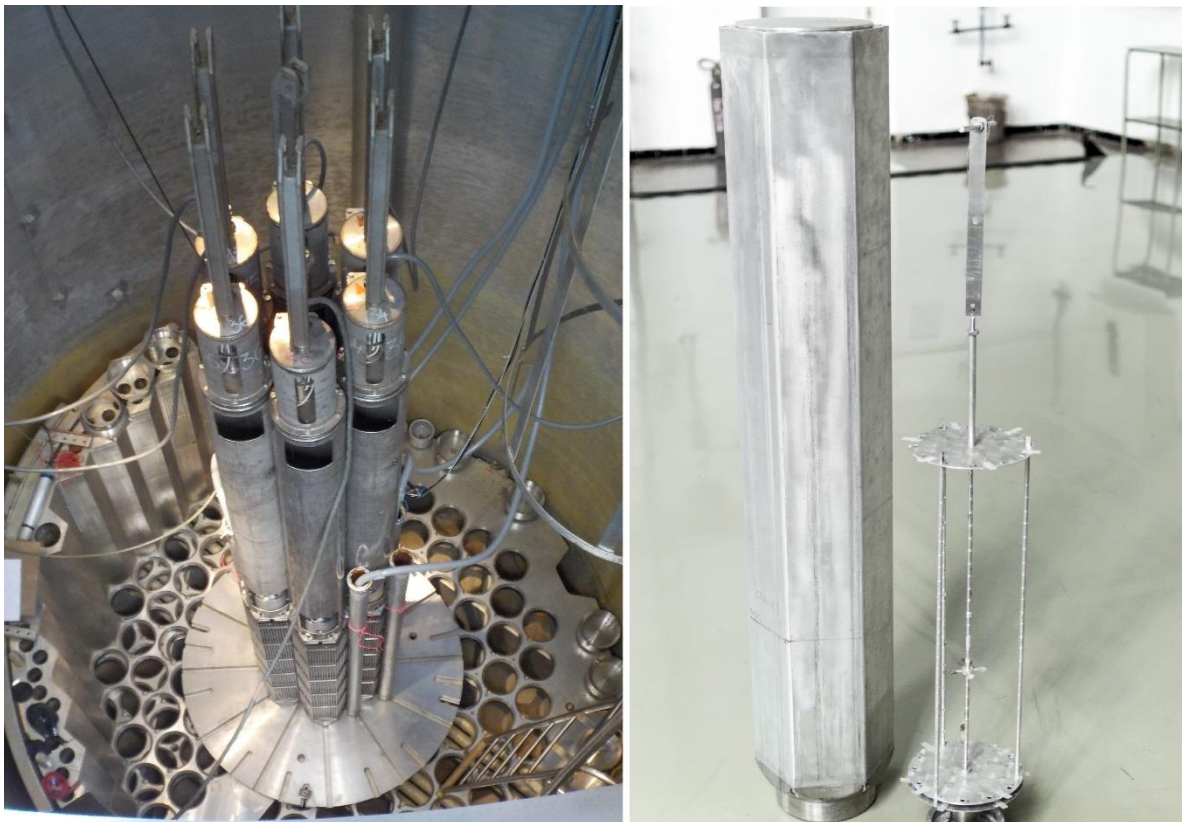


Figure 5: Overhead view inside the LR-0 reactor with a special core without a moderator (left) and a dry experimental channel with activation foil holder (right) [16]

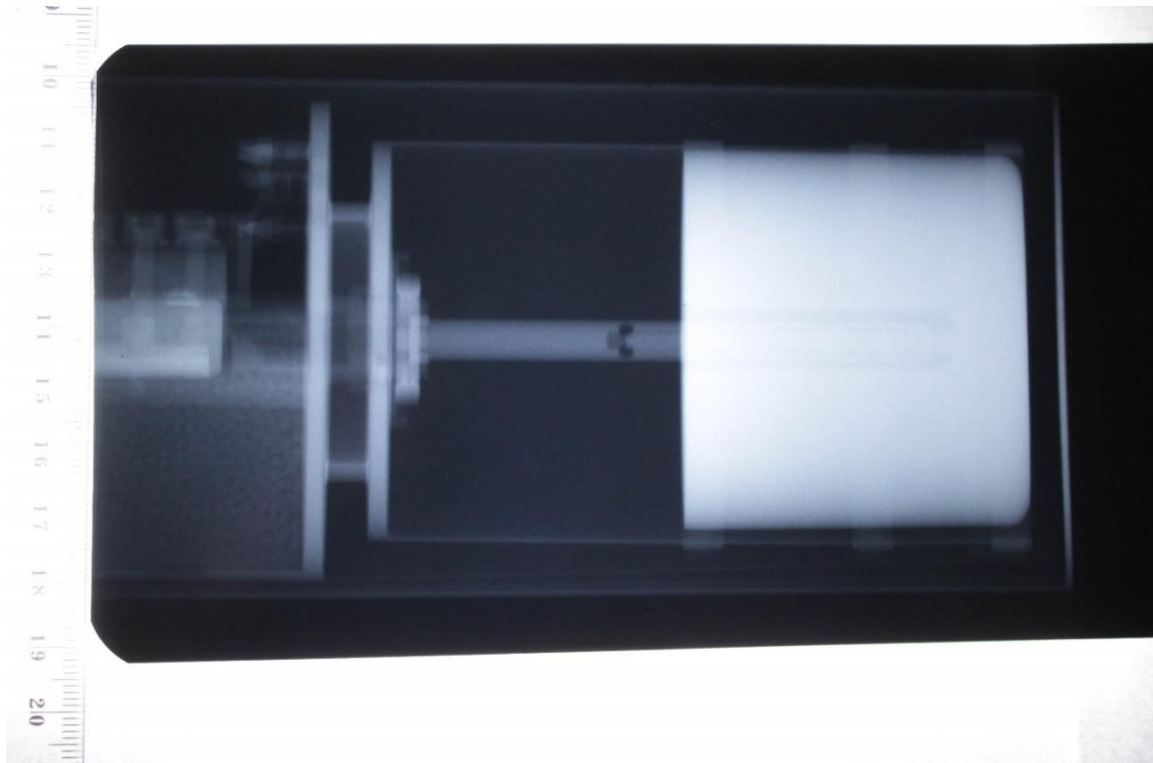


Figure 6: HPGe GEM35 detector radiogram used for determination of mathematical model

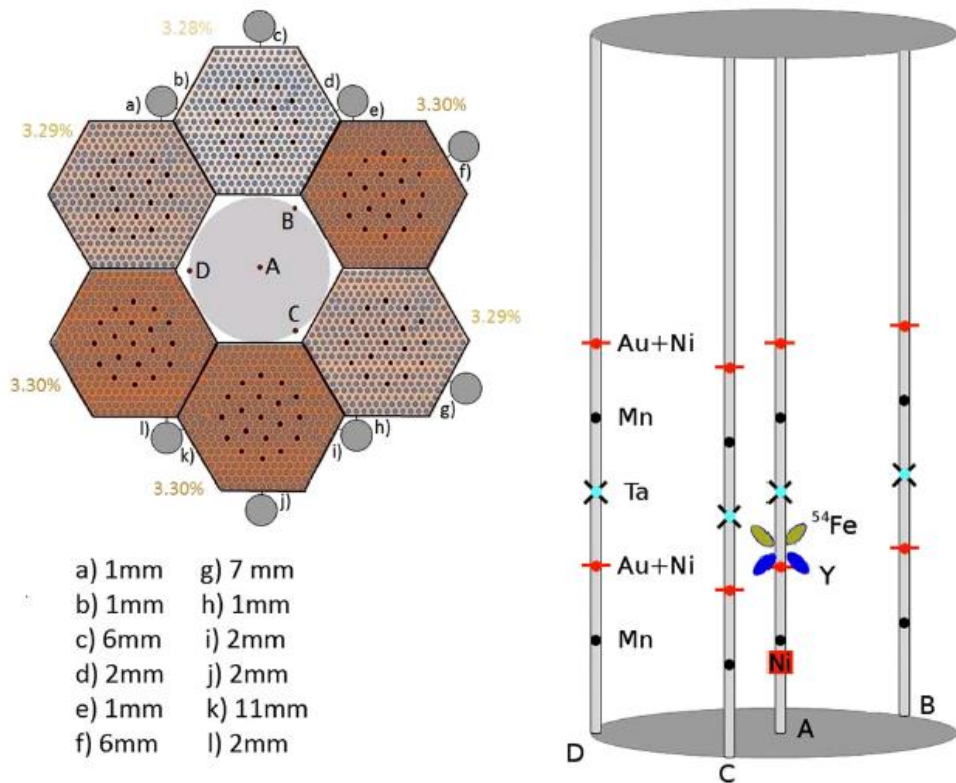


Figure 7: Scheme of irradiation experiment

Table 4: Measured and calculated reaction rate ratio in spatial flux characterization.

	Foil	Experiment				Calculation			
		Position A	Position B	Position C	Position D	Position A	Position B	Position C	Position D
Level 1	Mn	1.007	0.982	1.014	0.997	0.991	1.001	1.002	1.005
Level 2	Au	0.992	0.975	1.009	1.023	0.992	0.996	0.998	1.014
Level 2	Ni	0.993	1.009	0.971	1.027	0.971	1.008	1.004	1.017
Level 3	Ta	0.988	1.000	1.004	1.009	0.976	1.014	1.001	1.010
Level 4	Mn	0.977	0.985	1.031	1.007	0.982	1.007	1.005	1.006
Level 5	Au	1.009	0.977	0.986	1.027	0.991	0.986	1.015	1.008
Level 5	Ni	1.018	0.995	1.027	0.961	0.969	1.009	1.009	1.013

Table 5: Calculated gradient between monitoring positions and in the reference volume for the $^{58}\text{Ni}(n,p)$ reaction rates together with experimental validation during the first irradiation experiment. The coordinates are relative to the center of dry hexagonal channel, axially at beginning of the fission column.

Position	Pin 1	Pin 2	Pin 3	Pin 4
	x=4.7 y=8.14	x=4.7 y=-8.14	x=-9.4 y=0	x=0 y=0
z=18.35 cm	1.014	1.014	1.011	0.967
z=23.35 cm	1.042	1.047	1.042	1.042
z=28.35 cm	1.044	1.046	1.045	1.005
z=33.35 cm	1.006	1.007	1.004	0.965
	C/E-1			
z=18.35 cm	0.6%	0.3%	3.0%	0.3%
z=23.35 cm	-	-	-	-
z=28.35 cm	-2.2%	2.0%	-	2.4%
z=33.35 cm	-0.8%	-0.2%	-0.3%	-1.4%

1.3 Characterization of neutron and gamma spectrum

The knowledge of neutron spectrum is crucial for describing neutron field because neutronic cross section strongly depends on neutron energy. Often the spectrum is evaluated based on deconvolution from the set of reaction rates [21]. In the case of the LR-0 reference field, the neutron spectrum was measured using stilbene scintillation spectrometry [22]. As the light outputs of the scintillator coming from gamma and neutron reactions are different, their precise characteristics are important in the determination of the stilbene response function and calibration [23]. The neutrons and gammas in mixed fields can then be distinguished using PSD [24]. The specialists from University of Defence (Brno, Czech Republic) tested the developed stilbene spectrometer in a Physikalisch-Technische Bundesanstalt (PTB, Braunschweig, Germany) reference neutron field. An accelerator, producing mono-energetic neutron fields (1.2 MeV, 2.5 MeV, 5 MeV, 14.6 MeV, and 19 MeV), has been used for absolute sensitivity and detector response function studies [25].

In the neutron spectra measurements, stilbene scintillator with cylindrical geometry and dimensions $\varnothing 10 \text{ mm} \times 10 \text{ mm}$ and photomultiplier RCA 8575 were used. The separation between neutron and gamma pulses is performed by means of pulse shape discrimination (PSD) of the measured response. Pulse Shape Discrimination parameter (D) is derived by an integration algorithm, which principle lies

in the comparison of area limited by part of a trailing edge of the measured response (Q_1) with area limited by the whole response (Q_2). The areas Q_1 and Q_2 , as integrals over time, are expressed in Equation (5), and their illustration is shown in Figure 8.

The time offset t_2 is set for the optimal discrimination properties (namely, the most significant possible difference in the discrimination parameter for neutrons and gammas) to about 1/10 to 1/3 of the trailing edge. It varies for each scintillation material (stilbene, p-terfenyl). In this way, it is possible to eliminate the classification mistakes caused by the dependency of the response shape on its amplitude.

Charge Q_1 is determined by an area limited by the response course within a time interval (t_2, t_3). The charge Q_2 is determined by an area limited by the response course within firmly defined times t_0 and t_3 . Times t_0 and t_3 depend on the parameters of the measuring apparatus, and time t_3 is defined as the end of the response.

Using PSD, energy-dependent recoil proton responses $S(E_p)$ are evaluated. The neutron fluxes are then evaluated by deconvolution according to Equation (6). The response matrix of the crystal $K(E_N, E_p)$ was determined employing Monte Carlo code NEU-7. The methodology was tested in various fields, especially fission reactor fields, $^{252}\text{Cf}(s.f)$, and also DT generator fields [26].

$$Q_1 = \int_{t_2}^{t_3} i(t)dt, \quad Q_2 = \int_{t_0}^{t_3} i(t)dt, \quad D = \frac{Q_1}{Q_2} \quad (5)$$

$$S(E_p) = \int K(E_N, E_p)\phi(E_N)dE_N \quad (6)$$

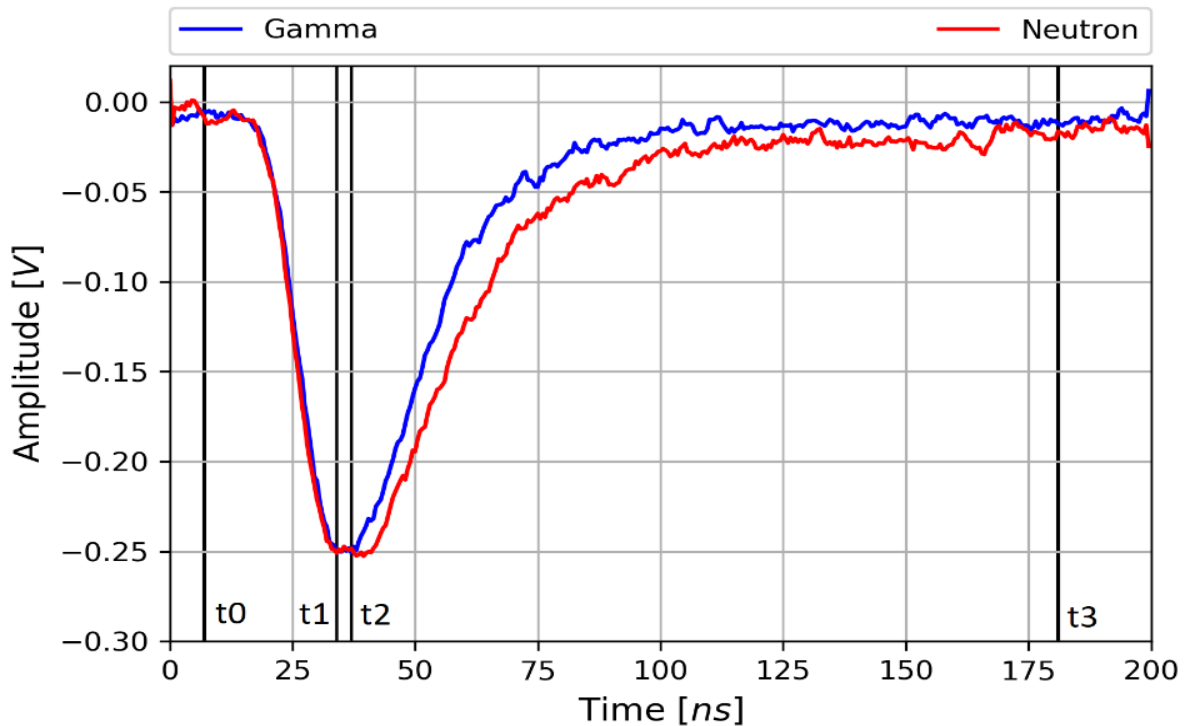


Figure 8: Comparison of real neutron and gamma pulses from Stilbene scintillation detector with marked examples of a separation boundary for integration algorithm

The gamma spectrum is not primary focused, but its shape is important, because in reactor experiments, there is often a question on the gamma effect on the purity of the experiment. Namely, the problem might be the contribution from (γ, n) reactions whose product is the same as those originating from $(n, 2n)$ reactions.

The resulting electrons from gamma interactions are standardly used for organic scintillator calibration. This procedure is applicable under the assumption that the detection system, including crystal, photomultiplier tube, and associated electronics, is linear. The neutron calibration curve is determined using the gamma calibration curve (Figure 9) from the measurement using the gamma standards' Compton edge energy. An example of the calibration for ^{60}Co peaks is depicted in Figure 10. The linearity of the system is confirmed when the channels of the peaks and their corresponding energies have a linear dependence. For this measurement, the linearity is plotted in Figure 11.

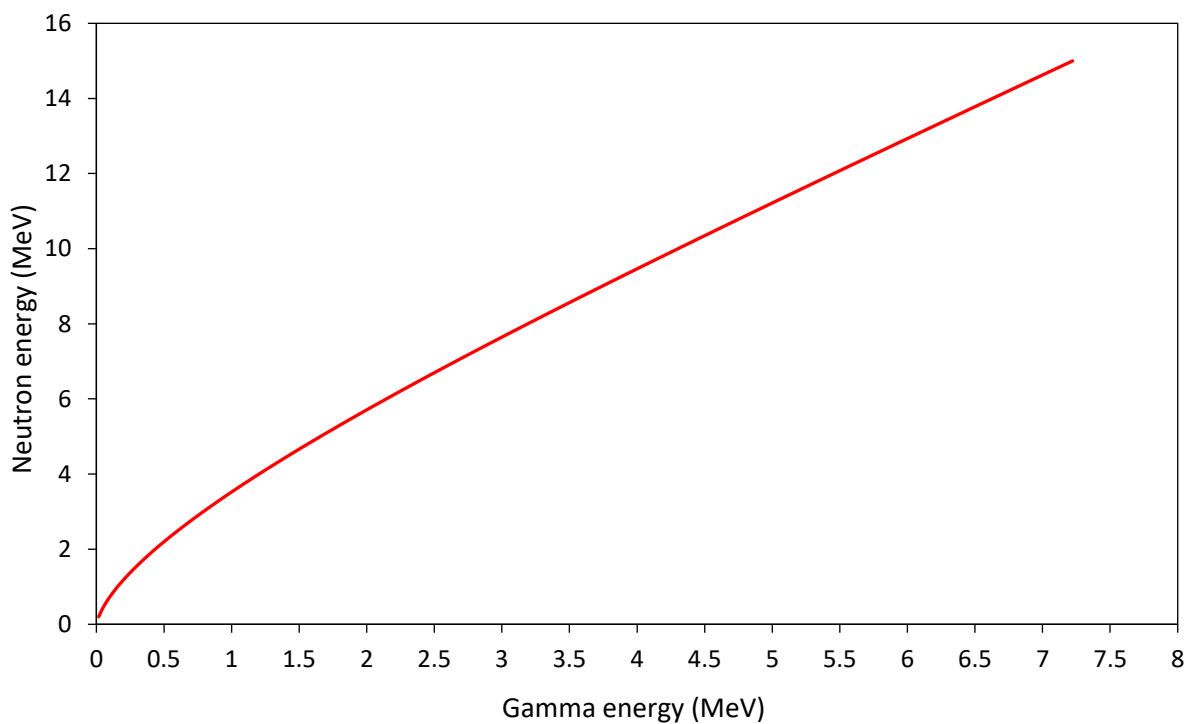


Figure 9: Relation between Neutron and Gamma Energy in Stilbene Detector.

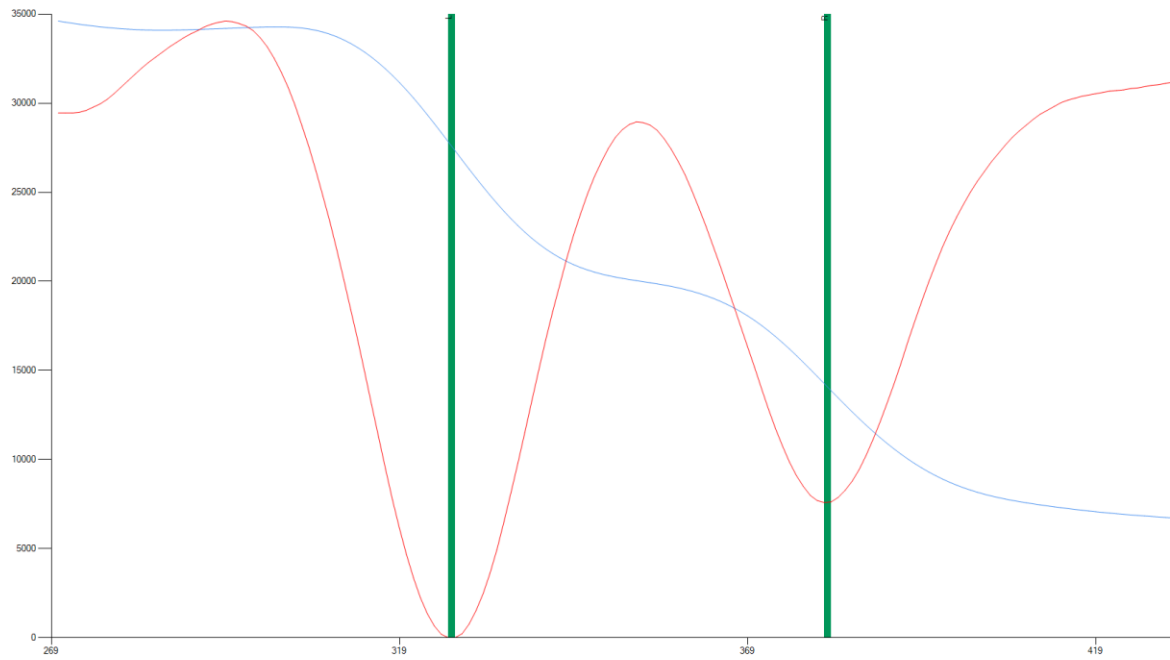


Figure 10: Calibration of the Apparatus Spectrum using ^{60}Co Peak.

The electron spectrum is the blue line, the differentiation of the spectrum with visible inflections is the red line. Green lines show channel number settings for energy scale calibration.

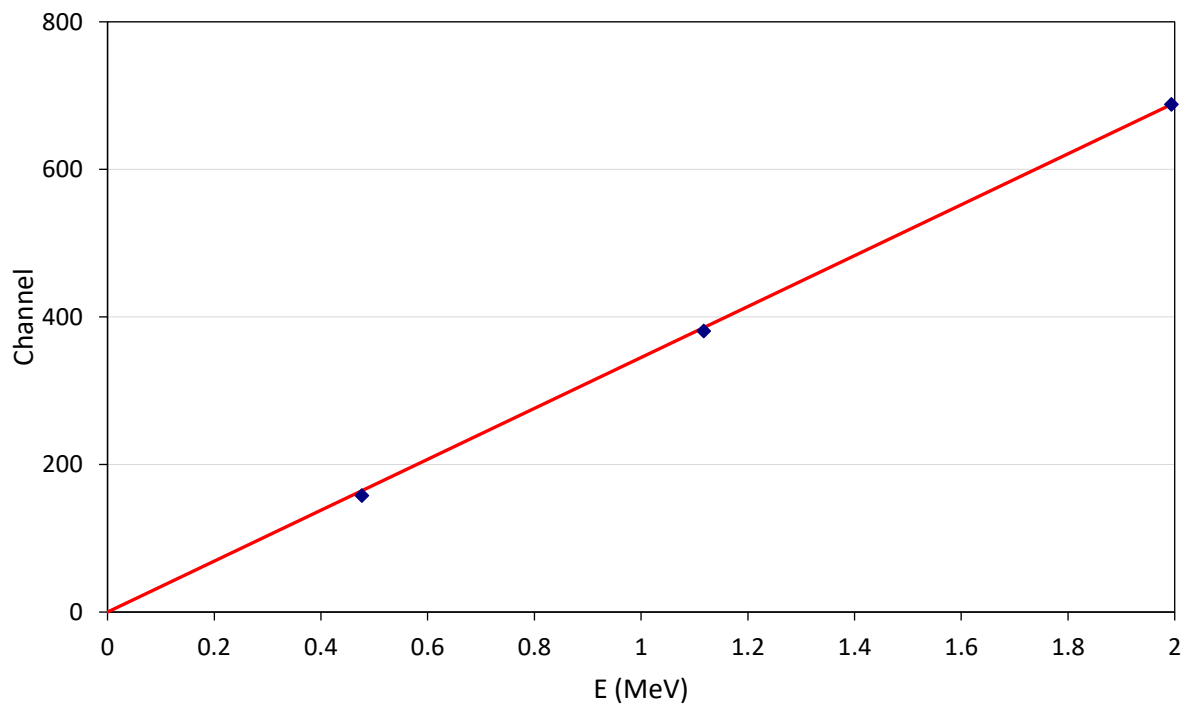


Figure 11: Linearity of Calibration (Cs line, Co line, $^1\text{H}(n,\gamma)$) $U_{\text{PMT}}=1400\text{ V}$.

As the calibration is indirect, a question may often arise about the reliability of obtained results. Due to this fact the methodology has been tested in many various fields as the VR-1 reactor radial channel [28], Mock-Up of VVER-1000 in LR-0 reactor [29], in D-T generator neutron field [30], and radioisotope (Am-Be) neutron field [31], special quasi monoenergetic neutron fields near accelerators [27]. Due to indirect evaluation, the uncertainties of the methodology are very complicated to determine. Often, they are determined using some standard and comparison between the standard values and values obtained by the tested methodology. The bias between both can be understood as the uncertainty of the method itself. In this case, the bias is determined by comparing tabulated spectrum [17], [18] and the spectrum determined by stilbene scintillation spectrometry for $^{252}\text{Cf}(\text{s.f.})$ (Figure 12). Based on such agreement, in fission-like smooth spectrum, which also covers neutron spectrum in reference benchmark neutron field the systematic uncertainty arising from deconvolution problems is not larger than 5%.

A silicon-filtered beam was developed in the LVR-15 research reactor for calibration testing. It is formed by the LVR-15 fission neutrons passing through one meter of single-crystalline silicon [26]. Due to the nature of Si cross section, the field contains several significant peaks in the fast neutron energy range (see Figure 13). Testing in such neutron fields is very valuable because it can reveal specific problems in the deconvolution matrix of the detection system, which may remain hidden in fields with a smooth structure and can provide a tool for proper energy calibration.

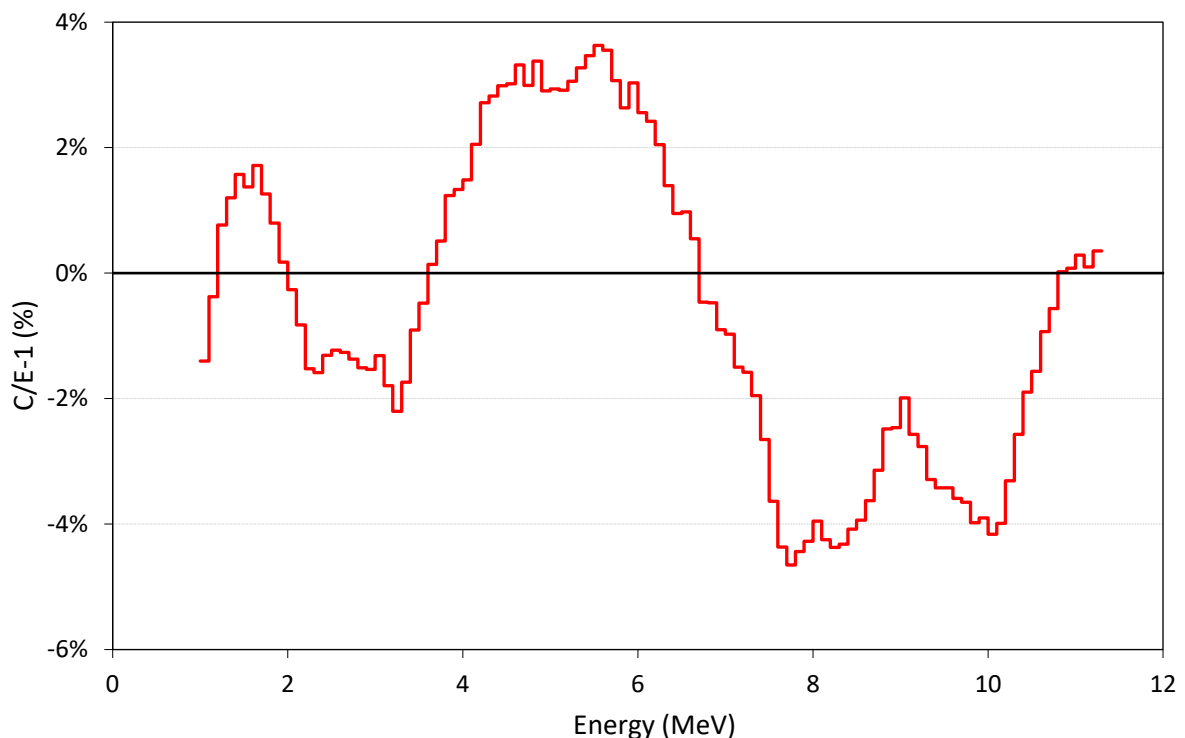


Figure 12: Eval/E-1 of $^{252}\text{Cf}(\text{s.f.})$ for flux 1 m from point source measured with NGA-01 and \varnothing 10 mm \times 10 mm crystal used in experiments.

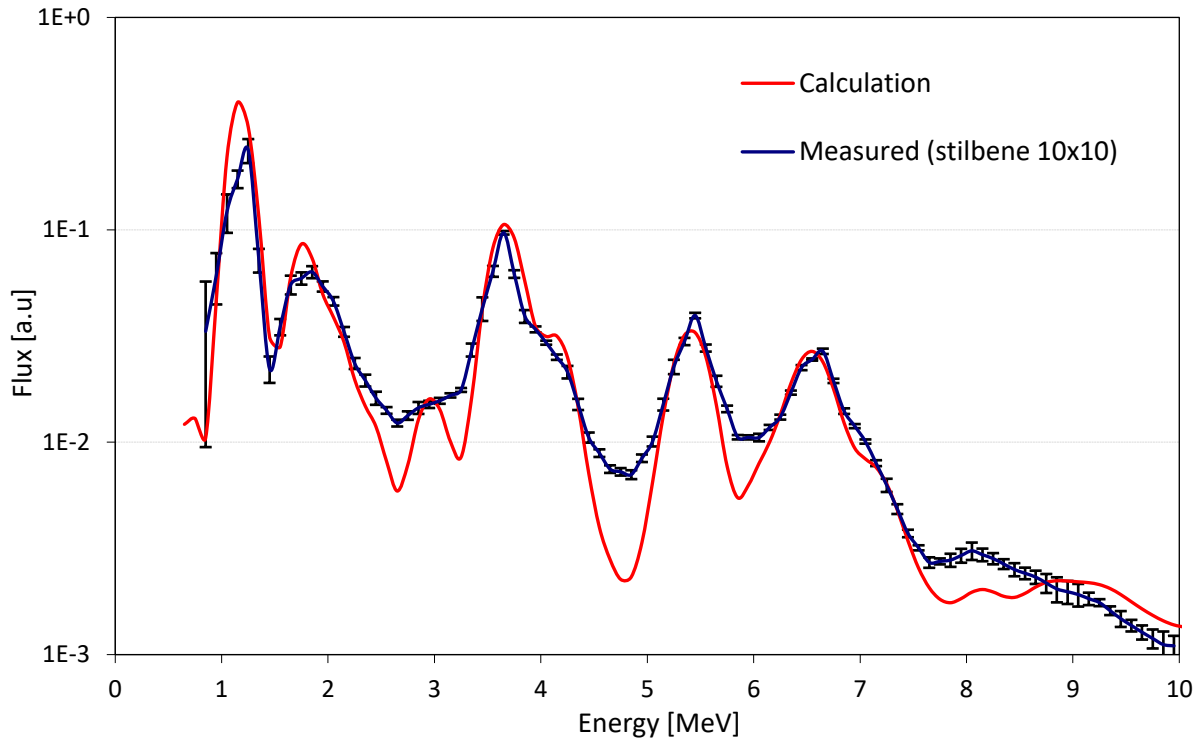


Figure 13: Comparison of calculated and measured Si filtered fluxes.

Using the above described and tested methodology, the neutron spectrum in reference position and region 1 – 14 MeV was determined, in region 0.1 – 1 MeV proportional counters were used [32]. The comparison between calculated and measured spectrum is plotted in Figure 14. Good agreement between calculation and experiment is reported. Due to such agreement, it can be concluded that the developed calculation model for the LR-0 reference benchmark neutron field is valid in terms of neutron spectrum in the reference position.

Moreover, it was demonstrated that the neutron spectrum above 6 MeV is undistinguishable from ^{235}U PFNS (see Figure 15). It means the neutrons with energy above 6 MeV have nearly the same energy distribution as ^{235}U fission neutrons. It also means, using proper normalization, the integral cross sections of reactions induced by neutrons with energy above 6 MeV can be evaluated as integral cross section weighted by ^{235}U PFNS. This is a valuable conclusion because, backwards, it allows using LR-0 data for testing of ^{235}U prompt fission neutron spectrum when the cross section of given dosimetry reactions is well known [22].

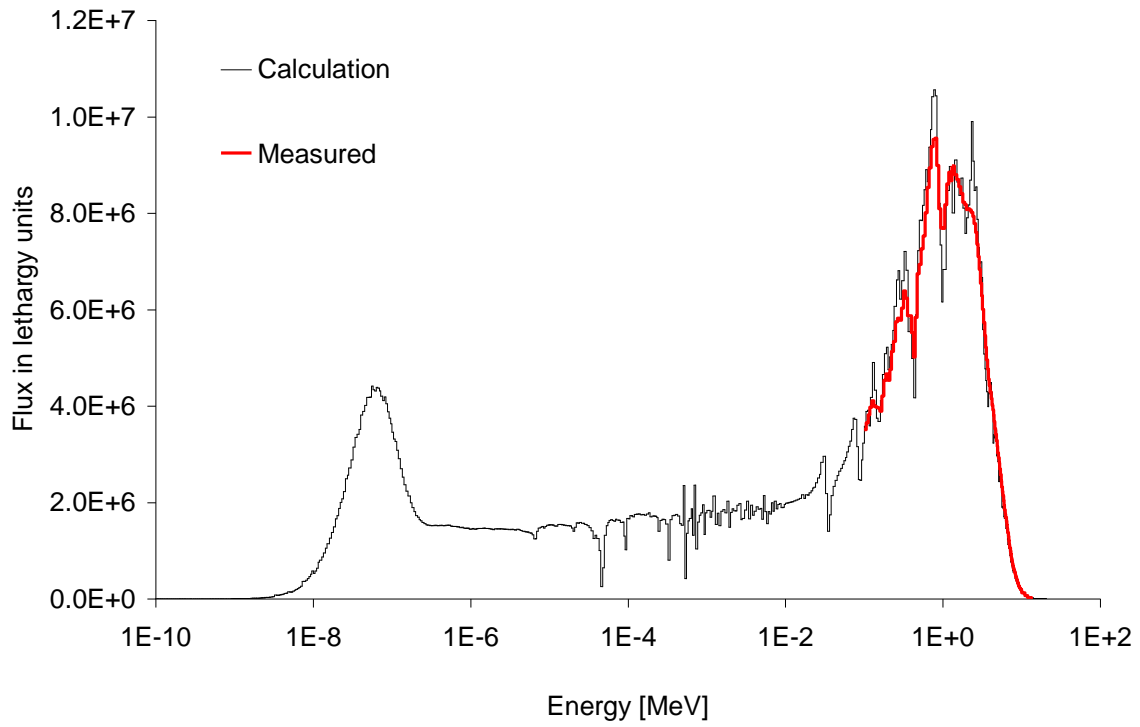


Figure 14: Comparison of Calculated, Measured neutron flux in the same core arrangement [33].

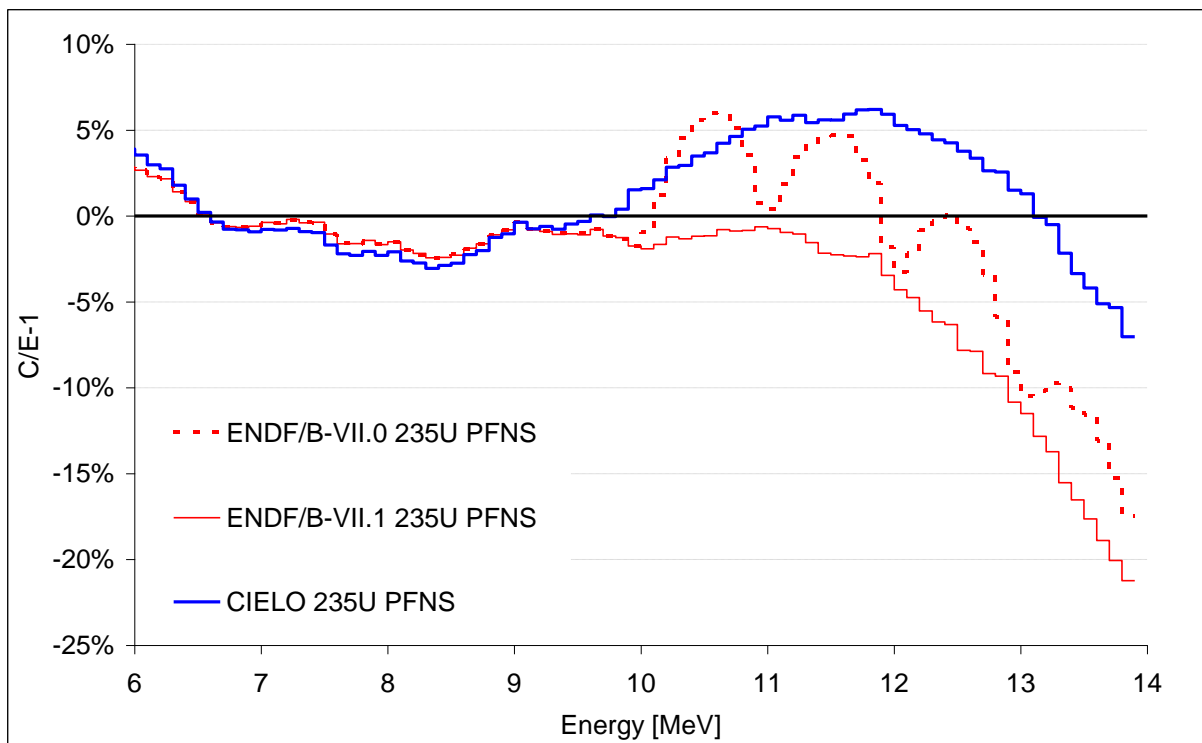


Figure 15: Identity between LR-0 and ^{235}U PFNS in ENDF/B-VII.0, ENDF/B-VII.1 and CIELO [22] which is adopted in ENDF/B-VIII.

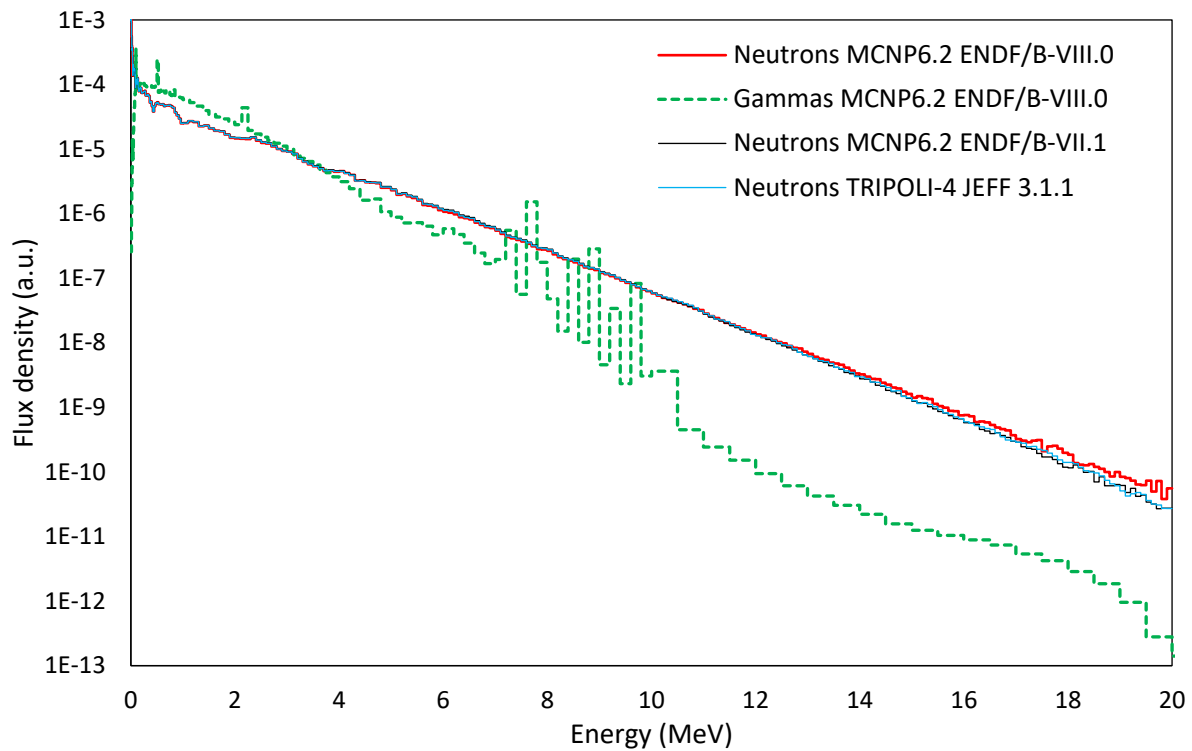


Figure 16: Calculated neutron and gamma fluxes in MCNP 6.2 and TRIPOLI [34].

The gamma spectrum in reference LR-0 field was evaluated as well. Calculation shows that gamma spectrum goes up to 20 MeV (see Figure 16). The experiment with newly developed gamma response matrix [35] focused on gamma measurement up to 13 MeV (Figure 17). The ENDF/B-VIII.0 evaluation is in good agreement with calculation, whereas calculations using JEFF-3.3 and JENDL-5 show significant deficiencies in region above 9 MeV. This result is important especially in the evaluation for $(n,2n)$ reaction cross section, because it implies that the impact of the photo-nuclear reaction which leads to the additional production of the same residual nuclei can be reliably evaluated with ENDF/B-VIII. The detail evaluation on effect of gamma can be found in Figure 19 and listed Table 6. Generally, the effect of gamma is not high, being mostly below 0.1 %. The significant exception from studied reactions is $^{197}\text{Au}(n,2n)$, where due to the threshold of $^{197}\text{Au}(\gamma,n)^{196}\text{Au}$ of about 8.1 MeV the effect of gamma can reach up to 1 % (Figure 19 or listed in Table 6). It means that in ^{196}Au from gold activation measurement about 1% of total activity is of (γ,n) origin instead of proposed $(n,2n)$.

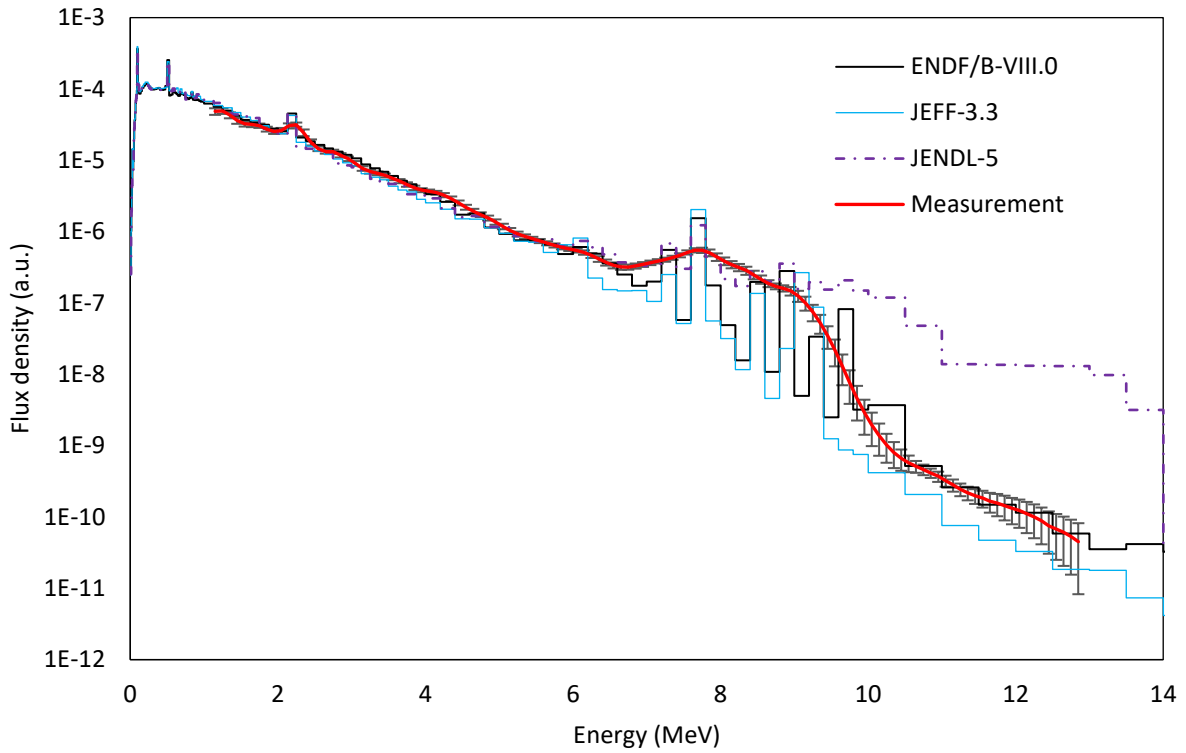


Figure 17: Comparison of measured and calculated gamma spectra in reference neutron field [35]

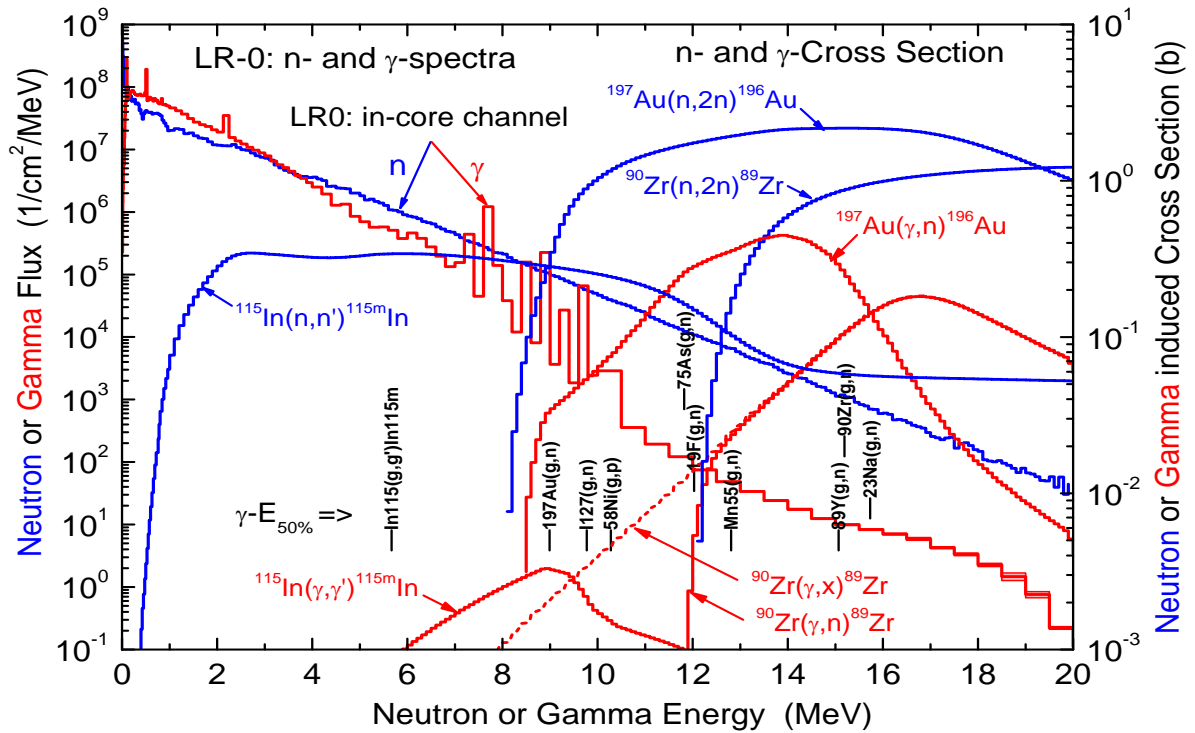


Figure 18: Cross section of selected (γ,n) reactions with gamma spectrum induced by neutron capture on iron.

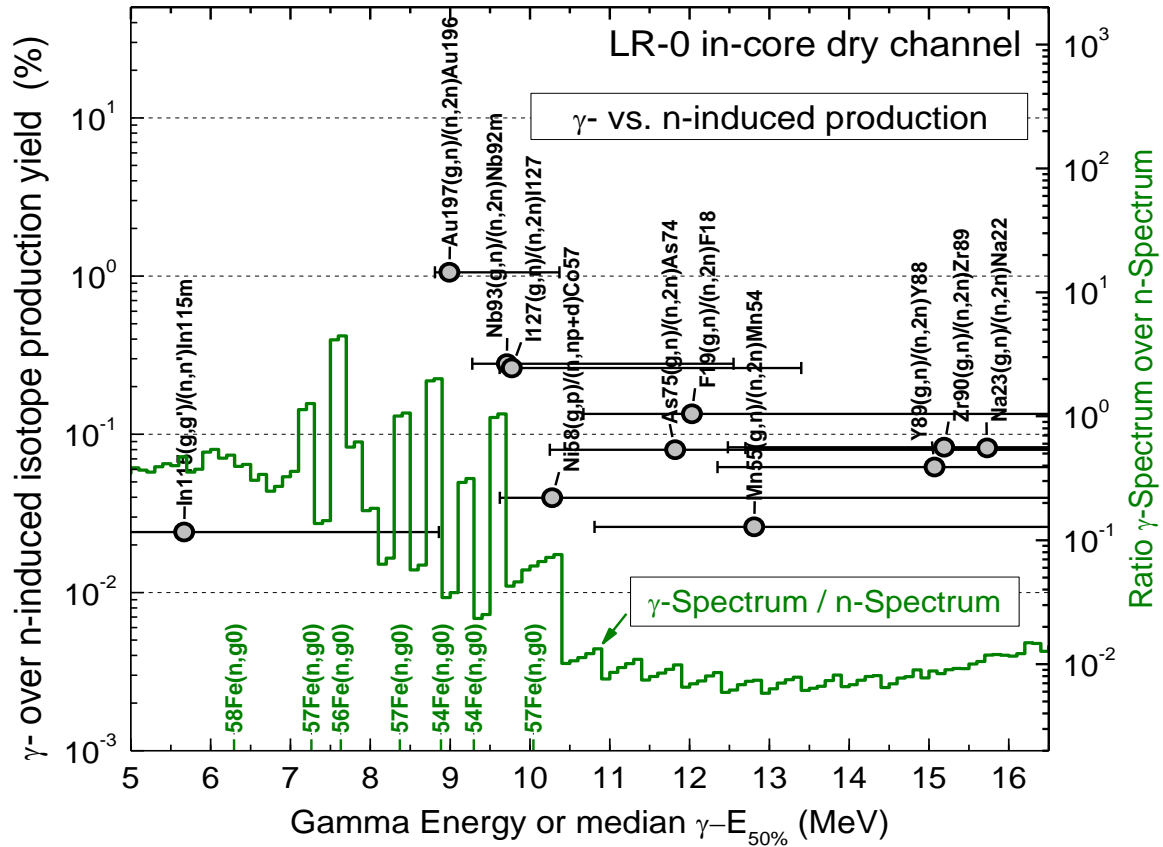


Figure 19: Left axis: Calculated gamma induced over the neutron induced production yields for the same residual isotope versus the gamma median energy γ - $E_{50\%}$ (shown by points); the horizontal bars indicate the (5 – 95)% response domain. Right axis: Ratio of the absolute γ -ray and neutron spectra in the dry hexagonal channel of LR-0 - green histogram. The energies of γ -rays $E_{\gamma 0}$ from (n_{th}, γ_0) on the Fe stable isotopes are indicated by green bars and labels

Table 6: Neutron and gamma induced reactions leading to the same residual nucleus [34]

Reaction	E_{thr} , MeV	$E_{50\%}$, MeV	SACS, mb	Rel. Unc., %	Reaction Rate, 1/kcode	Fraction, %
Competition between reactions (n,n') and (γ,γ')						
$^{115}\text{In}(n,n')^{115m}\text{In}$	0.339	2.481	5.594E+01	1.69	1.688E-05	99.98 \pm 0.00
$^{115}\text{In}(\gamma,\gamma')^{115m}\text{In}$	0.336	5.669	2.651E-02	0.03	4.065E-09	0.02 \pm 0.00
Competition between reactions (n,2n) and (γ,n)						
$^{197}\text{Au}(n,2n)^{196}\text{Au}$	8.114	10.420	9.113E-01	1.93	2.749E-07	98.96 \pm 0.02
$^{197}\text{Au}(\gamma,n)^{196}\text{Au}$	8.072	8.992	1.892E-02	0.10	2.902E-09	1.04 \pm 0.02
$^{93}\text{Nb}(n,2n)^{92m}\text{Nb}$	9.063	11.210	1.249E-01	0.88	3.767E-08	99.72 \pm 0.00
$^{93}\text{Nb}(\gamma,n)^{92m}\text{Nb}$	8.966	9.713	6.861E-04	0.17	1.052E-10	0.28 \pm 0.00
$^{127}\text{I}(n,2n)^{126}\text{I}$	9.217	11.460	3.279E-01	3.16	9.892E-08	99.74 \pm 0.01
$^{127}\text{I}(\gamma,n)^{126}\text{I}$	9.144	9.773	1.690E-03	0.19	2.592E-10	0.26 \pm 0.01
$^{55}\text{Mn}(n,2n)^{54}\text{Mn}$	10.414	12.810	6.893E-02	2.48	2.080E-08	99.97 \pm 0.00
$^{55}\text{Mn}(\gamma,n)^{54}\text{Mn}$	10.227	12.810	3.523E-05	0.57	5.403E-12	0.03 \pm 0.00
$^{75}\text{As}(n,2n)^{74}\text{As}$	10.383	12.820	9.031E-02	6.03	2.725E-08	99.92 \pm 0.00
$^{75}\text{As}(\gamma,2n)^{74}\text{As}$	10.245	11.820	1.419E-04	0.42	2.176E-11	0.08 \pm 0.00
$^{89}\text{Y}(n,2n)^{88}\text{Y}$	11.612	13.780	4.816E-02	1.37	1.453E-08	99.94 \pm 0.00
$^{89}\text{Y}(\gamma,n)^{88}\text{Y}$	11.482	15.070	5.883E-05	0.89	9.021E-12	0.06 \pm 0.00
$^{19}\text{F}(n,2n)^{18}\text{F}$	10.986	13.880	2.252E-03	3.04	6.793E-10	99.87 \pm 0.00
$^{19}\text{F}(\gamma,2n)^{18}\text{F}$	10.432	12.030	5.968E-06	0.54	9.151E-13	0.13 \pm 0.00
$^{90}\text{Zr}(n,2n)^{89}\text{Zr}$	12.103	14.290	2.948E-02	1.08	8.895E-09	99.93 \pm 0.00
$^{90}\text{Zr}(\gamma,n)^{89}\text{Zr}$	11.968	15.190	4.802E-05	0.91	7.364E-12	0.08 \pm 0.00
$^{23}\text{Na}(n,2n)^{22}\text{Na}$	12.965	15.410	1.072E-03	1.54	3.235E-10	99.92 \pm 0.00
$^{23}\text{Na}(\gamma,2n)^{22}\text{Na}$	12.216	15.730	1.727E-06	1.09	2.648E-13	0.08 \pm 0.00
Competition between reactions (n,d+np) and (γ,p)						
$^{58}\text{Ni}(n,np+d)^{57}\text{Co}$	6.051	12.663	3.281E-02	0.28	9.898E-09	99.93 \pm 0.00
$^{58}\text{Ni}(\gamma,p)^{57}\text{Co}$	8.172	10.280	4.829E-05	0.28	7.404E-12	0.07 \pm 0.00
Competition between reactions (n, α) and ($\gamma,^3\text{He}$)						
$^{63}\text{Cu}(n,\alpha)^{60}\text{Co}$	0.000	7.008	1.416E-01	3.07	4.271E-08	100.00 \pm 0.00
$^{63}\text{Cu}(\gamma,^3\text{He})^{60}\text{Co}$	18.861	21.250	1.812E-20	99.92	2.779E-27	0.00 \pm 0.00
$^{54}\text{Fe}(n,\alpha)^{51}\text{Cr}$	0.000	6.909	2.560E-01	3.70	7.722E-08	100.00 \pm 0.00
$^{54}\text{Fe}(\gamma,^3\text{He})^{51}\text{Cr}$	19.734	21.250	9.211E-21	100.00	1.412E-27	0.00 \pm 0.00
$^{27}\text{Al}(n,\alpha)^{24}\text{Na}$	3.249	8.482	1.889E-01	0.74	5.700E-08	100.00 \pm 0.00
$^{27}\text{Al}(\gamma,^3\text{He})^{24}\text{Na}$	23.710	5.523	1.232E-08	0.03	1.889E-15	0.00 \pm 0.00
$^{51}\text{V}(n,\alpha)^{48}\text{Sc}$	2.095	10.420	9.113E-01	1.93	2.749E-07	100.00 \pm 0.00
$^{51}\text{V}(\gamma,^3\text{He})^{48}\text{Sc}$	22.631	-	-	-	-	-

Comparing different experiments, question could arise, whether the neutron spectrum doesn't differ in response to various critical levels in various arrangements. The critical level is dependent also on used instrumentation around core. It was shown [34], that the variations are negligible (see Figure 20) for studied arrangements (Table 7).

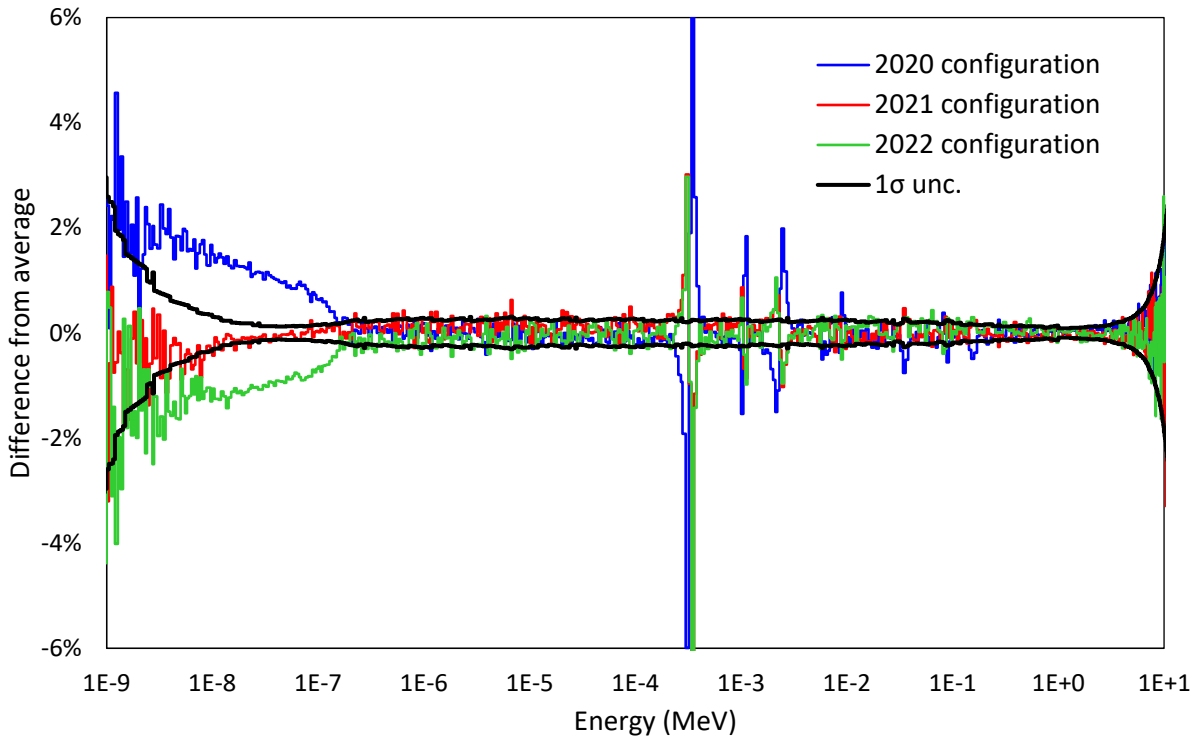


Figure 20: Comparison of MCNP calculated spectra in various special core arrangements together with related uncertainty (1σ uncertainty level).[34]

Table 7: Summary of various experiments with small foils used in SACS measurements.

	2020 configuration		2021 configuration		2022 configuration	
	Mean	Rel. unc.	Mean	Rel. unc.	Mean	Rel. unc.
Scaling (n/s)	7.96E+11	2.3%	6.90E+11	3.0%	7.93E+11	2.6%
Flux ($\text{cm}^{-2}\cdot\text{s}^{-1}$)	2.20E-4	0.1%	2.18E-4	0.1%	2.20E-4	0.0%
H_{cr} (cm)	53.553	0.01%	54.412	0.01%	53.800	0.01%
H_{ref} (cm)	21.750	0.05%	21.750	0.05%	22.300	0.04%

1.4 Characterization of the fission density profile

The neutron field in the developed reference benchmark neutron field is formed by neutrons emitted by the driver core. Due to this fact, the validation of the source term, namely spatial distribution of neutron emissivity is the valuable cross check of the previously validated spatial distribution of the neutron field in the reference volume because the neutron emission from fission is isotropic.

The neutron spectrum in the core differs only slightly case by case; thus, the concentration of fission products is nearly proportional to fission density at a defined point in fuel [36]. Due to this

proportionality, the concentration of fission products can be simply derived from their activity after a defined irradiation period (3). The details of the methodology can be found in [37].

This approach using single peak and fission products with well-defined fission yields was also reported in [38], [39]. It is also possible to measure the total gamma activity induced during irradiation [40]. In this approach, the relative fission density profile is derived by means of comparison with a reference fuel pin whose decay is monitored along with the measured one. The decay correction is determined semi-empirically because the wide integral consists of many peaks with various decay parameters, making an analytical solution unrealistic.

The details of the decay corrections used in the evaluation of fission density in a single peak can be found in equations (7 – (12). The time evolution is plotted in Figure 21.

$$F_j^i = \frac{NPA_j^i(t)}{\eta^i \cdot \varepsilon^i \cdot \lambda^i} \cdot \frac{1}{N^i(t)} = NPA_j^i(0) \cdot \frac{1}{\eta^i \cdot \varepsilon^i \cdot \lambda^i \cdot N^i(0)} \quad (7)$$

$$NPA_j^i(0) = NPA_j^i(t) \cdot \frac{1}{e^{-\lambda^i \cdot t}} \cdot \frac{\lambda^i \cdot \Delta T}{1 - e^{-\lambda^i \cdot \Delta T}} \quad (8)$$

Where:

F_j^i fission rate determined via the i-th nuclei and j-th pin; $N^i(t)$ the calculated number of observed nuclei in fuel pin when 1 fission/s occurs, in time t after irradiation end; $NPA_j^i(t)$ measured Net Peak Area j-th pin of the observed nuclei i and selected peak, λ^i decay constant of a selected nuclide; η^i efficiency of HPGe for the selected gamma line of the i-th nuclide; ε^i gamma branching ratio of the selected peak from observed nuclei i; t start j-th pin measurement; ΔT length of j-th pin HPGe measurement

During the measurement, the detector response depends on actual activity and apparatus sensitivity to the measured gamma photons as $Response = \int A(t) \times \varepsilon \times \eta \cdot dt$. The isotope activity decays by decay law as $A = A(0) \times e^{-\lambda \cdot t}$. By integration can be obtained:

$$\int A(t) \cdot dt = \int_0^{T_{measurement}} A_{Startup} \times e^{-\lambda \cdot t} dt = A_{Startup} \times \frac{1 - e^{-\lambda \cdot T_{meas.}}}{\lambda} \quad (9)$$

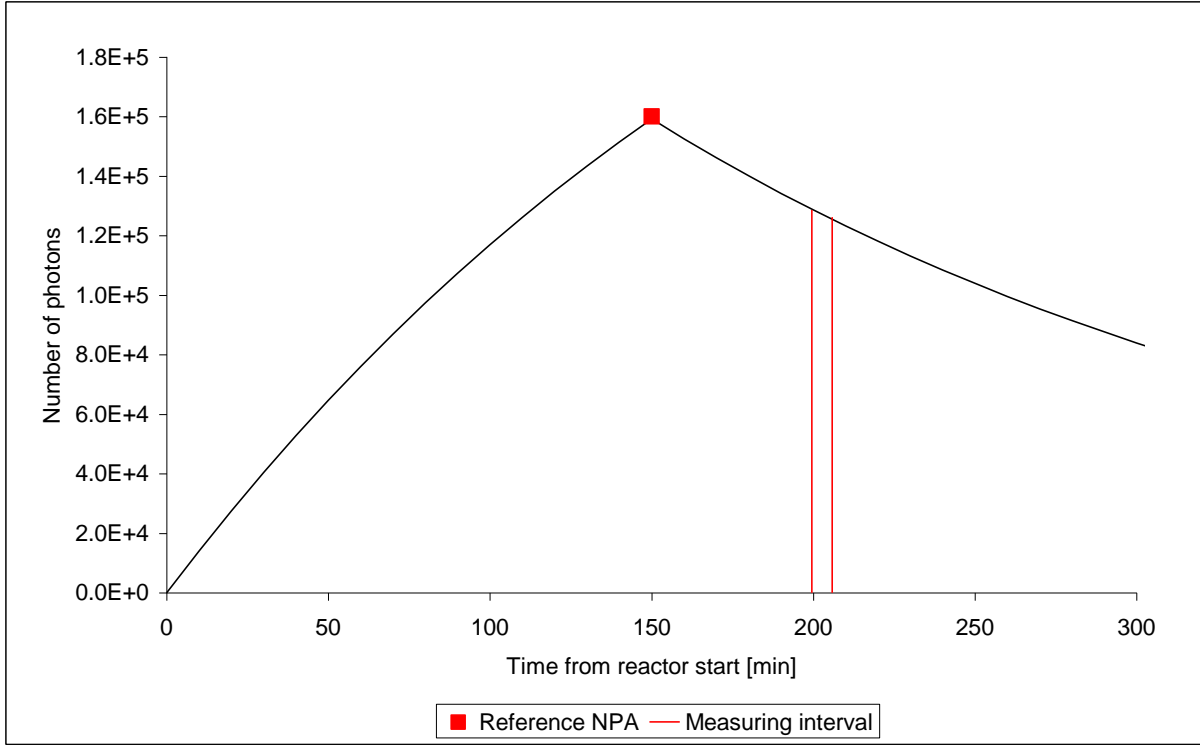


Figure 21: Time scheme of the measurement.

The correction factor, considering the decay compared with the non-decay case, is then obtained just by division by $A_{startup} \cdot T_{meas.}$. Thus the correction factor is:

$$\frac{\int A(t).dt}{A_{Startup} \times T_{measurement}} = \frac{1 - e^{-\lambda.T_{meas.}}}{\lambda \times T_{meas.}} \quad (10)$$

The second task is to determine a correction to decay between the start of measurement and the reference point. This correction is very simple, using the decay formula $N = N(0) \times e^{-\lambda.T}$, and it is reflected in equation (11). Similarly, as in the previous case, when half-life is very long, no correction is necessary, as the $-\lambda \times \Delta T$ approaches 0.

$$\frac{N^{REF}}{N_{startup}} = \frac{1}{e^{-\lambda.\Delta T}} \quad (11)$$

$$N_{ref} = N_{measured} \cdot \frac{1}{e^{-\lambda.\Delta T}} \times \frac{\lambda.T_{meas.}}{1 - e^{-\lambda.T_{meas.}}} \quad (12)$$

For correct determination of fission density, the correct determination of gamma activity is essential. Due to this demand, the characterization of HPGe [20] used in the fuel experiment was realized as well. The developed calculation model of used HPGe seems to be suitable, as related uncertainty is estimated from bias between standard and evaluated activity (see Figure 22, Figure 23).

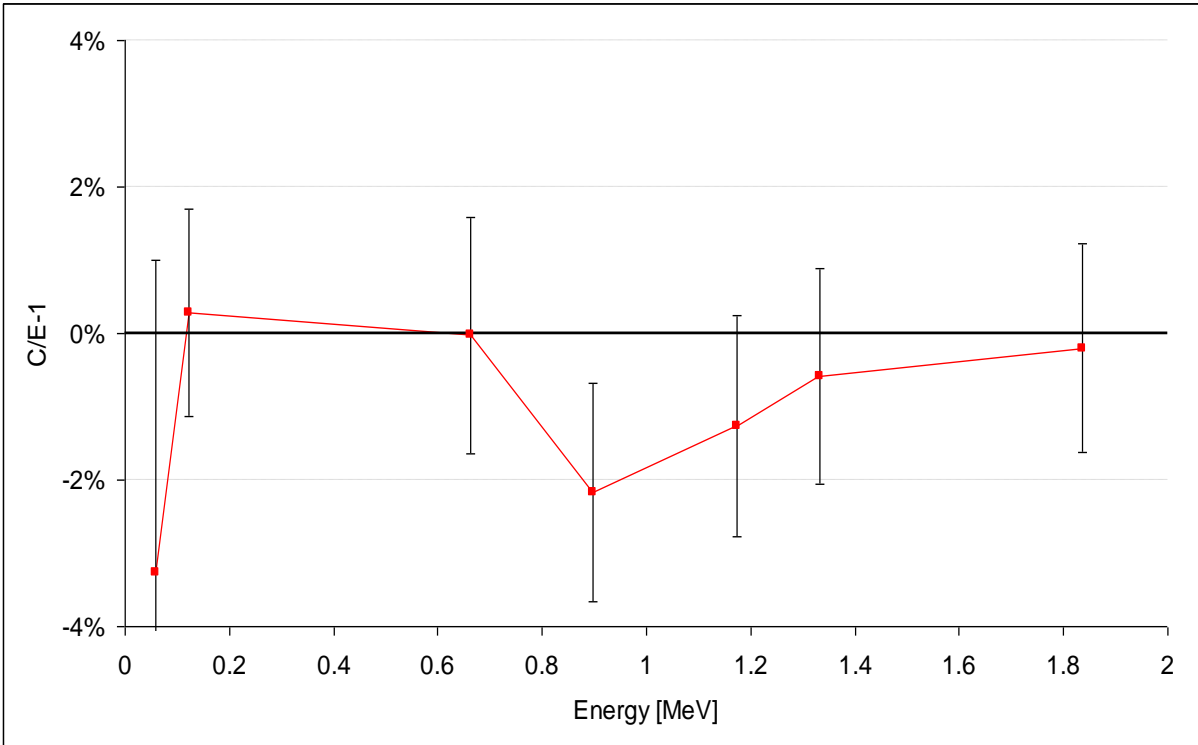


Figure 22: Validation of HPGe detector with etalon with a set of gamma emitters (^{252}Am , ^{57}Co , ^{60}Co , ^{137}Cs , ^{88}Y), etalon source in the middle of collimator slit, 11.5 cm from detector cap.

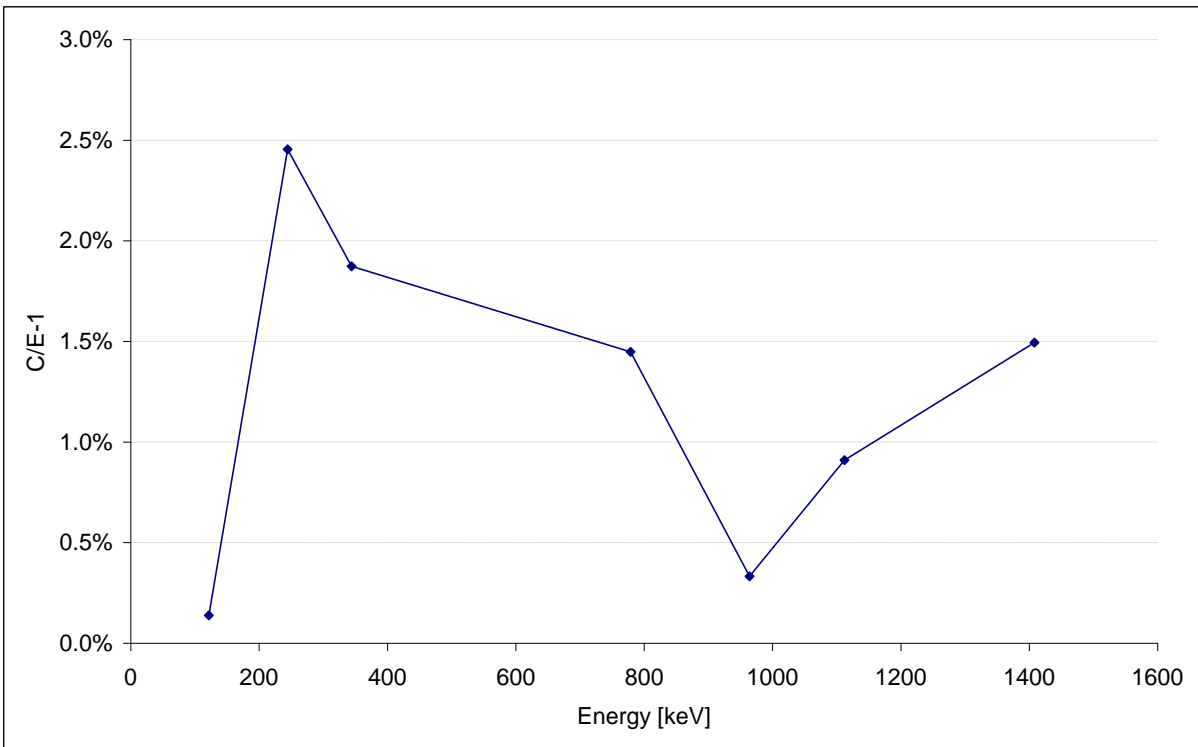


Figure 23: Validation of HPGe model with ^{252}Eu source in geometry where HPGe is out of shielding and point source is 11.5 cm from detector cap (the same distance 11.5 cm is between fuel pin and HPGe End Cap).

The methodology described above was applied to the studied case of driver core surrounding the reference volume (see Figure 24). The obtained results are in very good agreement with the theoretical prediction (see Figure 25). The fission densities usable in future benchmarking are in Table 8. Based on such agreement it can be concluded that the fission density in the calculation model of driver core is in good agreement with reality.

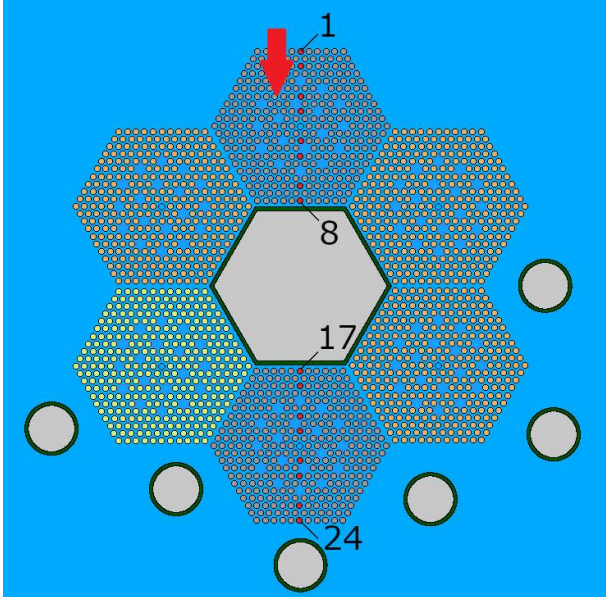


Figure 24: selection of pins where pin power was determined [41]

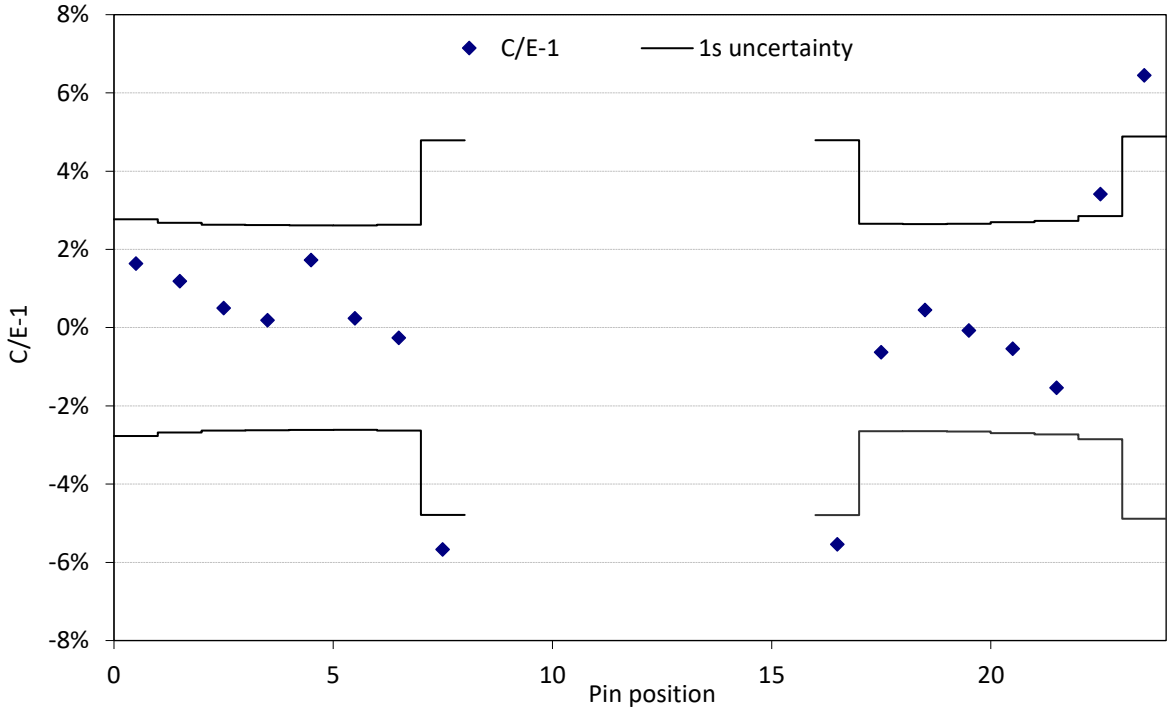


Figure 25: C/E-1 of fission density determined for selected pins [41]

This result is important because the spatial distribution of fission density confirms the spatial distribution of neutron flux in the central cavity because neutrons in reference volume are mostly

formed by transmitted or scattered fission neutrons. This validity of the driver core model also allows using the whole core in validation issues. This is valuable as round check issue in the testing of various evaluations of interesting materials. It was for example stainless steel which is important structural material [41], or silicon oxide which is important in space reactor technology or spent fuel management [42], because SiO₂ is the major component of earth crust and occurs in planetary rocks as well.

Table 8: Fission density distribution across core per 1 neutron, (Mn foils used in normalization)

Pin position	Row position	Y [cm]	Fission density [fiss/s/nps]	Rel. unc.
1	1	34.64	1.81E-04	2.8%
2	3	32.43	1.35E-04	2.7%
3	7	28.02	1.85E-04	2.6%
4	9	25.81	2.15E-04	2.6%
5	13	21.39	2.52E-04	2.6%
6	15	19.18	2.64E-04	2.6%
7	19	14.77	2.55E-04	2.6%
8	21	12.56	2.91E-04	2.6%
17	43	-12.56	2.89E-04	2.6%
18	45	-14.77	2.54E-04	2.7%
19	49	-19.18	2.59E-04	2.6%
20	51	-21.39	2.52E-04	2.7%
21	55	-25.81	2.12E-04	2.7%
22	57	-28.02	1.84E-04	2.7%
23	61	-32.43	1.25E-04	2.9%
24	63	-34.64	1.53E-04	2.8%

2 Reference neutron benchmark field for dosimetry cross section measurements

Due to an extremely well defined neutron field with defined critical parameters, the neutron flux spatial distribution, and neutron spectrum in the reference benchmark neutron field, along with the spatial distribution of fission density of driver core, the reference field was established [43]. Confirmation of low effect of (γ,n) reactions additionally to the conventional path allows to neglect this effect. Nonnegligible production from measured reactions is only in the case of $^{197}\text{Au}(n,2n)$ in which case, contribution of $^{197}\text{Au}(\gamma,n)$ to conventional $^{197}\text{Au}(n,2n)$ into total production of ^{196}Au is about 1 % which is much smaller than related uncertainties.

Because of the undistinguishable shape of the LR-0 reference field and $^{235}\text{U}(n_{\text{th}}, \text{fiss})$ PFNS [14], [22] in the region above 6 MeV the set of reaction rate was evaluated as spectral averaged cross section averaged in ^{235}U PFNS. The normalization is relatively simple, its principle is considering the share of identical tails in both spectra. Namely, in the evaluated ENDF/B-VIII.0 $^{235}\text{U}(n_{\text{th}}, \text{fiss})$ PFNS, about 2.566 % of total emitted neutrons have energy above 6 MeV. In the LR-0 spectrum only 0.714 % of neutrons have energy above 6 MeV. Thus, for determination of the SACS, the flux which is used for normalization of calculated RR must be divided by factor of 3.594 which reflects that a large amount of thermal and epithermal neutrons is added to the part of “true PFNS”.

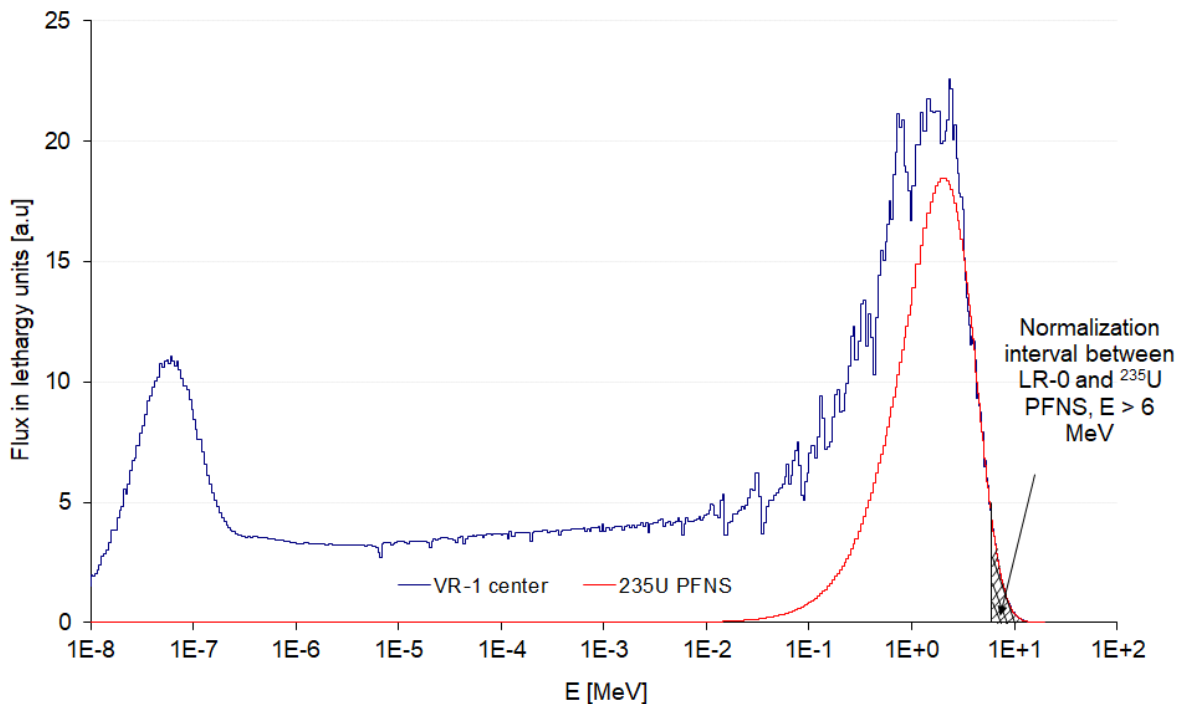


Figure 26: Graphical interpretation of similarity in LR-0 spectra and $^{235}\text{U}(n_{\text{th}},f)$ PFNS and following flux normalization.

Large set of reactions were measured (see Table 9) and using above mentioned approach they can be evaluated as a spectral averaged cross sections averaged in ^{235}U PFNS [33], [43],[44], [45], [46], [47].

Most of this data was adopted by a part of the IRDFF-II neutron dosimetry library [1]. They are used for improving cross sections because such data are usable in nuclear data evaluation [56].

Table 9: Summary of the. older experimental results.

	Critical water level (cm)	RR (s^{-1})	Scaling (n/s)	Normalized flux in target $E_n > 10$ MeV (cm^{-2})	Rel. unc.
$^{127}I(n,2n)$	56.08	2.785E-20	4.199E+11	7.727E-8	4.0%
$^{75}As(n,2n)$	57.36	6.395E-21	4.014E+11	6.769E-8	4.3%
$^{89}Y(n,2n)$	56.50	3.777E-21	4.037E+11	7.558E-8	3.2%
$^{19}F(n,2n)$	55.65	3.034E-22	7.316E+11	7.399E-8	4.0%
$^{90}Zr(n,2n)$	56.19	2.403E-21	3.821E+11	8.189E-8	4.0%
$^{23}Na(n,2n)$	57.20	9.327E-23	4.516E+11	7.182E-8	4.8%

The newly developed reference field was benchmarked [3], [44] and now is part of the IRPhEP database, thus the whole experimental set is available for improving and testing new nuclear data libraries. The reference field itself becomes part of the prestigious world database of reference benchmark neutron fields under the IRDFF-II database.

The large set of foils was measured in 2020, 2021 and 2022 (see Table 10) and detail of experimental setup in Table 7. The averaged values are in Table 11. The comparison with experiment is in Table 12. Using correction (Figure 26) in case of threshold reactions the SACS averaged in $^{235}U(n_{th},f)$ PFNS were evaluated and are listed in Table 13. The agreement with IRDFF-II data is excellent.

Table 15 presents SACS of $^{58}Ni(n,x)^{57}Co$ reaction averaged in $^{235}U(n_{th},f)$ PFNS and quite a large set of measurements is available. As the results are in satisfactory agreement with IRDFF-II description, this reaction can be recommended as a new dosimetry reaction. A new dosimetric reaction, $^{58}Ni(n,x)^{57}Co$, was recommended, which is especially valuable in fields with higher energy neutrons. Results obtained in VR-1 [59] and also in $^{252}Cf(s.f.)$ [60] validate the ENDF/B-VIII.0 evaluation for the $^{58}Ni(n,x)^{57}Co$ reaction as well. These current results are in previously reported measurements [52][51][49]. The suitable properties of this reaction make it a good candidate for the next update of the IRDFF library. This reaction will be beneficial for the reactor dosimetry field due to its long half-life and relatively high threshold, making it a good candidate for characterization of the high-energy neutron fields of accelerators [61].

The methodology developed in LR-0 was applied in the VR-1 Czech Technical University reactor. The set of data was used for testing of new neutron metrology library IRDFF-II [59]. The good agreement confirms a good correspondence of IRDFF-II with the experiment.

The reference field was also tested in combination with special filters [62]. This data will be benchmarked in the future.

Table 10: Summary of evaluated integral cross sections averaged in LR-0 spectrum.

Reaction	2020 configuration		2021 configuration		2022 configuration	
	Mean (b)	Rel. unc.	Mean (b)	Rel. unc.	Mean (b)	Rel. unc.
$^{58}\text{Fe}(n,\gamma)$	2.221E-1	3.0%	2.078E-1	4.1%		
$^{59}\text{Co}(n,\gamma)$			7.037E+0	4.1%		
$\text{Cd } ^{197}\text{Au}(n,\gamma)$					3.693E+1	3.8%
$\text{Cd } ^{23}\text{Na}(n,\gamma)$					8.231E-3	3.3%
$\text{Cd } ^{58}\text{Fe}(n,\gamma)$					3.265E-2	3.5%
$^{115}\text{In}(n,n')$			5.800E-2	4.0%	5.848E-2	3.4%
$^{47}\text{Ti}(n,p)$	5.008E-3	3.1%	4.995E-3	4.0%	4.995E-3	3.2%
$^{64}\text{Zn}(n,p)$			1.014E-2	4.0%	1.112E-2	3.4%
$^{58}\text{Ni}(n,p)$	2.955E-2	3.0%			2.949E-2	3.2%
$^{54}\text{Fe}(n,p)$	2.191E-2	3.5%			2.167E-2	3.2%
$^{92}\text{Mo}(n,p)^{92m}\text{Nb}$	1.928E-3	3.1%	1.949E-3	4.1%	1.914E-3	3.4%
$^{46}\text{Ti}(n,p)$	2.981E-3	3.0%			2.984E-3	3.2%
$^{60}\text{Ni}(n,p)$			5.393E-4	7.2%	6.214E-4	5.9%
$^{63}\text{Cu}(n,\alpha)$	1.405E-4	3.5%			1.382E-4	4.2%
$^{54}\text{Fe}(n,\alpha)$					2.423E-4	10.5%
$^{56}\text{Fe}(n,p)$	2.974E-4	3.1%	2.864E-4	4.5%	2.926E-4	3.5%
$^{48}\text{Ti}(n,p)$	8.070E-5	3.2%	7.982E-5	5.0%	8.230E-5	3.2%
$^{24}\text{Mg}(n,p)$					3.929E-4	4.6%
$^{27}\text{Al}(n,\alpha)$	1.873E-4	3.6%	1.872E-4	4.3%	1.902E-4	3.4%
$^{51}\text{V}(n,\alpha)$	6.345E-6	3.3%			6.652E-6	3.9%
$^{197}\text{Au}(n,2n)$	9.382E-4	4.0%				
$^{93}\text{Nb}(n,2n)^{92m}\text{Nb}$	1.165E-4	3.3%	1.197E-4	4.1%	1.233E-4	3.5%
$^{55}\text{Mn}(n,2n)$					6.466E-5	4.5%
$^{58}\text{Ni}(n,x)^{57}\text{Co}$	6.30E-05	13%	6.30E-05	6%	6.81E-05	6%

Table 11: SACS averaged in LR-0 spectrum evaluated using the calculated neutron flux approach.

Reaction	Mean (b)	Unc.
$^{58}\text{Fe}(n,\gamma)$	2.150E-1	4.2%
$^{59}\text{Co}(n,\gamma)$	7.037E+0	4.1%
Cd $^{197}\text{Au}(n,\gamma)$	3.693E+1	3.8%
Cd $^{23}\text{Na}(n,\gamma)$	8.231E-3	3.3%
Cd $^{58}\text{Fe}(n,\gamma)$	3.265E-2	3.5%
$^{115}\text{In}(n,n')$	5.824E-2	2.7%
$^{47}\text{Ti}(n,p)$	4.999E-3	2.0%
$^{64}\text{Zn}(n,p)$	1.063E-2	5.3%
$^{58}\text{Ni}(n,p)$	2.952E-2	2.2%
$^{54}\text{Fe}(n,p)$	2.179E-2	2.4%
$^{92}\text{Mo}(n,p)^{92m}\text{Nb}$	1.930E-3	2.2%
$^{46}\text{Ti}(n,p)$	2.983E-3	2.2%
$^{60}\text{Ni}(n,p)$	5.803E-4	8.5%
$^{63}\text{Cu}(n,\alpha)$	1.394E-4	2.9%
$^{54}\text{Fe}(n,\alpha)$	2.423E-4	10.5%
$^{56}\text{Fe}(n,p)$	2.921E-4	2.6%
$^{48}\text{Ti}(n,p)$	8.094E-5	2.6%
$^{24}\text{Mg}(n,p)$	3.929E-4	4.6%
$^{27}\text{Al}(n,\alpha)$	1.882E-4	2.3%
$^{51}\text{V}(n,\alpha)$	6.498E-6	3.5%
$^{197}\text{Au}(n,2n)$	9.382E-4	4.0%
$^{93}\text{Nb}(n,2n)^{92m}\text{Nb}$	1.198E-4	3.1%
$^{127}\text{I}(n,2n)$	3.276E-4	4.0%
$^{55}\text{Mn}(n,2n)$	6.466E-5	4.5%
$^{75}\text{As}(n,2n)$	8.982E-5	4.3%
$^{89}\text{Y}(n,2n)$	4.724E-5	3.2%
$^{19}\text{F}(n,2n)$	2.139E-6	4.0%
$^{90}\text{Zr}(n,2n)$	2.931E-5	4.0%
$^{23}\text{Na}(n,2n)$	1.097E-6	4.8%
$^{58}\text{Ni}(n,x)^{57}\text{Co}$	6.469E-5	6.4%

In reactions marked Cd foils were covered by Cd layer.

Table 12: C/E-1 of SACS averaged in LR-0 spectrum compared with various calculations.

	MCNP 6.2		TRIPOLI	
	IRDFF-II	ENDF/B-VIII.0	IRDFF-II	JEFF-3.1.1
$^{58}\text{Fe}(n,\gamma)$	2.9%	3.2%	1.0%	0.9%
$^{59}\text{Co}(n,\gamma)$	4.6%	4.6%	3.1%	3.4%
$\text{Cd } ^{197}\text{Au}(n,\gamma)$	-1.1%	-	-0.7%	0.2%
$\text{Cd } ^{23}\text{Na}(n,\gamma)$	5.0%	5.4%	5.1%	3.3%
$\text{Cd } ^{58}\text{Fe}(n,\gamma)$	4.4%	6.1%	7.7%	7.7%
$^{115}\text{In}(n,n')$	-4.0%	-	-3.2%	-
$^{47}\text{Ti}(n,p)$	1.6%	7.3%	2.6%	9.3%
$^{64}\text{Zn}(n,p)$	-0.1%	-9.5%	0.9%	3.5%
$^{58}\text{Ni}(n,p)$	0.1%	-1.0%	1.2%	1.6%
$^{54}\text{Fe}(n,p)$	-1.9%	-1.9%	-0.7%	-10.1%
$^{92}\text{Mo}(n,p)^{92\text{m}}\text{Nb}$	-6.1%	-	-4.3%	-
$^{46}\text{Ti}(n,p)$	2.3%	-6.2%	4.7%	1.7%
$^{60}\text{Ni}(n,p)$	-0.1%	-7.1%	2.8%	3.0%
$^{63}\text{Cu}(n,\alpha)$	1.6%	45.4%	4.4%	2.1%
$^{54}\text{Fe}(n,\alpha)$	5.7%	-16.2%	8.1%	-42.4%
$^{56}\text{Fe}(n,p)$	-0.3%	-0.3%	2.7%	0.9%
$^{48}\text{Ti}(n,p)$	-0.2%	17.1%	2.2%	-8.2%
$^{24}\text{Mg}(n,p)$	1.6%	10.6%	4.3%	13.7%
$^{27}\text{Al}(n,\alpha)$	0.4%	2.3%	2.9%	4.8%
$^{51}\text{V}(n,\alpha)$	1.4%	8.7%	2.1%	2.3%
$^{197}\text{Au}(n,2n)$	-2.9%	-7.6%	-2.8%	-7.7%
$^{93}\text{Nb}(n,2n)^{92\text{m}}\text{Nb}$	4.2%	-	3.0%	-
$^{127}\text{I}(n,2n)$	0.1%	1.5%	-1.7%	8.7%
$^{55}\text{Mn}(n,2n)$	6.7%	4.5%	0.4%	2.7%
$^{75}\text{As}(n,2n)$	0.6%	3.5%	-5.4%	-12.0%
$^{89}\text{Y}(n,2n)$	2.1%	3.2%	-7.5%	-8.0%
$^{19}\text{F}(n,2n)$	5.6%	26.6%	-4.9%	14.4%
$^{90}\text{Zr}(n,2n)$	0.9%	2.9%	-10.7%	-5.0%
$^{23}\text{Na}(n,2n)$	-1.5%	55.2%	-16.6%	-17.4%
$^{58}\text{Ni}(n,x)^{57}\text{Co}$	-	-4.4%	-	-9.1%

In reactions marked Cd foils were covered by Cd layer.

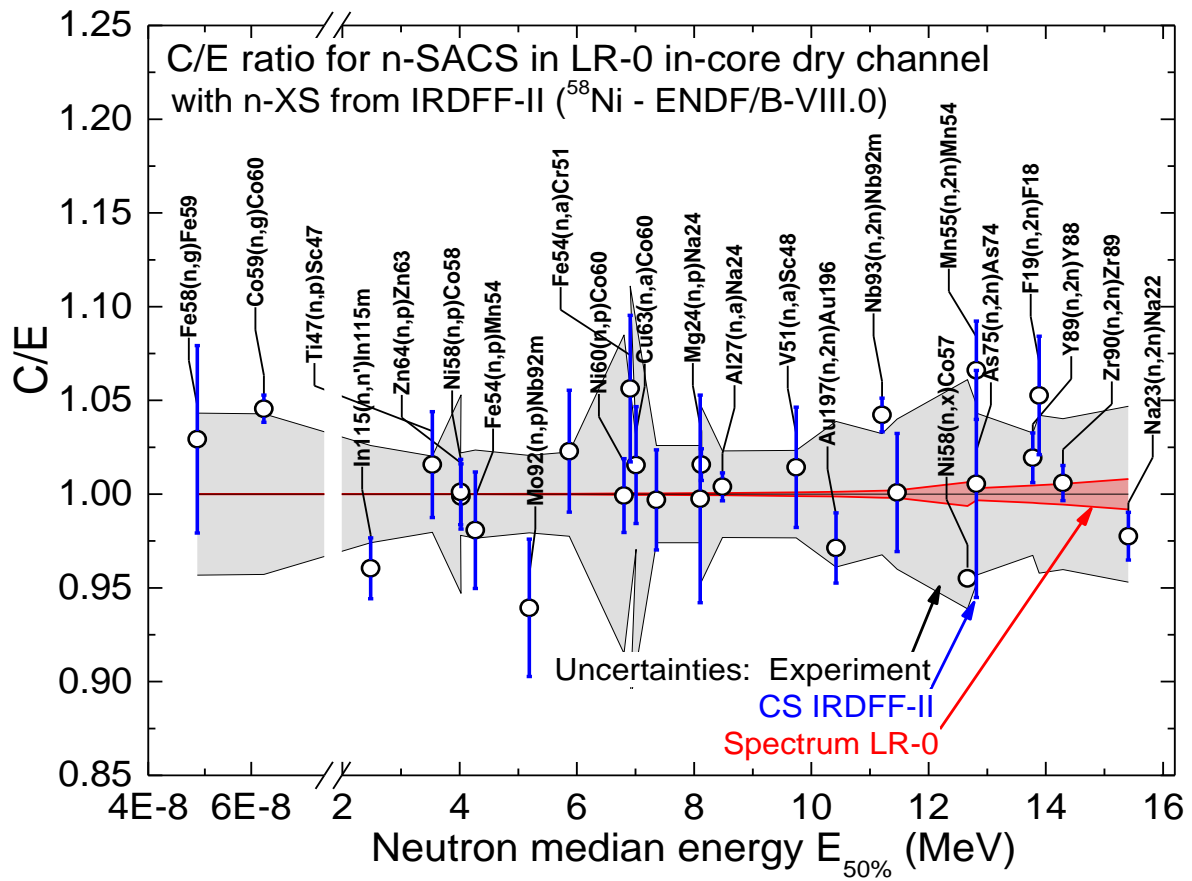


Figure 27: C/E ratio for the neutron induced spectrum average cross sections (n-SACS) versus the neutron median energy $E_{50\%}$. The gray corridor area shows the total experimental uncertainties, the blue columns – the total uncertainties from IRDFF-II, the red area – the statistics of the simulated neutron spectrum. Note the change in scale of the abscissas at neutron energies below 2 MeV.

Table 13: Summary of SACS corrected to $^{235}\text{U}(n_{\text{th}}, f)$ PFNS and compared with IRDFF-II data.

	Threshold energy (MeV)	SACS (mb)	Rel. unc.	Eval./E-1
$^{115}\text{In}(n,n')$	0	209.3	2.7%	-10.3%
$^{47}\text{Ti}(n,p)$	0	17.97	2.0%	-0.7%
$^{64}\text{Zn}(n,p)$	0	38.21	5.3%	1.8%
$^{58}\text{Ni}(n,p)$	0	106.1	2.2%	2.0%
$^{54}\text{Fe}(n,p)$	0	78.33	2.4%	-0.3%
$^{92}\text{Mo}(n,p)$	0	6.938	2.2%	-3.6%
$^{46}\text{Ti}(n,p)$	1.619	10.72	2.2%	7.4%
$^{60}\text{Ni}(n,p)$	2.075	2.086	8.5%	4.5%
$^{63}\text{Cu}(n,\alpha)$	0	0.5009	2.9%	3.3%
$^{54}\text{Fe}(n,\alpha)$	0	0.8707	10.5%	-0.7%
$^{56}\text{Fe}(n,p)$	2.966	1.050	2.6%	2.8%
$^{48}\text{Ti}(n,p)$	3.274	0.2909	2.6%	3.6%
$^{24}\text{Mg}(n,p)$	4.932	1.412	4.6%	2.6%
$^{27}\text{Al}(n,\alpha)$	3.25	0.6764	2.3%	3.6%
$^{51}\text{V}(n,\alpha)$	2.093	0.0234	3.5%	4.0%
$^{197}\text{Au}(n,2n)$	8.114	3.372	4.0%	0.4%
$^{93}\text{Nb}(n,2n)$	9.064	0.4307	3.1%	0.9%
$^{127}\text{I}(n,2n)$	9.217	1.177	4.0%	1.8%
$^{55}\text{Mn}(n,2n)$	10.414	0.2324	4.5%	0.0%
$^{75}\text{As}(n,2n)$	10.384	0.3228	4.3%	-1.1%
$^{89}\text{Y}(n,2n)$	11.611	0.1698	3.2%	0.8%
$^{19}\text{F}(n,2n)$	10.986	0.00769	4.0%	5.9%
$^{90}\text{Zr}(n,2n)$	12.1	0.1053	4.0%	-0.7%
$^{23}\text{Na}(n,2n)$	12.965	0.00394	4.8%	-1.9%
$^{58}\text{Ni}(n,x)^{57}\text{Co}$	6.051	0.2325	6.4%	2.5% ^a

^a this reaction is not in IRDFF-II, thus data are from ENDF/B-VIII.0

Table 14: Comparison between actually measured $^{58}\text{Ni}(n,x)^{57}\text{Co}$ SACS averaged in $^{235}\text{U}(n_{\text{th}}, f)$ and previously measured results.

Reference	Mean (mb)	Eval./E-1
[48]	0.216 ± 0.005	-7.1 %
[49]	0.240 ± 0.035	3.2 %
[50]	0.232 ± 0.005	-0.2 %
[51]	0.253 ± 0.015	8.8 %
[52]	0.275 ± 0.015	18.3 %
[45]	0.239 ± 0.013	2.8 %
[53]	0.241 ± 0.015	3.7 %
[54]	0.226 ± 0.010	-2.9 %

3 Spectrum averaged cross-sections

The cross section averaged over ^{235}U fission spectrum is a fundamental quantity that can be used in the evaluation of nuclear data. Many experiments focused on the determination of Spectral Averaged Cross Sections (SACS) weighted in ^{235}U Prompt Fission Neutron Spectrum (PFNS) were performed in light water reactors using enriched uranium fuel. In these reactors, already some amount of water moderator is between the uranium fuel and the irradiated sample. Due to the decreasing character of hydrogen cross-section, the high energy tail of the reactor spectrum in cores with water moderators may be harder than the pure prompt fission neutron spectrum at some specific conditions. This is, for the example, case of VR-1 reactor (see Figure 28).

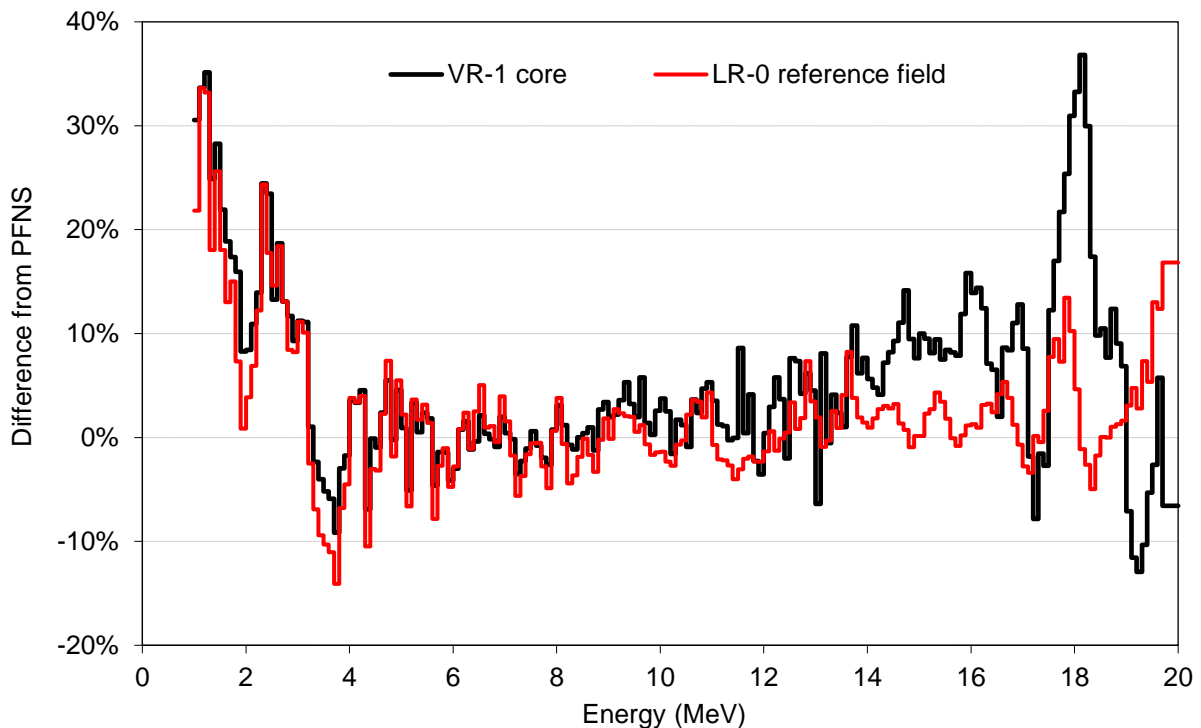


Figure 28: Comparison of VR-1 and LR-0 reactor spectra with ^{235}U PFNS.

The figure demonstrates the fact, that whereas LR-0 spectrum is close to ^{235}U fission spectrum, the VR-1 shows some differences in the region above 14 MeV. These differences in the high-energy tail of the fission spectrum in the LR-0 and VR-1 reactors compared to the pure ^{235}U prompt fission neutron spectrum can be explained by the differences in the macroscopic cross sections of the homogenized cores (see Figure 29). The total cross section of the homogenized LR-0 core is higher compared to VR-1. Also, the VR-1 homogenized cross section has decreasing character in the region above 15 MeV. The combination of both facts causes a non-negligible decrease in interaction rates with increasing energy in the VR-1. The situation in LR-0 is different because the cross section is nearly constant, and the oscillations from the average cross section are relatively lower (in percentage terms); thus, the interaction rate is nearly constant. This fact is propagated in nearly constant energy-dependent attenuation of high energy neutrons (> 10 MeV) in the LR-0, while in the VR-1, it decreases. Based on this fact a harder tail of spectrum above 15 MeV in the VR-1 reactor can be expected.

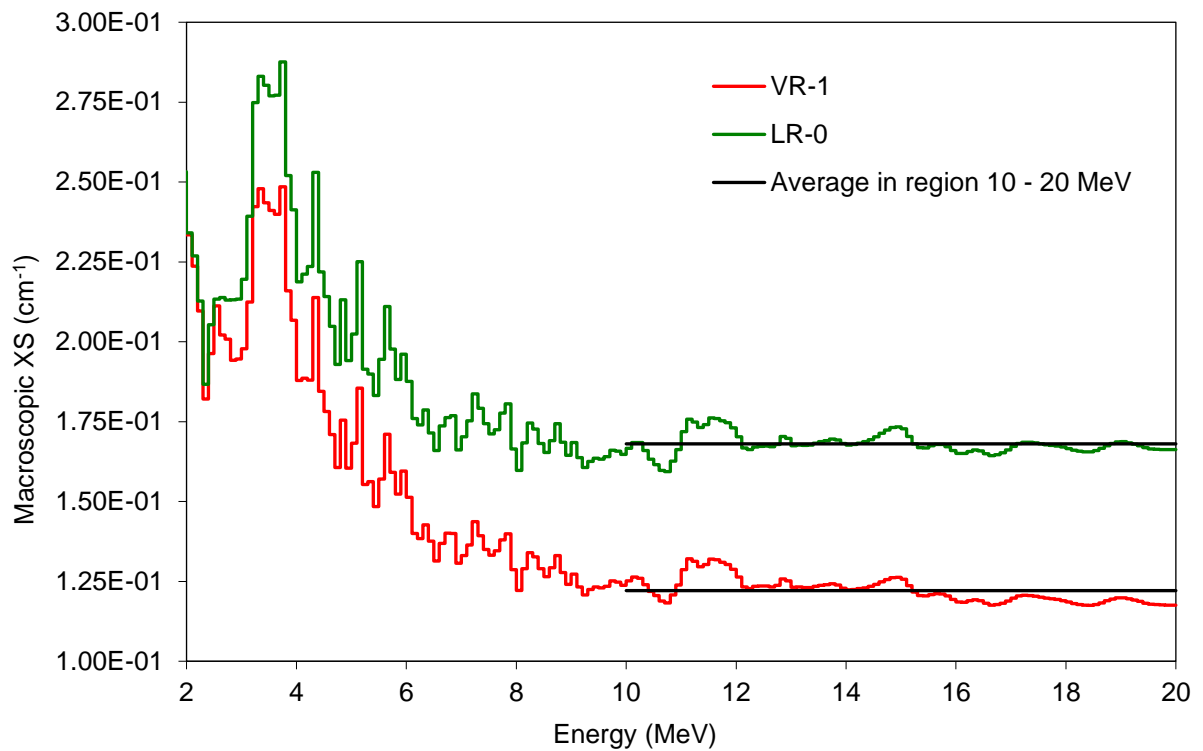


Figure 29: Macroscopic cross sections of VR-1 and LR-0 cores (ENDF/B-VIII.0 data [55])

The above presented shows the importance of the International Nuclear Data Committee conclusion that the purity of high energy tail of reactor spectrum must be ensured prior to evaluation as ^{235}U PFNS [56]. The same report also states that spectrum averaged cross sections in fast spectrum in reactors where reference spectrum is not defined are more suitable for data verification/validation rather than for the adjustment. Their usefulness depends on the accuracy with which the spectrum is known. Ideally, it should be supplied with the full covariance matrix, or at least the uncertainties. It is the reason why integral cross section data from VR-1 reactor [53] or LVR-15 reactor were used for validation and verification of neutron dosimetry cross sections.

4 Pile noise experiment

For safety reasons, it is important to correctly predict the kinetic behavior of LWRs in nominal or incidental situations. When a nuclear reactor is near criticality, the delayed neutron (DN) kinetics drive the neutron production. Integral parameters, such as the reactor reactivity, are calculated by computational tools which make the use of nuclear data library. To compare these calculation results to the experimental values, it is possible to use nuclear research reactors at low power in well characterized configurations.

In the past years, CEA has been leading research activities focusing on producing better evaluations of delayed neutron nuclear data, by means of summation calculations, microscopic measurements, or reactor measurements. The pile noise experiment was realized in LR-0 as well [65]. "Pile noise" refers to a set of techniques to derive the transfer function of a nuclear reactor from the measurement of low frequency correlations in signals issued by neutron detectors. By fitting on a point kinetic model, the prompt decay constant (α_p) can be obtained as well as the delayed neutron fraction (β_{eff}) and prompt neutron generation time (Λ), if the reactor fission rate is known. The reactor integral fission rate, which was required to estimate the delayed neutron fraction, was obtained by metal foils activation. CVR derived saturated activities by gamma spectrometry on several metallic foils (Al + 1 % gold, Al + 0.1 % gold, nickel and cobalt)

The core was surrounded by eight dry channels used for instrumentation and power monitoring. This configuration was not symmetrical since one FA had a 3.28 % enrichment, two had a 3.29 % enrichment and the others had a 3.30 % enrichment. The uncertainty on the enrichment is 0.01 wt%.

Two dry tubes, labelled A and B, were loaded with the pile noise fission chambers. Tube A stayed fixed during all the experiments. Tube B was progressively moved away from the core up to 20 cm.

4.1 Detectors and acquisition systems

Two KNK15 fission chambers (containing 0.5 g of ^{235}U , sensitivity around 0.5 (c/s)/n/cm²/s), were put in the dry channels A & B. In the following, they are referred to as Detector 1 and Detector 2. They have a diameter of 50 mm and a height of 205 mm. The precise internal geometry of the chambers is not known. Note that this is not a problem for the modelling of the experiment as the detectors do not significantly alter the neutron flux, especially when they are put in dry tubes. The fissile deposit is supposed to be centered at the mid-plane of the chambers. The precision on its location is around ~10 mm, which also has a limited impact on the modelling since the deposit is long (probably around 15 cm).

Detector 1 was placed in dry tube B, which was mobile in the reflector, whereas Detector 2 was located in the core center (except during the metal foil irradiation). They were placed at the maximum flux plan level, with their center at a height of 225.5 mm (± 3 mm) from the bottom of the fissile column.

Dry tube B was positioned thanks to marks drawn beforehand by the reactor operating team (see Figure 30). The position "0" corresponds to a contact of the dry tube with the feet of the two closest assemblies. For this position, the distance between the surface of the tube and the nearest pins is 8 mm \pm 1.5 mm. Other instrumented dry tubes (like the tube labelled "MK" on Figure 30, left) are 40 mm away from the nearest pins of the fuel assemblies.

The CEA-developed acquisition system SPECTRON was used to digitize the neutron signals. They were processed and analyzed in the frequency domain, using the so-called cross-power spectrum method. The system's sampling frequency is 78 kHz and it can compute on line the power spectra as well as display the detectors' currents for monitoring.

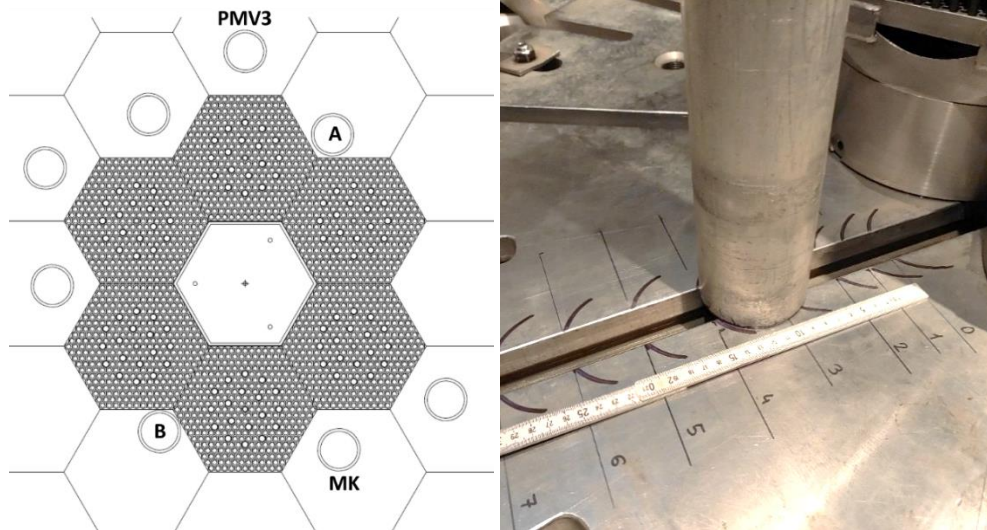


Figure 30: Left: section views of the LR-0 reference core geometry. The dry tubes labelled A and B were loaded with fission chambers for the purpose of the experiment. The tubes labelled PMV3 and MK contained neutron flux monitors. Right: Picture of the bottom of the movable dry tube B.

4.2 Irradiation runs and flux monitoring

The experimental campaign was divided into nine irradiation runs. Eight runs (run n°1 to run n°8) can be considered independent, as the reactor was shut down for a change in the core configuration. The last two runs (n°8 and n°9) were done consecutively, at two reactor powers, without shutting down the reactor. They are nonetheless considered independent in the analysis.

Table 15 gives an overview of the configuration for each run. Runs are classified as “symmetrical”, when the two detectors were in opposite positions, and “non-symmetrical”, when Detector 2 was in the core center channel. The monitoring signals of two neutron flux detectors were recorded to allow rescaling the reactor power from one run to the other. “MK” refers to a boron chamber (current recorded in nA) and “PMV3” refers to a boron lined counter (signal in c/s). The average currents of the two fission chambers are also indicated along with their position.

The current of Detector 1 shows an expected decreasing trend when it was moved away from the fuel. From Detector 2 (runs n°2 to n°7), one can calculate a relative spread of 0.2 %, which indicates a very good reproducibility of the irradiation conditions. This is also in good agreement with the preliminary calculations that showed that the change in the position of Detector 1 would not affect the flux in the central channel. Design calculations showed that the maximum variation in detection rate in instrumented tubes is below 1 % (Figure 31).

Table 15. Core configuration of the irradiation runs.

Configuration	Run	Center	Duration (min)	LR-0 Monitoring		Detector 1			Detector 2	
				MK (nA)	PMV3 (kc/s)	Position	Distance (cm)	Signal (μ A)	Position	Signal (μ A)
Symmetrical	1	∅	20	507.80	359.7	Tube B	0	0.801	Tube A	0.884
Symmetrical	8	Holder	120	512.70	360.7	Tube B	0	0.747	Tube A	0.881
Symmetrical	9	Holder	120	3334.10	2282	Tube B	0	4.915	Tube A	5.768
Non sym.	2	Det2	45	517.60	360.9	Tube B	0	0.811	Center	0.665
Non sym.	7	Det2	45	517.00	361.7	Tube B	2.5	0.897	Center	0.661
Non sym.	6	Det2	45	516.70	363.7	Tube B	5	0.798	Center	0.663
Non sym.	3	Det2	45	515.60	363.6	Tube B	10	0.390	Center	0.662
Non sym.	4	Det2	45	514.30	362.0	Tube B	15	0.150	Center	0.661
Non sym.	5	Det2	45	515.90	362.5	Tube B	20	0.055	Center	0.663

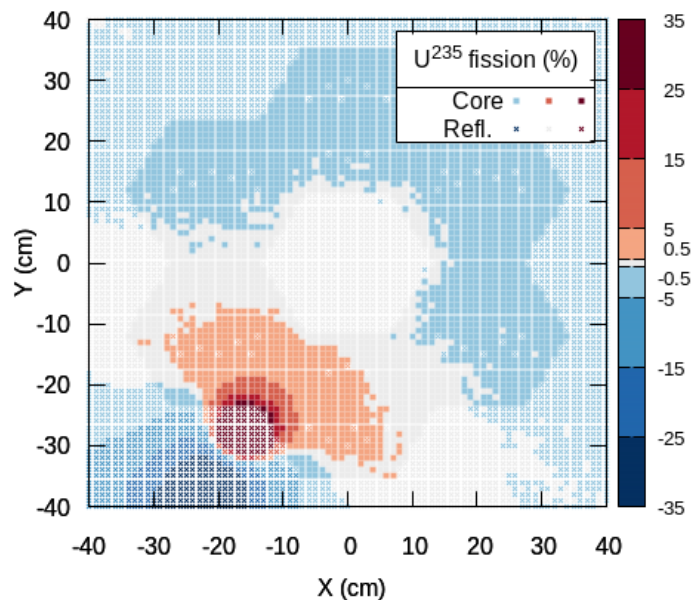


Figure 31: Variation of the microscopic ^{235}U fission rate between two positions of dry tube B: 20 cm (run 5) and 0 cm (run 2). Square symbols in fuel and cross symbols in reflector.

Runs n°8 and n°9 correspond to the metal foil irradiation, so the core central channel was loaded with the foil's holder. This device, made of aluminum tubing, is not supposed to have any influence on the flux levels. It was indeed observed that Detector 2 and PMV3 do not vary from run n°1 to run n°8. Contrarily, there is a small, but significant, 1 % difference on MK signal. This detector also shows a slight variation from run n°1 to run n°2, whereas PMV3 does not vary. We conclude here that Detector MK was not perfectly reliable and that PMV3 (or Detector 2 when possible) is preferred for rescaling the reactor power.

Between runs n°8 and n°9, the reactor power was multiplied by a factor of 6 approximately. At this power, detector PMV3 counting rate was so high that it was not perfectly linear due to dead time, showing a 3.3 % bias. For run n°9, the signal from Detector 2 was used to rescale the power level.

Finally, there is an unexplained 7 % difference between levels registered by Detector 1 during run n°1 and n°8. As it will be shown in the following, the data analysis was still correct, but the results from Detector 1 for these two runs are suspicious.

The central dry channel was used either to insert a fission chamber or the dosimeter foils holder (see Figure 32). The foils were located at $z = 246 \text{ mm} \pm 3 \text{ mm}$ relatively to the bottom of the fissile column, which was close to the core maximum flux plane in the position where the reference neutron field was identified [43]. The post-irradiation gamma spectrometry was carried out by CVŘ with a high purity Germanium detector (HPGe). Based on the mass activities, the following reaction rates (RR) were obtained: $^{197}\text{Au}(n,g)$, $^{56}\text{Fe}(n,p)$ and $^{58}\text{Ni}(n,p)$. Table 16 gives the ratio of the mass activity to the saturate activity (The saturated mass activity normalized per activated nuclei is equal to the microscopic reaction rate.) For the aluminum-gold alloy foil (Al + 0.1% Au), the value was averaged over the two metal foils.

By comparing measured reaction rates with those calculated with TRIPOLI-4®, the integral fission rate of the core was derived. Run n°9 was used as the reference because around 90 % for the neutron fluence came from it. The integral fission rate was estimated to be $2.72 \times 10^{11} \text{ f/s}$, which corresponds to a reactor power of 8.7 W. Using the average signals issued by Detector PMV3 and Detector 2, the integral fission rate of each run was rescaled to the one run n 9. The overall relative uncertainty on the integral fission rate was estimated at 1.5 % (1σ). It is driven by the efficiency calibration of the gamma spectrometry chain.



Figure 32. View of the metal foils fixed to the aluminum holder.

Table 16. Metal foils activities (in proportion of saturated activities), reactions rates and average core fission rate during Run n°9.

Reaction	Activity / saturated act. (%)	Calculated RR per n. source (s^{-1})	Measured RR (s^{-1}) ^a	Neutron emission rate ($\times 10^{11} \text{ n/s}$) ^b
$^{56}\text{Fe}(n,p)$	57.81	6.61×10^{-32}	4.41×10^{-20}	6.67(13)
$^{58}\text{Ni}(n,p)$	0.13	6.72×10^{-30}	4.45×10^{-18}	6.62(12)
$^{197}\text{Au}(n,g)$	3.46	1.12×10^{-26}	7.55×10^{-15}	6.72(13)
Average neutron emission rate				6.63(9)
Average core fission rate in Run n°9 :		$2.72 (4) \times 10^{11} \text{ f/s}$		

^a Average reaction rate during irradiation

^b Ratio of measured over calculated reaction rate = average number of source neutrons

4.3 Power spectral densities and associated uncertainties

The raw signals recorded by SPECTRON were processed to produce power spectrum densities (PSDs). Before applying the Welch method (without windowing), the signals were decimated by a factor of 27, which is equivalent to resample the signal at a frequency of 610 Hz. PSDs obtained from one signal are called auto-PSD (APSD), whereas those obtained from two signals are called cross-PSD (CPSD). Let x and y be two time series of duration T , sampled at frequency F_s . Let TF and TF^* be the fast Fourier transform operator and its complex conjugate and let $\langle \cdot \rangle_N$ be the average operator over N timeframes processed, then:

$$CPSD(x, y) = \frac{2}{T \cdot F_s} |\langle TF(x) \cdot TF^*(y) \rangle_N| \quad (1)$$

$$APSD(x) = \frac{2}{T \cdot F_s} |\langle TF(x) \cdot TF^*(x) \rangle_N| = \frac{2}{T \cdot F_s} \langle |TF(x)|^2 \rangle_N \quad (2)$$

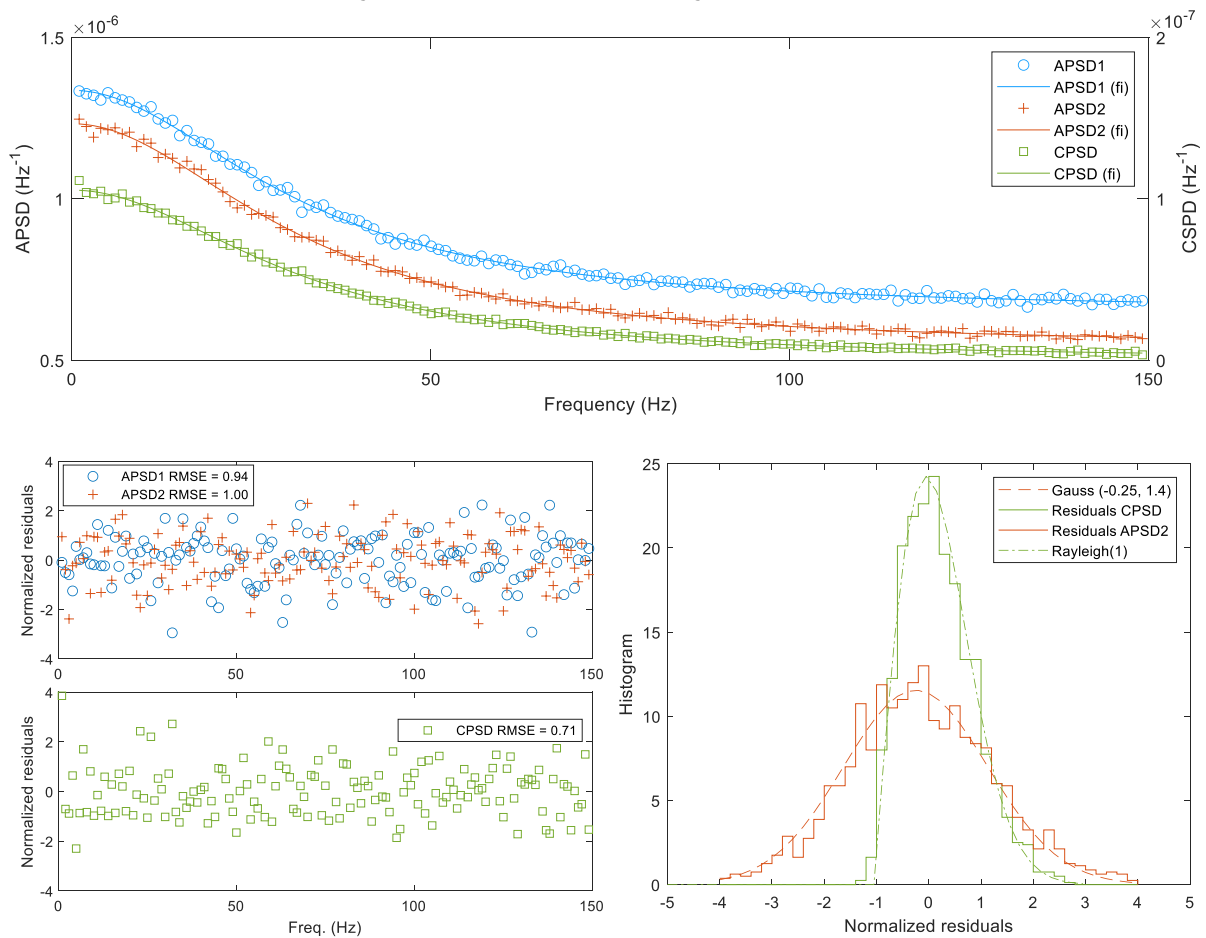


Figure 33 : APSDs and CPSD from run 8 (top) and residuals associated to the fit (bottom left). The distributions of residuals from APSD and CPSD are different (bottom right).

A good approximation of the relative standard deviation of an APSD was $1/\sqrt{N}$, where N is the number of timeframes. For CPSD, the relative standard deviation was taken equal to $0.5/\sqrt{N}$. After the fit process, the residuals can give information on the statistics of the errors. The APSDs and CPSD obtained from run n°8 are displayed in Figure 33. As expected, the CPSD tends to zero when frequency tends to infinite but stays positive. The residuals of the fit do not show any trend and the root mean square error (RMSE) values of APSD fits are close to 1. The residuals distribution are shown of the bottom

right. A zero centered Gaussian curve fits nicely the APSD residuals. On the contrary, the residuals of the CPSD are not Gaussian-shaped but are better fitted with a Rayleigh distribution of parameter $\sigma = 1$. The probability density function of the Rayleigh distribution is $f(x) = \frac{x}{\sigma^2} e^{-x^2/(2\sigma^2)}$.

4.4 Analytical model, data fitting and reproducibility

In the point kinetics model, the reactor response function (or zero power transfer function) is a complex analytical model which embeds delayed neutron parameters as well as the prompt neutrons generation time and the reactivity. When interested in the prompt neutrons response, it is standard to simplify the model by discarding the delayed neutron terms, because their response is negligible in the frequency range above 1 Hz. For experiments made at critical state, the reactivity can be considered null. In the end, the analytical model used for fitting prompt neutron pile noise data is a low-pass filter (Lorentzian function), with 2 or 3 parameters, depending on whether a constant B is added to account for the so-called “uncorrelated” part of the signal.

$$\frac{PSD(\omega)}{C_i C_j} = \frac{1}{F_0} \frac{D}{\beta_{eff}^2} \frac{1}{1 + \omega^2/\alpha^2} + B \quad (3)$$

where C_i and C_j are the signals of detector i and j averaged over the experiment, F_0 is the core integral fission rate, D is the Diven factor ($D = \overline{\nu(\nu - 1)}/\bar{\nu}^2$ (with ν the number of prompt neutrons per fission), β_{eff} is the effective delayed neutron fraction, ω is the angular frequency (in rad/s) and $\alpha = \beta_{eff}/\Lambda$ is the prompt decay constant.

Note that the nuclear Diven factor D was calculated with TRIPOLI-4®/JEFF311 to be 0.877. This value includes the so-called nuclear part of the Diven (0.7977) and the so-called spatial multiplication factor (1.099). See [63][64] for details on the theory and analytical expressions. An upper-bound uncertainty of 2 %, which covers the calculation’s convergence, was associated to this calculated value.

From the fitted parameters (amplitude \hat{A} and cut-off pulsation $\hat{\alpha}$) with a nonlinear least-square algorithm, the kinetic parameters are obtained as follows:

$$\beta_{eff} = \sqrt{\frac{D}{F_0 \cdot \hat{A}}} \quad (1)$$

$$\Lambda = \frac{\beta_{eff}}{\hat{\alpha}} \quad (2)$$

A short sensitivity study was conducted to optimize the fitting parameters, which lead us to choose a frequency resolution of 1 Hz and a frequency range of 150 Hz. Note that, in the end, the uncertainties and biases coming from the measurement and fit are negligible compared to the other sources of uncertainties. With these parameters, the 9 runs were fitted within Matlab (Trusted region algorithm). All results are given in appendix. The main APSD results for detector 2 are illustrated in Figure 34. The fitted amplitude was multiplied by F_0 , to account for the reactor power. The fitted values appear to be consistent with each other and no effect of the change of configuration can be seen.

The weighted average decay constant was 201.5 rad/s, with a spread equal to 1.6 %. This was consistent with the estimated standard deviation (0.5 % at 1 s). The average value of amplitude was 28846 (± 0.3 %) with a spread of 1 %. Based on these results, the average delayed neutron fraction was

779 pcm ($\pm 0.2\%$, 1 sigma statistical uncertainty). As it is usually observed, the statistical uncertainty obtained by error propagation was negligible.

4.5 Impact of the detector's distance in the reflector

In the non-symmetrical configurations, when the distance between Detector 1 and the core increased, it was observed that the APSD (rescaled to the average current) becomes flat. This can be explained by the decrease in the detector's efficiency. Because the average current drops quickly with the distance, the relative APSD increases (Figure 35, left). A significant difference with the reference measurement was observed at 10 cm and for larger distances. When the constant B was subtracted from the APSD (Figure 35, right), the curves tend to be consistent with respect to the uncertainties. So, it seems that the APSD at 20 cm is not biased but only affected by a lower signal to noise ratio. It would probably be possible to increase the measurement duration to counterbalance this effect, but this was not tested.

The fit results with Detector 1 were found consistent with the ones of Detector 2 up to around 10 cm (see appendix). When Detector 1 was pushed further from the core, the results deviate greatly (for the amplitude) or the output uncertainty becomes very large (for the decay constant). In the case of symmetrical configurations, the two detectors are in good agreement, except for the first run. Since there is a significant difference between run n°1 and run n°8 in the average current of detector 1, we chose to discard the values obtained for run n°1.

After discarding run n°1 (inconsistency), n°4 and n°5 (low efficiency), the average decay constant for Detector 1 was 202.4 rad/s ($\pm 0.5\%$), with a spread of 1.4%. The amplitude was 28714 ($\pm 0.3\%$) with a spread of 0.8%. The final delayed neutron fraction was 781 pcm ($\pm 0.2\%$, 1 sigma statistical uncertainty). This value is in excellent agreement with the one given by Detector 2, with a difference as small as 0.3%.

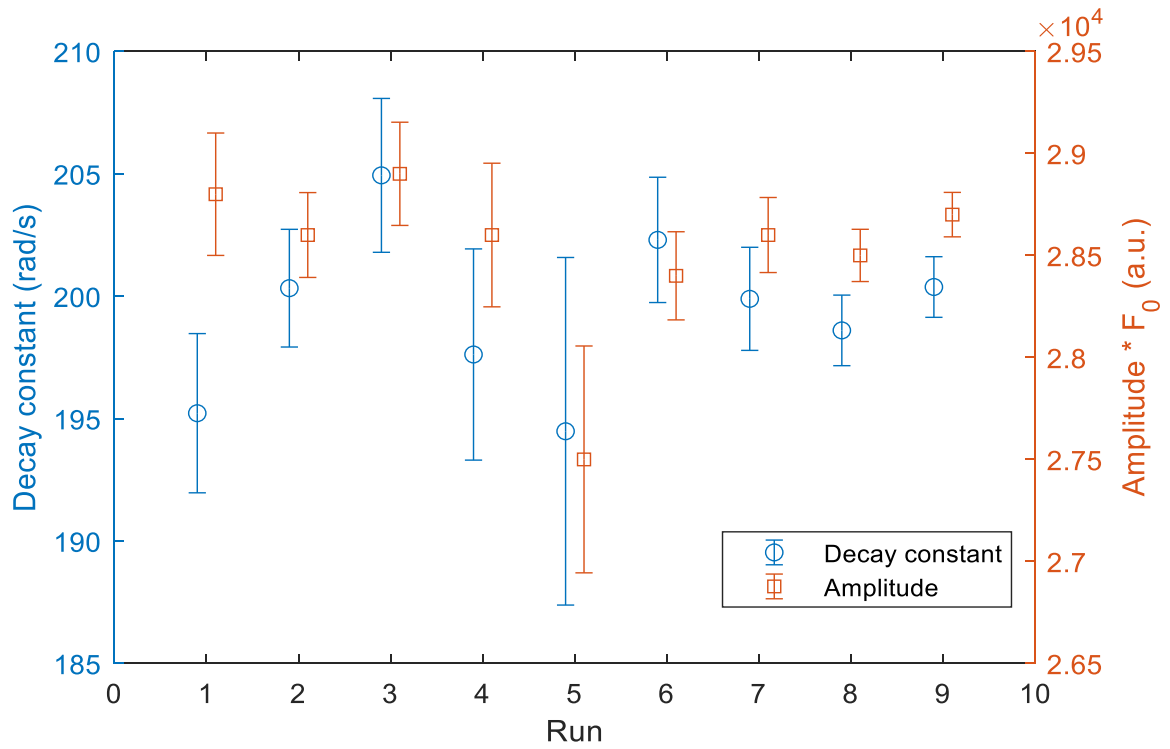


Figure 34: Fit results from APSD obtained with Detector 2: decay constant and Amplitude multiplied by the integral fission rate.

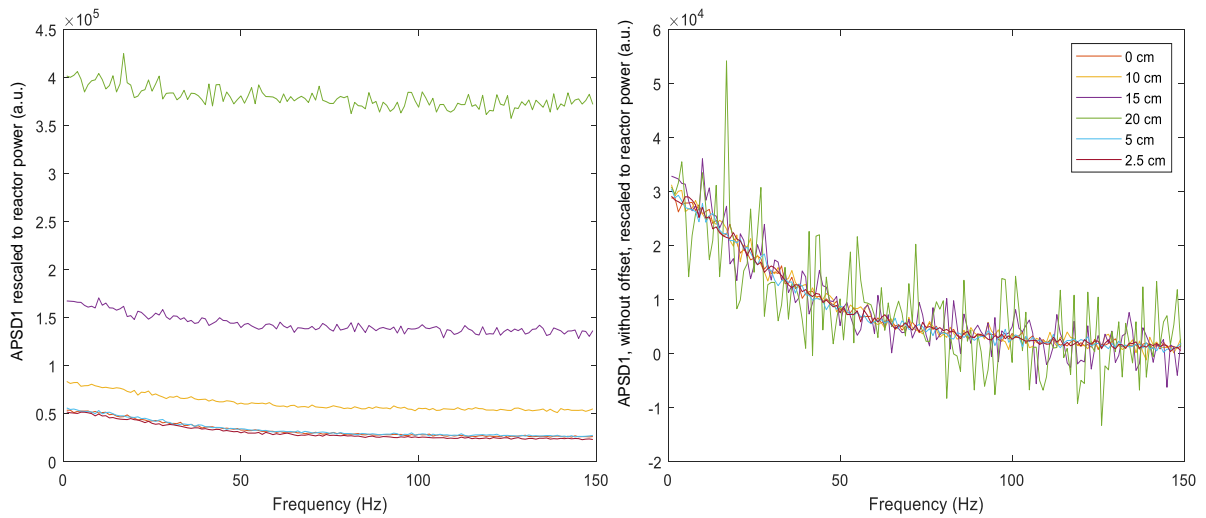


Figure 35: APSD of Detector 1 in non-symmetrical configurations, rescaled to the reactor power (left) and with constant offset subtracted (right).

4.6 Kinetic parameters of LR-0 reference core configuration

By analyzing CPSD, one is supposed to produce better results than with APSD, even compared to the average results of two APSDs. This is because the signal of non-correlated neutrons is removed when calculating the PSD, as well as spurious signals (electromagnetic noise for instance) that could affect one detector and not the other. Therefore, the signal to noise ratio is improved.

Detailed results are gathered in appendix. All the results are consistent with each other's, with respect to the uncertainty bars. As expected, uncertainties are much greater for runs n°4 and n°5, for which Detector 1 was at 15 cm and 20 cm, respectively. There is also a 4% difference on the amplitude of run n°5 as compared to the average. This motivated us to remove these two runs from the final estimation of the kinetic parameters.

The weighted averaged decay constant was found at 200.0 rad/s ($\pm 0.4\%$). The weighted amplitude was 28655 ($\pm 0.2\%$). The associated delayed neutron fraction was 782 pcm ($\pm 0.1\%$ statistical uncertainty). Satisfactorily, this value is consistent with the ones obtained from the APSDs. Note that the statistical uncertainty is very small but nevertheless in agreement with the dispersion of the results (0.3%).

The results are summarized in Table 17, along with the overall uncertainties. The uncertainty for β_{eff} and Λ include the uncertainty on the average currents (0.5%), D (2%) and FO (1.5%). In the end, the statistical uncertainty coming from the fit is negligible. The CPSD results show a slightly lower statistical uncertainty than the ones obtained from APSDs.

An excellent agreement was obtained with preliminary calculations using MCNP6.1 associated to ENDF-B-VII (see Table 18). The difference between calculated and measured decay constant was found as low as $0.1\% \pm 0.6\%$. For the delayed neutron fraction, as well as for the generation time, the relative difference was calculated at $-0.2\% \pm 1.3\%$.

4.7 Conclusions and outlooks

The first delayed neutron measurement in the reference neutron field assembled in LR-0 research reactor was conducted in 2022. A standard pile noise methodology was applied by CEA, using the double-channel current mode acquisition system SPECTRON. Measurements were done in various experimental configurations, for which the kinetic parameters do not change. The dispersion amongst the several runs was found very satisfactory, which points out the very good repeatability of the reactor operation. The estimated kinetic parameters ($\beta_{\text{eff}} = 782 \pm 10$ pcm and $\Lambda = 39.1 \pm 0.5$ μ s) were found very consistent with calculations using MCNP6.1 associated to ENDF-B.VII nuclear data library (respectively 781 pcm for the delayed neutron fraction and 39.05 μ s for the neutron generation time).

These results are very valuable complements to the characterization of LR-0 reference neutron benchmark field, that currently includes static parameters such as the criticality parameters, the spatial distribution of fission rate and, the spatial and energy distributions of the neutron field in the central cavity. The addition of kinetic parameters highly increases the nuclear data validation potential of LR-0.

Table 17: Results for Detector 1, Detector 2 and CPSD (uncertainties are given at 1σ). Run n°1, n°4 and n°5 were excluded for Detector 1. All the runs were included for Detector 2. Run n°4 and n°5 were excluded for the CPSD.

Estimator	APSD detector 1	APSD detector 2	CPSD
Amplitude	28714(89)	28880(80)	28656(46)
Decay constant (rad/s)	202.4(10)	201.5(9)	200.0(7)
Delayed neutron fraction (pcm)	782(10)	779(10)	782(10)
Generation time (μ s)	38.7(5)	38.7(5)	39.1(5)

Table 18: Kinetic parameters and microscopic reaction rates calculated with MCNP6.1 and ENDFB-VII for Run 2 (Tube B at 0 cm) and Run 5 (Tube B at 20 cm). The convergence uncertainty is given at 1 sigma.

Configuration :	Run n°2		Run n°5		Relative difference	
	Value	Uncertainty	Value	Uncertainty	Value	Uncertainty
Reactivity (pcm)	153	3	285	3	-	-
α_p	200.1	0.9	201.6	0.9	0.7 %	0.6 %
β_{eff} (pcm)	781	3	781	3	0 %	0.5 %
Λ (μ s)	39.05	0.03	38.73	0.03	-0.8 %	0.1 %
MK Capture rate (per fission)	0.21	1.9e-5	0.209	1.9e-5	-0.25 %	0.01%
PMV3 Capture rate (per fission)	0.093	2.8e-6	0.092	4.8e-6	-1.14 %	0.01 %

5 Measurements of spectrum-averaged cross sections in high-purity graphite moderation environment

In purpose of development of new benchmark reference field, experiments with graphite environment were conducted. The unique activation foil holder (Figure 36 right) consists of four pure aluminium rods with a diameter of 0.8 cm assembled in defined positions. A distance between each activation material was set to 5 cm in each rod to prevent any neutron field disruption and possible interference between the materials. Irradiation of the activation foils was performed in two independent experiments. In the first experiment, the irradiation lasted for two days, with the first part of the irradiation taking 9 hours and the second part taking 7 hours. Both experiments were operated at the same power of approximately 5 W thermal. The second experiment was performed with such selected materials, whose absorption reactions are considered as a reference for thermal neutron mapping, to verify the thermal neutron flux distribution reconstruction. The second set of activation films was irradiated for 5.5 hours at approximately 5 W thermal.

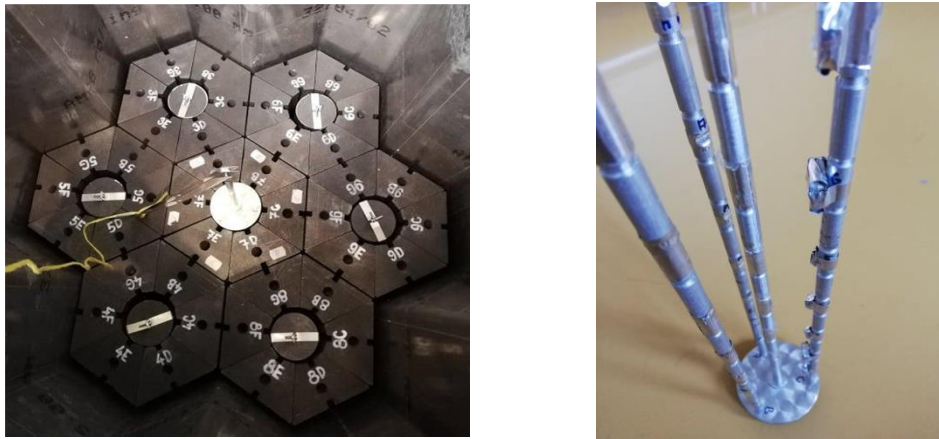


Figure 36: Photo of real arrangement in the reactor core (left side) and the activation foil holder (right side).

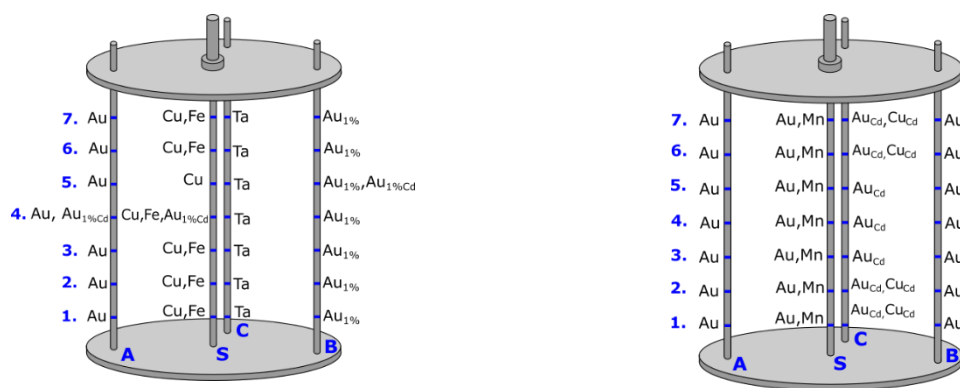


Figure 37: Schematic of the aluminium activation foil holder – the layout in the first experiment (left) and the arrangement in the second experiment (right).

Table 19: Activation foil positioning in the activation foil holder during both experiments, (Cd) stands for cadmium filter.

Axial position	Holder rod S	Holder rod A	Holder rod B	Holder rod C
1	Cu, Au, Fe, Mn	Au	1%Au, Au	Au (Cd), Cu (Cd), Ta
2	Cu, Au, Fe, Mn	Au	1%Au, Au	Au (Cd), Cu (Cd), Ta
3	Cu, Au, Fe, Mn	Au	1%Au, Au	Au (Cd), Ta
4	Cu, Au, Fe, 1%Au (Cd), Mn	Au, 1%Au (Cd)	1%Au, Au	Au (Cd), Ta
5	Cu, Au, Mn	Au	1% Au, 1%Au (Cd), Au	Au (Cd), Ta
6	Cu, Au, Fe, Mn	Au	1%Au, Au	Au (Cd), Cu (Cd), Ta
7	Cu, Au, Fe, Mn	Au	1%Au, Au	Au (Cd), Cu (Cd), Ta

Table 20: Reactions and parameters of analysed activation samples.

Measured Nuclide	Concentration	Peak Energy (keV)	HPGe Efficiency	k _{CSEF}	k _{SSEF}	k _{SSEF in Cd}
¹⁹⁷ Au(n,γ) ¹⁹⁸ Au	100%	411.8	8.22E-02	0.998	1.778	3.539
¹⁹⁷ Au(n,γ) ¹⁹⁸ Au	1%	411.8	8.22E-02	0.998	1.009	1.022
⁶³ Cu(n,γ) ⁶⁴ Cu	100%	511.0	6.71E-02	1.000	1.054	1.427
⁵⁸ Fe(n,γ) ⁵⁹ Fe	98%	1099.2	3.36E-02	0.988	1.062	1.067
⁵⁵ Mn(n,γ) ⁵⁶ Mn	100%	846.7 1810.7	2.39E-03	0.996 0.990	1.081	-
¹⁸¹ Ta(n,γ) ¹⁸² Ta	100%	1121.0 1221.4	3.56E-02	0.867 0.940	1.911	-

Neutron spectrum was calculated at specific positions of the activation holder in two computational steps. First, the raw neutron spectrum at the holder location was calculated, and then the cadmium-filtered spectrum was determined. These calculations were carried out only in MCNP6.2 code with ENDF/B-VII.1 nuclear data library and corresponding TSL (Thermal Scattering Library). Both calculations were in standard critical calculation mode with a fixed moderator level determined from critical experiments. Analyses of activation detectors with or without cadmium shaping filters were performed with 40,000 neutrons per cycle in 585,000 active cycles with 50 inactive cycles. The neutron spectrum was calculated for all 28 positions in the aluminium activation foil holder (four holder rods with seven axial irradiation positions each). The statistical uncertainty of the calculated neutron spectrum, reached in the central position S3 of the holder, is below 2% in each energy group in the energy range from 1×10^{-8} MeV to 3 MeV. In higher and lower energy regions, the statistical uncertainty in each energy group slightly rises. Obtained neutron spectrum serves as a defined neutron spectrum for reaction rate calculation in previously described activation materials.

Reaction rates of all activation foils were calculated separately with a fixed neutron spectrum source and the exact shape of the activation detector in the separate MCNP calculation. In each calculation step, 1×10^9 source neutrons were simulated with an energy spectrum corresponding to the precise position in the activation foil holder. The simulated geometry was a sphere in which the previously

calculated neutron source spectrum was simulated. The source sphere was 8 cm in diameter, and the actual specific activation foil with the corresponding shape and dimensions was placed in the centre of the sphere. The statistical uncertainty in the calculated reaction rate was between 0.3% and 0.7%, depending on the activation material. The geometry of all activation detectors was calculated with and without the activated material. Finally, the correction factors and positions of all materials were determined based on the obtained reaction rates for the specific material and cavity geometry. The self-shielding factor was defined as the share of two reaction rates: the reaction rate obtained from the calculation without activation material divided by the reaction rate obtained from the calculation with activating material. These self-shielding correction factors were later used to modify experimentally obtained data and link calculation and experiment. After that, reaction rates of all materials used for neutron mapping in the activation foil holder and comparison with the experiment were manually calculated using the scalar multiplication of the calculated neutron spectrum in a defined position and microscopic cross-section obtained from ENDF/B-VIII.0 nuclear data library. This technique determines the reaction rate per atom in each activation foil.

MCNP and Serpent were also used to calculate a wide range of the neutron spectrum. The ENDF/B-VIII.0 nuclear data library was used with a corresponding TSL matrix for this calculation. In the case of graphite, the correct TSL with 30% graphite porosity was used, which is consistent with previous research on graphite calculations and experiments performed on the LR-0 reactor [58]. The selected porosity of graphite best corresponds to the real density and structure of the graphite used for these experiments. The MCNP calculation performed 200,000 neutrons per cycle in 20,000 active and 50 inactive cycles. The uncertainty of the calculated neutron spectrum is below 0.8% in energy ranges from 1×10^{-8} MeV to 3 MeV. The same task was calculated using the Serpent code. For this calculation, 200,000 neutrons per cycle were simulated in 80,000 active cycles with 50 inactive cycles. The nuclear data library and other parameters such as temperature were the same as in the previous MCNP calculations. To reach the same uncertainty as MCNP, a higher number of simulated generations was chosen in Serpent simulations. The need for a larger number of computational cycles was probably due to the different methodology of modelling the whole system in the Serpent code compared to MCNP. The simulated detection volume was modelled at the centre of the graphite insertion height, in the axial position corresponding to the measuring point of the Stilbene detector.

The behaviour of the neutron flux and the shape of the neutron spectrum have been described in previous sections of this paper by calculating the activation detector and stilbene measurements. The pin power distribution in the selected fuel assembly was calculated to understand better how the presence of graphite affects the power distribution throughout the reactor core. The pin power distribution was calculated across the one fuel assembly in ninety axial layers for eight defined fuel pins (see Figure 39) using tally F7 calculation mode. The F7 tally, as one of the standardised tallies in MCNP, calculates fission energy deposition averaged over all cells in units of MeV/g. Obtained results show averaged fission power in defined cells which directly corresponds to the neutron flux in the observed cell. The exact axial division can be found in the results in Figure 40. This calculation was performed only in MCNP as a criticality calculation with the same nuclear data library as in the previous calculations performed and with 100,000 neutrons in 50,000 active cycles, of which 50 cycles were inactive as in the previous cases. The effect of inserted graphite is described in detail in the results section. The obtained results of fuel assembly power shaping can be compared with core power distribution in the reference neutron field [34].

The critical heights of moderator level (H_{cr}) measurements are summarised in Table 21. At this level, the reactor was critical, i.e., $k_{eff} = 1.00000$. The effect of the graphite insertion can be seen compared to cases without graphite. All the measurements were performed three times to achieve higher accuracy of the results.

Table 21: Experimental and calculated data of critical height of the moderator level H_{cr} – ENDF/B-VII.1 nuclear data library.

Modification of central module	Experimental H_{cr} [mm]	MCNP calc. k_{eff} [-]	Serpent calc. k_{eff} [-]	SCALE calc. k_{eff} [-]
With graphite insertion	391.33 ± 0.05	0.99543 ± 0.00006	0.99635 ± 0.00006	0.99569 ± 0.00005
Empty experimental module	564.23 ± 0.09	1.00140 ± 0.00005	1.00189 ± 0.00006	0.99863 ± 0.00005

The difference in moderator level between the case without graphite insertion and the case with graphite insertion is significant, indicating that graphite is a good moderator and reflector in the reactor core. One can notice that the case without graphite insertion agrees better with the experiment than the case with graphite insertion, which may be caused by disagreement in the graphite microscopic cross-section or in the TSL data library (see Table 22).

Table 22: Results from MCNP calculations from various combinations of nuclear data libraries.

Fuel and another material library	Graphite library	TSL library	k_{eff} [-] \pm 0.00006
ENDF/B-VII.1	ENDF/B-VII.1	/	0.99482
ENDF/B-VII.1	ENDF/B-VII.1	ENDF/B-VII.1	0.99543
ENDF/B-VII.1	ENDF/B-VII.1	ENDF/B-VIII.0 crystalline modification	0.99770
ENDF/B-VII.1	ENDF/B-VII.1	ENDF/B-VIII.0 10% porosity	0.99787
ENDF/B-VII.1	ENDF/B-VII.1	ENDF/B-VIII.0 30% porosity	0.99785
ENDF/B-VII.1	JEFF 3.3.	JEFF 3.3	0.99539
ENDF/B-VII.1	ENDF/B-VIII.0	/	0.99487
ENDF/B-VII.1	ENDF/B-VIII.0	ENDF/B-VII.1	0.99542
ENDF/B-VII.1	ENDF/B-VIII.0	ENDF/B-VIII.0 crystalline modification	0.99778
ENDF/B-VII.1	ENDF/B-VIII.0	ENDF/B-VIII.0 10% porosity	0.99782
ENDF/B-VII.1	ENDF/B-VIII.0	ENDF/B-VIII.0 30% porosity	0.99786
ENDF/B-VII.1	ENDF/B-VIII.0	JEFF 3.3	0.99538
ENDF/B-VIII.0	ENDF/B-VIII.0	ENDF/B-VIII.0 30% porosity	0.99383

Various combinations of nuclear data libraries and different TSL, only for graphite, can be found in Table 22. For all cases, the construction and other core materials were modelled in the same library ENDF/B-VII.1. only the graphite cross-section and TSL matrix were changed. Table 22 shows that when TSL in ENDF/B-VII.1 is used, the difference is only approximately 60 pcm compared to the case without

the TSL matrix of graphite. On the other hand, a very strong influence of all TSL modifications from the ENDF/B-VIII.0 nuclear data library is observed, with more than 240 pcm difference. Compared to this phenomenon, the JEFF 3.3. TSL matrix for graphite achieved a very similar result to the ENDF/B-VII.1, indicating that the evaluation of ENDF/VIII.0 is not entirely correct due to high overestimations of achieved results in comparison with other cases.

5.1 Reaction rate measurement

Based on the previously mentioned methodology, the activity of the activation detectors was measured on the HPGe detector and then calculated based on the methodology described in chapter 1.2. Estimated reaction rates based on measurement were normalised using a scaling factor. The scaling factor is a calculated constant representing the neutron emission in the reactor core. For calculating the scaling factor from the experiments, the average value based on Ta and ¹⁹⁹Au activation foils were used (positions 2, 3, and 4 in the activation foil holder). The scaling factor is calculated from the experimentally obtained reaction rate multiplied by the self-shielding correction factor and divided by the calculated reaction rate from the MCNP code calculation. The scaling factor for both experiments has been determined to be 4.245×10^{11} with 0.86 % statistical uncertainty. The average neutron emission per one fission obtained from MCNP calculation was 2.447 neutrons, with fission energy released of 180.9034 MeV. From these values, the irradiation power during the experiments mentioned above was calculated to be approximately 5 W. Table 23 shows experimentally determined reaction rates of the activation foils in the defined position on the activation holder. The statistical uncertainty of measurement has been quantified with a combination of measured geometry uncertainty and uncertainty of HPGe detector below 0.79 % for all observed activation detectors.

On the other hand, position 6 may be affected by the moderator-air interface, and position 7 is located above the moderator level. Position 7 shows the highest inconsistency of all the activation holder positions examined. As the difference between the moderator level and the position of the activation foil increases, the underestimation rises, corresponding to the neutron flux distribution previously observed [36].

Table 23: Experimentally determined reaction rates of the activation foil per one atom in the exact position on the special aluminum activation foil holder. The unit is (1/s)

Material	Au	Cu	Fe	Mn	Au ^{100%}	Au ^{100%}	Au ^{1%}	Ta	Au ^{100%} (Cd)	Cu (Cd)	Au ^{1%} (Cd)	Au ^{1%} (Cd)	Au ^{1%} (Cd)
Position	Rod S	Rod S	Rod S	Rod S	Rod A	Rod B	Rod B	Rod C	Rod C	Rod C	Rod S	Rod A	Rod B
1	7.650E-27	1.872E-28	5.406E-29	5.311E-28	7.844E-27	7.597E-27	7.976E-27	2.703E-27	3.718E-27	1.573E-29	-	-	-
2	8.441E-27	2.040E-28	5.990E-29	5.733E-28	8.831E-27	8.437E-27	8.990E-27	2.976E-27	4.500E-27	1.886E-29	-	-	-
3	9.171E-27	2.047E-28	5.996E-29	6.122E-28	9.431E-27	9.169E-27	9.510E-27	3.196E-27	5.016E-27	-	-	-	-
4	9.489E-27	2.083E-28	5.866E-29	6.290E-28	9.554E-27	9.493E-27	9.715E-27	3.235E-27	5.856E-27	-	5.623E-27	5.791E-27	-
5	8.990E-27	2.005E-28	-	6.077E-28	9.271E-27	9.253E-27	9.793E-27	3.261E-27	5.954E-27	-	-	-	5.696E-27
6	8.896E-27	1.912E-28	5.167E-29	5.511E-28	8.912E-27	8.935E-27	8.904E-27	2.962E-27	5.113E-27	2.008E-29	-	-	-
7	7.877E-27	1.698E-28	4.664E-29	4.830E-28	8.061E-27	7.736E-27	8.242E-27	2.353E-27	4.598E-27	1.882E-29	-	-	-

In order to compare experimental data and MCNP calculations of reaction rates, the C/E-1 (Calculation/Experiment 1) comparison was realised (see Table 24). An excellent agreement is shown between measurement and calculation in positions 3, 4, and 5, which is caused by their position in the centre of the activation holder (Figure 37) in the centre of the graphite insertion in the axial direction.

In contrast, positions 1, 2, and 6, 7 are underestimated for almost all detectors. This phenomenon may be caused by their axial position on the holder, which is, in the case of positions 1 and 2, at the bottom part of the graphite insertion module near the lower construction parts of the reactor core. The module has stainless steel weight and a relatively large amount of water, which seems to affect the shape of the neutron spectrum. At the same time, other boundary phenomena such as the end of the fuel column in this area may play a non-negligible role in neutron spectrum shaping.

Table 24: Calculated C/E-1 for all reaction rates in all positions on the holder

Material	Au	Cu	Fe	Mn	Au	Au	Au 1%	Ta	Au (Cd)	Cu (Cd)	Au 1% (Cd)	Au 1% (Cd)	Au 1% (Cd)
Position	Rod S	Rod S	Rod S	Rod S	Rod A	Rod B	Rod B	Rod C	Rod C	Rod C	Rod S	Rod A	Rod B
1	-0.01%	-9.64%	-8.88%	-5.22%	-2.77%	0.98%	-3.81%	-5.71%	12.55%	-11.61%	-	-	-
2	5.49%	-4.88%	-5.87%	-0.05%	0.51%	6.55%	-0.01%	1.18%	10.05%	-11.34%	-	-	-
3	5.24%	0.10%	-0.86%	-1.01%	3.10%	4.25%	0.52%	-0.26%	4.07%	-	-	-	-
4	1.31%	-2.68%	0.57%	-4.41%	0.73%	0.67%	-1.63%	0.25%	-7.75%	-	-2.46%	-4.95%	-
5	0.85%	-6.07%	-	-7.90%	-2.24%	-0.66%	-6.14%	-6.31%	-12.62%	-	-	-	-10.55%
6	-10.58%	-13.98%	-7.45%	-11.55%	-10.07%	-26.56%	-26.30%	-8.17%	-10.88%	-23.20%	-	-	-
7	-17.03%	-21.08%	-16.61%	-18.04%	-18.59%	-14.01%	-19.29%	-3.90%	-15.74%	-31.94%	-	-	-

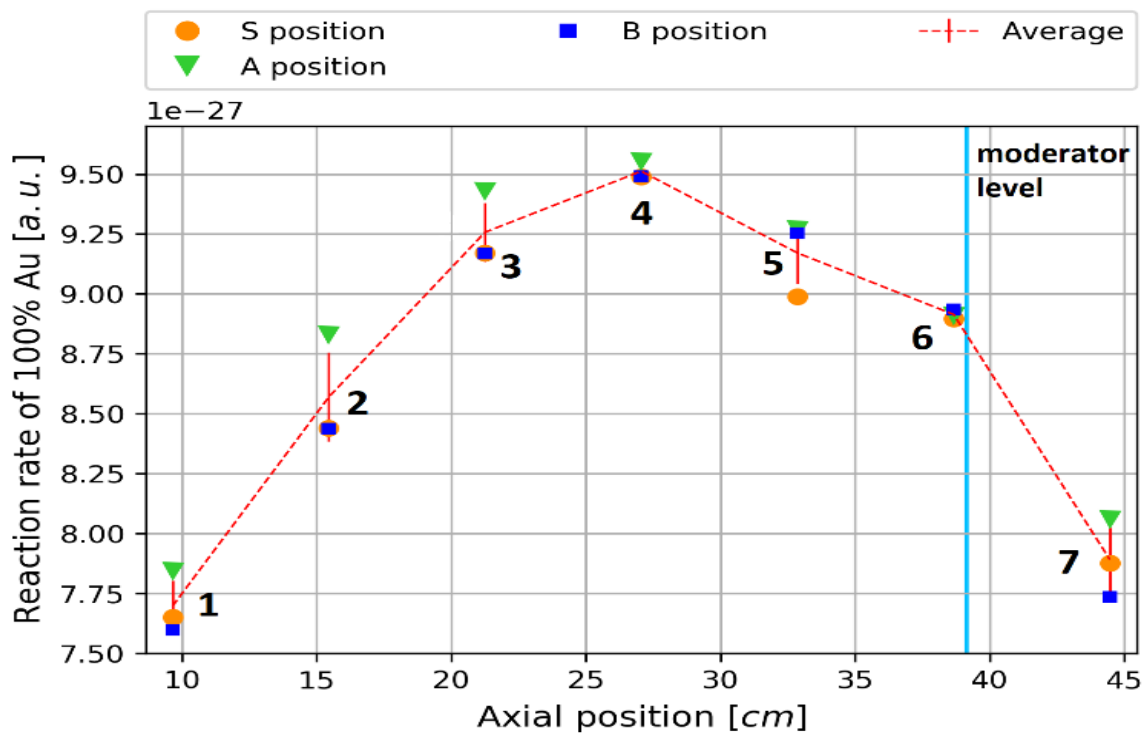


Figure 38. Thermal neutron flux - radial profile in different axial positions of holder

On the other hand, position 6 may be affected by the moderator-air interface, and position 7 is located above the moderator level. Position 7 shows the highest inconsistency of all the activation holder positions examined. As the difference between the moderator level and the position of the activation foil increases, the underestimation rises, corresponding to the neutron flux distribution previously observed [36].

The neutron flux profile in graphite block is illustrated by a plot of the Au reaction rates along the height of the special activation holder in Figure 38. Relatively high uniformity of the neutron field is demonstrated in the radial direction in all irradiation positions, especially around the centre of the activation holder in positions 3, 4, and 5, indicating the high homogeneity of the neutron field in the radial direction.

5.2 The effect of graphite on the neutron flux distribution

Experimental data and calculations have also demonstrated the effect of graphite on the neutron flux distribution in the axial direction of the reactor core. Figure 40 shows the axial profile of the neutron flux over the height of the reactor core. For illustration, the fission reaction rate in eight selected pins in the radial direction of the chosen fuel assembly was calculated, see Figure 39. Pin 1 is the closest to the experimental graphite module, and pin 8 stands on the other side of the fuel assembly at the furthest position. Additionally, the reaction rate distribution was calculated in the centre of the graphite insertion and compared to the experimental data obtained from the average reaction rate of Au activation foils.

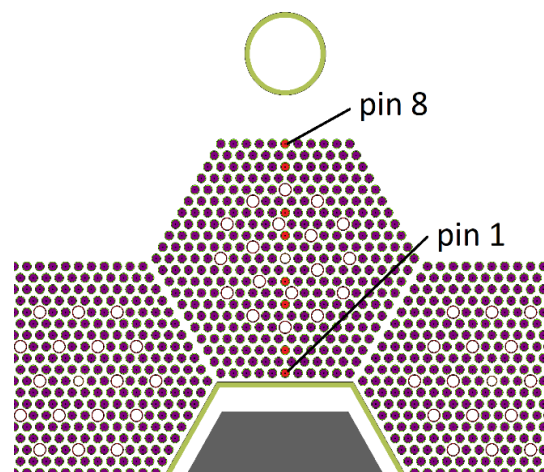


Figure 39. Position of eight pins across fuel assembly for power distribution mapping

The effect of the graphite presence in the centre of the reactor core can be seen in Figure 40. The influence is directly apparent in the neutron flux distribution of the fuel rods. The contribution of the neutron flux above the moderator level in the closest pin to graphite (pin 1) is higher than in pin 8 (pin 8), which is the farthest away from the graphite module. This effect, observed above the moderator level ($H_{cr} = 39.13$ cm), is attributed to the graphite reflector because, below the moderator level, this effect is almost negligible. With increasing distance above the moderator level, the neutron flux decreases. Over the graphite blocks, however, the neutron flux decreases for both fuel pins with the same trend. The end of the graphite blocks corresponds to the height of 64.4 cm in Figure 40.

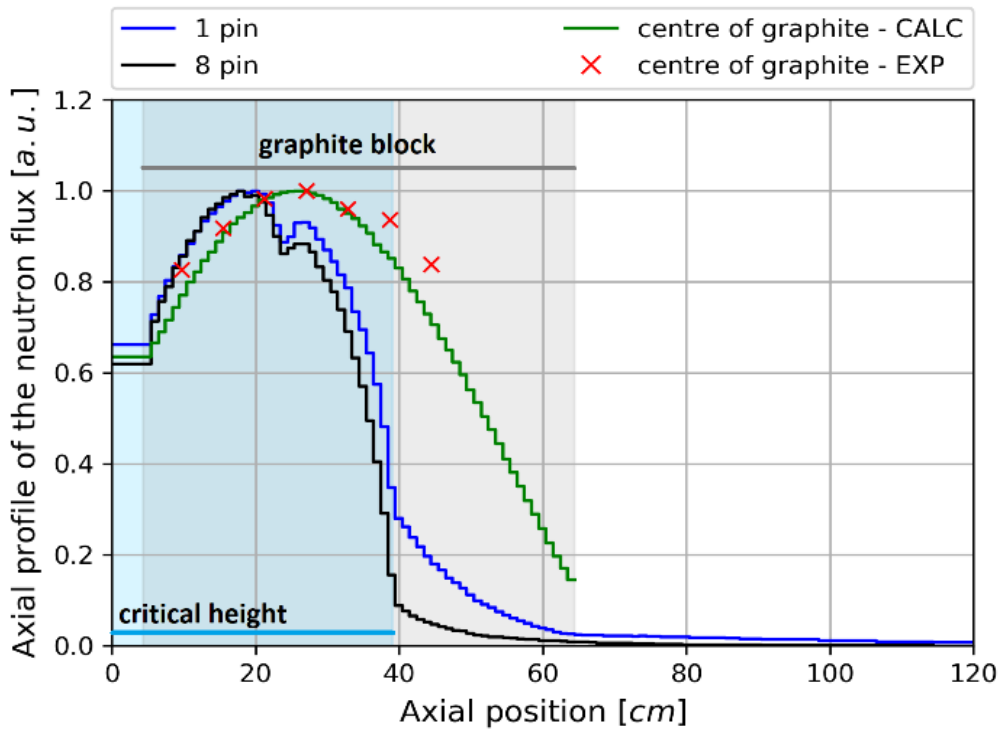


Figure 40. Neutron flux distribution in the axial profile of the fuel and graphite insertion (selection in Figure 39)

One can notice a considerable influence of the spacer grids located roughly in the centre of the reactor core from the axial course of the neutron flux in the fuel pins. Spacer grids strongly distort the shape of the neutron flux distribution in the fuel pins, and therefore the predicted maximum is distorted and shifted by this effect. Compared to neutron flux calculation in the graphite, an upward shift of the neutron flux maximum compared to the neutron flux distribution in the fuel can be observed, which is probably caused by the geometry of the graphite blocks and their position relative to the fuel column. In the centre of the graphite, the difference in the flux distribution between calculation results and measurement is minimal. As in previously discussed measurement result, Figure 40 confirms good agreement at positions 3, 4, and 5 on the activation holder. Disagreement in positions 6 and 7 can be caused by neutron field non-uniformity and the angular distribution of the neutron field. There is almost no source of neutrons in the radial direction from graphite blocks. Positions 1 and 2 can be affected by the edge effects of steel and water located under the graphite insertion. Below the moderator level, the neutron flux profile in graphite is very close to a parabola. Above the moderator level, a linear decrease can be observed, which is consistent with previous assumptions.

5.3 Fast neutron spectrum evaluation

The further stage was to evaluate the neutron spectrum in the fast energy region. Since the activation foils were selected with a focus on reactions in thermal and epithermal energy regions, a measurement with a stilbene scintillator was used to determine the fast neutron spectrum. The assumption determined by the calculation is a very well thermalised neutron spectrum in the proposed reactor core with graphite insertion, as shown in Figure 41. The total neutron spectrum was calculated using

MCNP and Serpent in the centre of the graphite insertion and then compared with the neutron spectrum of the reference core without graphite determined in MCNP. Serpent and MCNP calculations are in excellent agreement, and obtained results were normalised to 1 by integrating over the entire neutron spectrum. In contrast to the reference LR-0 core, significant thermalisation occurs in the proposed reactor core with a thermal neutron ratio of almost 25% and a fast neutron ratio of less than 4% above 1 MeV. Moreover, the epithermal region is flat and nearly constant compared to the LR-0 reference core without the graphite central module, which can be further used to evaluate microscopic cross-sections in this energy region.

The calculated fast neutron spectrum of the reactor core was experimentally verified by measurement using the stilbene detector in the centre of the graphite insertion. For this purpose, calculated and measured data are normalised to 1 and integrated over the spectrum from 4 MeV to 10 MeV. The measurement was accomplished in the range from 1 MeV to 10 MeV, and Figure 42 reveals the measurement results and compares the results with calculations. Calculated results obtained from MCNP and Serpent calculations were modified by Gaussian broadening function using experimentally determined parameters for the stilbene detector. This method allows the comparison of experimental and calculated results. In the resulting calculated spectrum of fast neutrons, there are several sharp resonances due to resonances in the microscopic cross-section of graphite, namely between 2 MeV and 3 MeV. Considering the shape of the resonances, which are very sharp and narrow, they cannot be observed by the stilbene detector in detail, as this does not allow its resolution. The effect of these resonances can still be seen in Figure 43. It should be noted that the spectrum from Serpent is underestimated across the entire spectrum. On the other hand, Figure 41 suggests that Serpent is slightly overestimated in thermal energy.

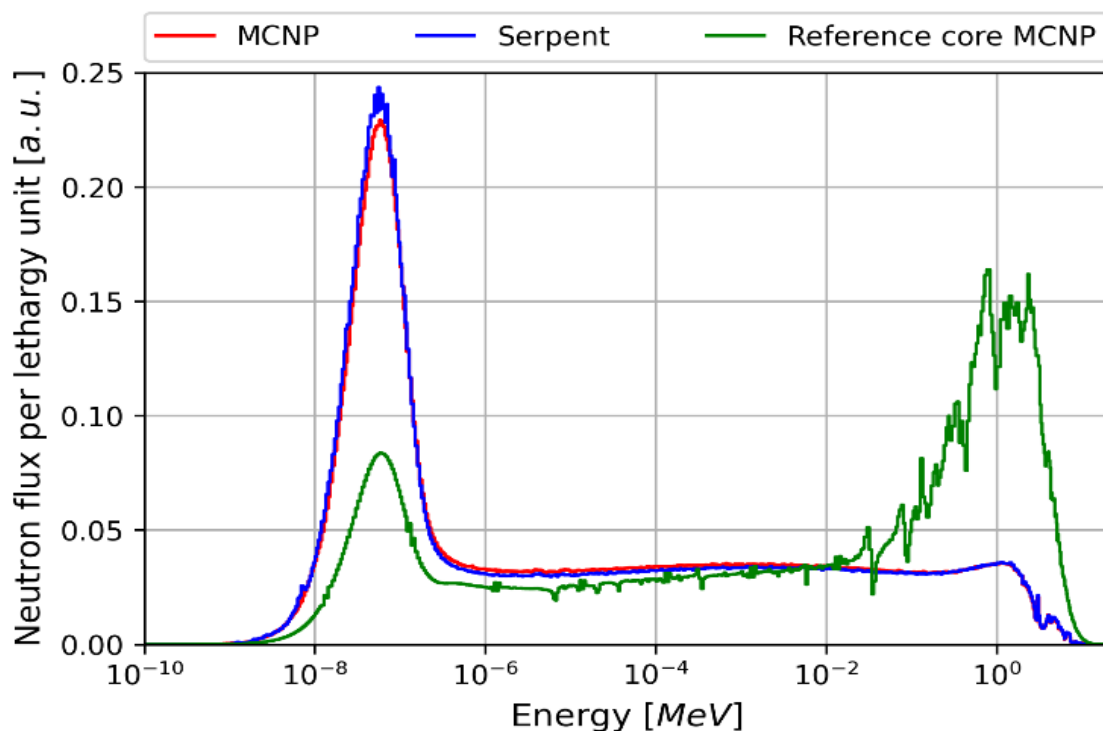


Figure 41: Calculated neutron spectrum of the proposed reactor core with the graphite insertion compared with the reference LR-0 reactor core.

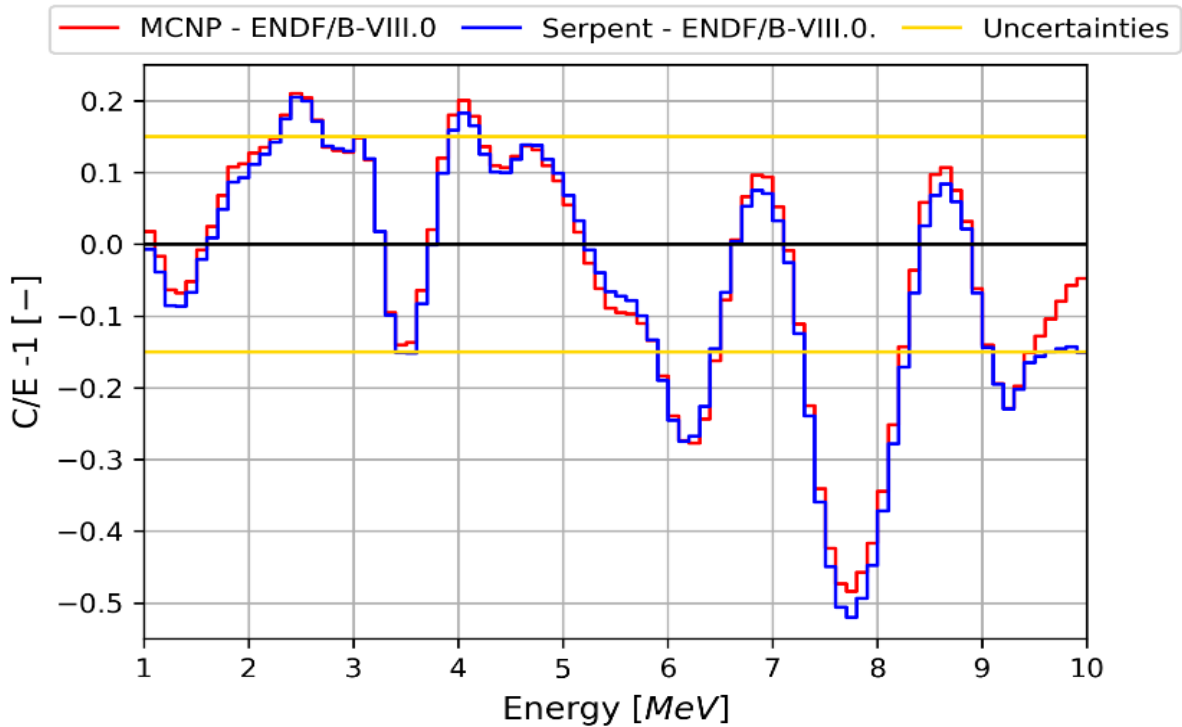


Figure 42: The C/E-1 comparison of the fast neutron spectrum calculated by MCNP and Serpent and experimental data.

The calculated and measured results match very well from 1 MeV to 5.8 MeV. The deviation between the calculated and measured neutron spectrum increases from 6 MeV to 7 MeV, and around 8.5 MeV, the deviation is significant. Then, up to 10 MeV, the results are again in good agreement. To better understand the behaviour of the measured and calculated spectrum, Figure 42 compares the experimental data and calculation results in C/E-1. One can notice that, with a few exceptions, the region from 1 MeV to 5.8 MeV is within the +/- 15% uncertainty, and the discrepancy rises to -27% above the 5.8 MeV in specific troublesome energies. The most significant disagreement between the calculated and experimentally determined spectra may be observed around 7.8 MeV, where MCNP and Serpent calculations are underestimated by almost 50%, whereas the same tendency was observed in the previous experiments with graphite block leakage [66]. That massive discrepancy may be caused by certain evaluation inaccuracy in graphite microscopic cross-sections, mainly around 8 MeV. The criticality calculations of the reactor core with central graphite insertion, consistently underestimated throughout all reactor core calculations (Table 21, Table 22), may also indicate this phenomenon. Based on these assumptions, a sensitivity analysis of microscopic cross-sections was created to illuminate this issue using TSUNAMI-3D.

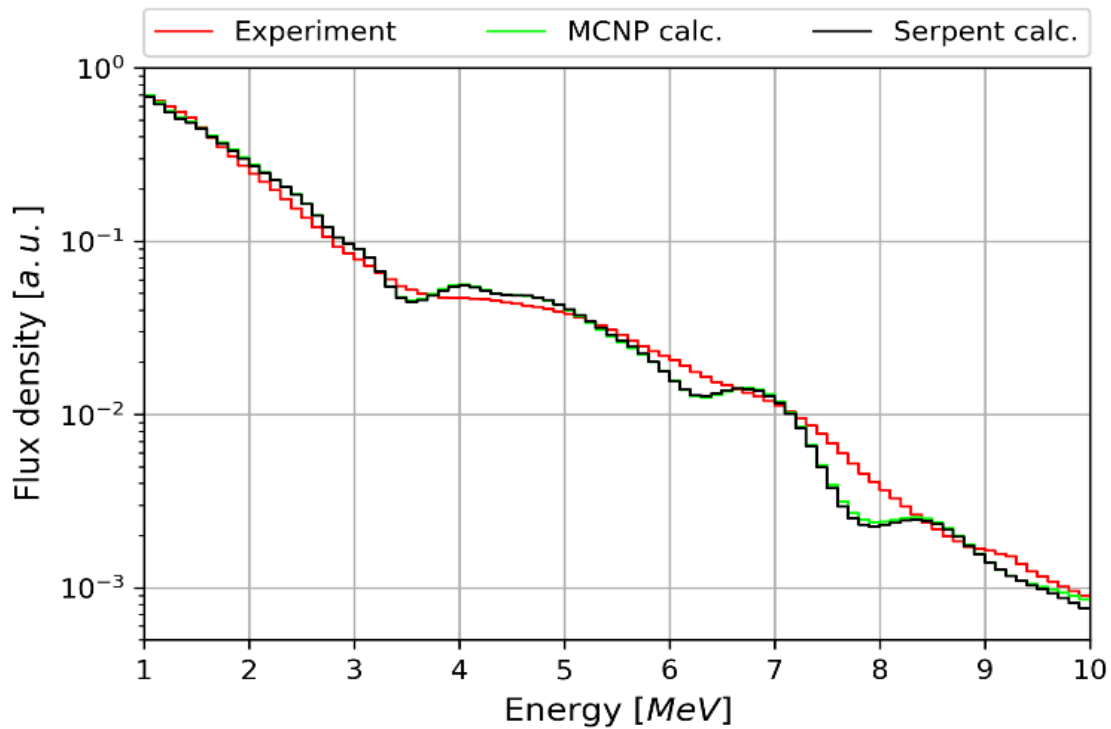


Figure 43: Comparison of the experimentally measured fast neutron spectrum and spectrum calculated by MCNP and Serpent code compared with the reference LR-0 reactor core.

The results showed that graphite has one-tenth the sensitivity compared to the moderator, which is the most sensitive material in the core. It also showed that the fuel sensitivity is about 40% of the moderator sensitivity. The sensitivity shows how the k_{eff} changes if the macroscopic cross-section of a given reaction (or material) is changed by 1%. The ten most significant reactions are tabulated in Table 25. It is not surprising that these are the reactions in the fuel and moderator.

Analysis of graphite reactions, tabulated in Table 26, has shown that elastic scattering is the dominant reaction. This reaction is the tenth most crucial reaction in the core. The second most important reaction in graphite, radiative capture, has a sensitivity lower than 5 % of elastic scattering sensitivity. Sensitivity profiles of both reactions and inelastic scattering are depicted in Figure 44.

Table 25: The most sensitive reactions in the reactor core determined by SCALE

Material	Nuclide	Reaction	Sensitivity [-]	Uncertainty
Fuel	^{235}U	nubar	9.49E-1	0.00 %
Moderator	^1H	(n,n)	3.46E-1	0.14 %
Fuel	^{235}U	(n,f)	3.22E-1	0.02 %
Fuel	^{238}U	(n, γ)	-1.68E-1	0.01 %
Fuel	^{235}U	(n, γ)	-1.24E-1	0.01 %
Moderator	^1H	(n, γ)	-9.42E-2	0.02 %
Fuel	^{238}U	nubar	5.06E-2	0.04 %
Moderator	^{16}O	(n,n)	3.93E-2	0.36 %
Fuel	^{238}U	(n,f)	3.42E-2	0.06 %
Graphite	Graphite	(n,n)	3.12E-2	0.72 %

Table 26: Calculated sensitivities in the graphite

Reaction	Sensitivity (-)	Uncertainty
(n,n)	3.12E-2	0.72%
(n,total)	3.00E-2	0.75%
(n, γ)	-1.40E-3	0.07%
(n,n')	2.38E-4	1.26%
(n, α)	-6.66E-5	0.56%

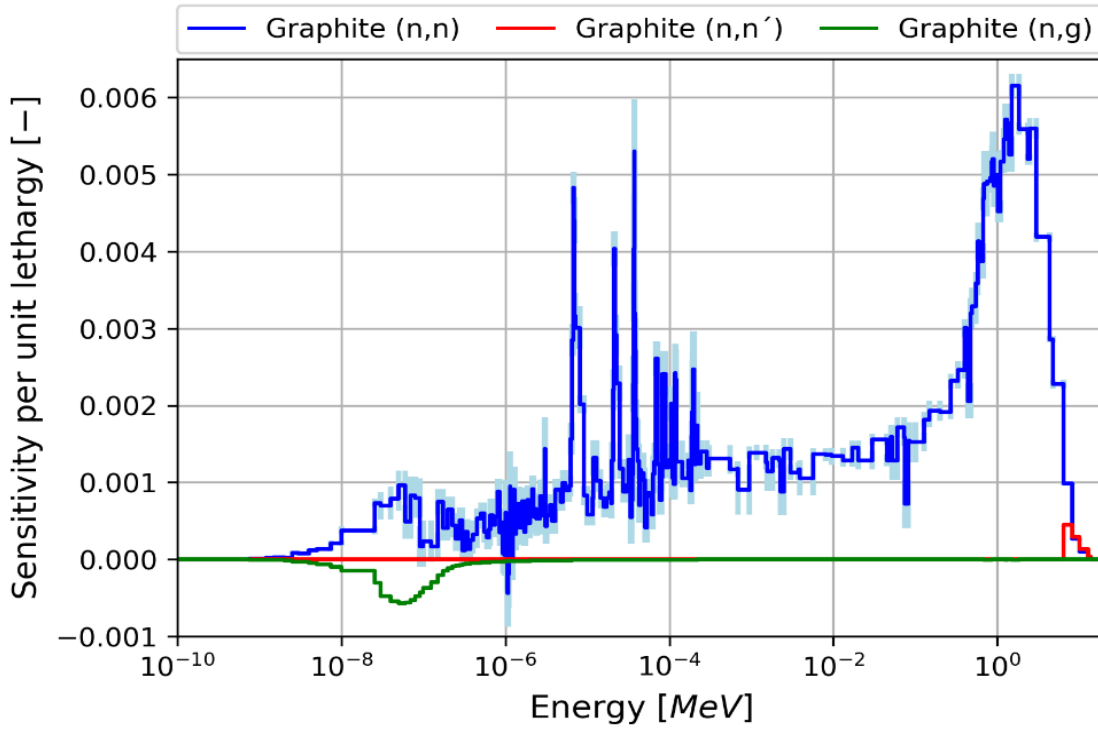


Figure 44: Sensitivity per unit lethargy for the most important graphite reactions

Table 27: Experimental SACS in large graphite environment

Experiment	Au (b)	Cu (b)	Fe (b)	Mn (b)	Au (b)	Au (b)	Au1%(b)	Ta (b)	NaF (b)
Position	ROD S	ROD S	ROD S	ROD	ROD A	ROD	ROD B	ROD C	ROD
1	85.0252	2.0809	0.6008	5.9027	87.1854	84.4367	88.6464	30.0399	-
2	81.7597	1.9757	0.5802	5.5527	85.5421	81.7180	87.0762	28.8250	-
3	83.6668	1.8675	0.5470	5.5848	86.0361	83.6481	86.7580	29.1553	0.2179
4	87.0017	1.9097	0.5378	5.7667	87.5944	87.0315	89.0666	29.6577	-
5	88.0621	1.9638	-	5.9525	90.8136	90.6380	95.9348	31.9483	-
6	98.7951	2.1233	0.5739	6.1210	98.9783	99.2319	98.8822	32.8946	0.2312
7	105.7870	2.2803	0.6264	6.4869	108.2584	103.9009	110.6953	31.5970	-

Table 28: Experimental SACS for reactions from foils in Cd cladding and in large graphite environment

Experiment	Fe _{Cd} (b)	NaF _{Cd} (b)	NaF _{Cd} (b)	Au _{Cd} (b)	Cu _{Cd} (b)	Au1% _{Cd} (b)	Au1% _{Cd} (b)	Au1% _{Cd} (b)
Position	ROD S	ROD	ROD B	ROD C	ROD C	ROD	ROD A	ROD B
1	-	-	-	41.3233	0.1748	-	-	-
2	-	-	-	43.5844	0.1827	-	-	-
3	-	-	-	45.7569	-	-	-	-
4	0.0477	0.0114	-	53.6881	-	51.5554	53.0952	-
5	0.0504	-	0.0120	58.3263	-	-	-	55.7956
6	-	-	-	56.7826	0.2230	-	-	-
7	-	-	-	61.7534	0.2527	-	-	-

Table 29: Calculated SACS in graphite environment

Calculation	Au (b)	Cu (b)	Fe (b)	Mn (b)	Au (b)	Au (b)	Au1%(b)	Ta (b)	NaF (b)
Position	ROD S	ROD S	ROD S	ROD	ROD A	ROD	ROD B	ROD C	ROD
1	85.0147	1.8802	0.5474	5.5945	84.7747	85.2678	85.2678	28.3252	-
2	86.2471	1.8793	0.5461	5.5500	85.9808	87.0667	87.0667	29.1646	-
3	88.0524	1.8694	0.5423	5.5284	88.7044	87.2049	87.2049	29.0781	0.2150
4	88.1426	1.8585	0.5408	5.5122	88.2373	87.6188	87.6188	29.7326	-
5	88.8100	1.8445	-	5.4822	88.7801	90.0437	90.0437	29.9316	-
6	88.3411	1.8264	0.5311	5.4142	89.0111	72.8799	72.8799	30.2078	0.1703
7	87.7753	1.7996	0.5224	5.3166	88.1335	89.3406	89.3406	30.3658	-

Table 30: Calculated SACS in graphite environment and Cd cladding

Calculation	Fe _{Cd} (b)	NaF _{Cd} (b)	NaF _{Cd} (b)	Au _{Cd} (b)	Cu _{Cd} (b)	Au1% _{Cd} (b)	Au1% _{Cd} (b)	Au1% _{Cd} (b)
Position	ROD S	ROD	ROD B	ROD C	ROD C	ROD	ROD A	ROD B
1	-	-	-	46.5076	0.1545	-	-	-
2	-	-	-	47.9666	0.1619	-	-	-
3	-	-	-	47.6201	-	-	-	-
4	0.0410	0.0099	-	49.5278	-	50.2869	46.7091	-
5	0.0420	-	0.0100	50.9636	-	-	-	49.9065
6	-	-	-	50.6052	0.1713	-	-	-
7	-	-	-	52.0348	0.1720	-	-	-

5.4 Experiment with single graphite insertion

In addition to large graphite insertion, also the neutron field was studied in single graphite insertion (Figure 45). Namely, the experimental dry module is filled with graphite block, which consists of six smaller trapezoidal graphite parts with a central void cavity. These six blocks filled the dry channel, except the central cylindrical cavity with 8 cm diameter. The height of the block is 60 cm, hexagonal key (flat-to-flat) dimension is 21.65 cm. The neutron detector, like stilbene and activation foil holder, was placed in the central cavity. The graphite block used in this experiment has a density of 1.72 ± 0.02

g/cm^3 and a concentration of impurities below 0.2 ppm of boron equivalent and thus meets the nuclear graphite limits.

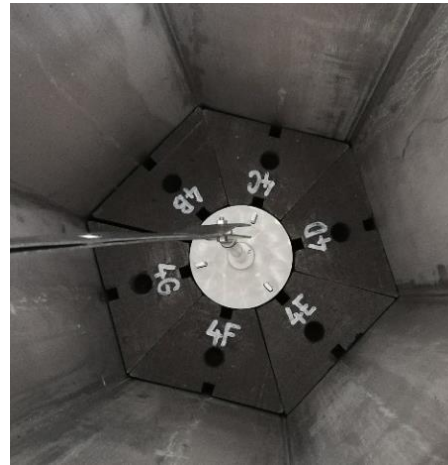
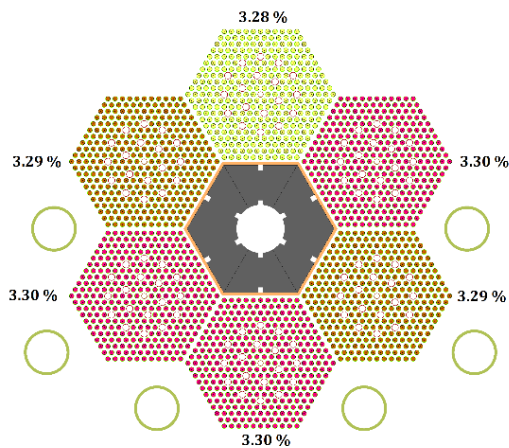


Figure 45. Schematic diagram of the LR-0 core with single graphite (left), photo of real graphite insertion with activation foil holder (right).

5.5 Mapping of the neutron flux distribution in the graphite prism

For precise axial monitoring of the thermal, epithermal, and fast neutron flux, the set of activation detectors, 1% Au, Ta, and Ni activation foil, was chosen. The schematical arrangement and axial position of the activation foil fixed to the holder can be seen in Figure 46. The reaction of Au activation foil $^{197}\text{Au}(n,\gamma)^{198}\text{Au}$ serves for thermal neutron mapping, Ta for epithermal neutron mapping (reaction $^{181}\text{Ta}(n,\gamma)^{182}\text{Ta}$) and the Ni activation detector serves for fast neutron flux monitoring (reaction $^{58}\text{Ni}(n,p)^{58}\text{Co}$).

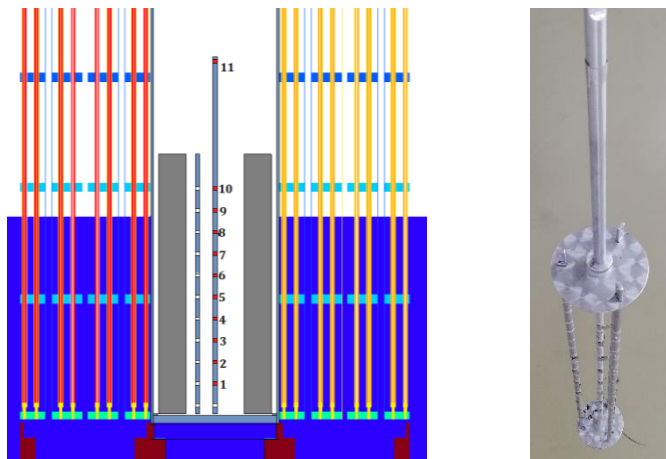


Figure 46. Side view on activation foil holder and number of positions, schematic view, and photo.

The activation Au and Ta detectors have a square shape with a 3 mm side length, and the thickness of the foil was 0.1 mm. Due to the much lower fast neutron flux, the Ni foils were larger and square in shape with a side length of 8 mm and thickness of 1 mm. The activation foil holder consists of four pure aluminium rods in a fixed geometry. Each rod is made of pure aluminium with a diameter of 0.8 mm, and the holder's height is 60 cm. In the upper and lower parts, there is a special centering ring plate to ensure the vertical position of the holder. Activation detectors were placed in the central rod

of the holder; in other rods the monitors for thermal power mapping were used. These monitors were not evaluated as part of this work.

All activation detectors were mounted in fixed known geometry at a 5 cm axial distance between each other to ensure a sufficiently low neutron field distortion effect. Their positions are illustrated in Figure 46. In the axial direction, ten positions were evaluated; the last activation foil, position 11, in the case of Ta foil, was over the graphite insertion to assess the neutron flux far from the core above the moderator level (431.16 mm) and the graphite prism. Position 11 was 21.4 cm above the top of the graphite prism, which means 29.4 cm above the water moderator level. Irradiation was carried out in single-step irradiation for 11 hours at a thermal power of 7.5 W to reach sufficient activity of Ni detectors.

5.6 MCNP calculation and reaction rate determination

Critical analyses were performed using MCNP 6.2 Monte Carlo code with ENDF/B-VIII.0 nuclear data library and corresponding TSL (Thermal Scattering Library) for graphite and water. For the graphite, the 30% porosity type TSL was chosen based on previous research. The model of the whole core was developed without any simplifications in precise geometry and material composition. In the critical calculation mode, the 100,000 neutrons per cycle in 500,000 cycles were simulated, and the first 50 inactive generations were chosen for proper source distribution. This critical calculation calculated the neutron spectrum for all axial positions in the activation foil holder. The neutron spectrum statistical uncertainty in a central position, in the center of the axial height of the core, marked as position P4, is below 1 % in each energy group in the energy range from 6×10^{-9} MeV to 5.3 MeV. In higher and lower energies, the statistical uncertainty slightly rises. For instance, on the 10 MeV, there is an uncertainty of 5.71%. The obtained neutron spectrum serves as a defined neutron spectrum for reaction rate calculation in activation materials described in the sections above.

The reaction rates for self-shielding correction factors were calculated in separate simplified MCNP simulations in fixed source calculation. The simulated geometry of the neutron source was a sphere shape with an 8 cm diameter, where the neutron source was placed. The activation material was placed in the sphere's center with precise dimensions and shape. As a neutron source spectrum, the results from the critical calculation were used for each axial position detailed spectrum and type of activation detector. In each calculation step, the 1×10^9 source neutrons were simulated. The statistical uncertainty in the calculated reaction rate was between 0.2% and 0.6%, depending on the activation material.

The reaction rate was evaluated for cases with and without the material in the detector volume. After that, the correction factor of all materials was determined based on the obtained reaction rates for the specific material and cavity geometry. The self-shielding factor was defined as the reaction rate obtained from the calculation without activation material divided by the reaction rate obtained from the calculation with activating material. These self-shielding correction factors were later used to modify experimentally obtained data.

Finally, reaction rates of all materials used for neutron mapping in the activation foil holder and comparison with the experiment were manually calculated using the scalar multiplication of the calculated neutron spectrum in a defined position and microscopic cross-section obtained from

ENDF/BVIII.0 nuclear data library. This technique determines the reaction rate per atom in each activation foil.

First, the critical height of the moderator level (H_{cr}) was measured three times. The experimentally estimated moderator level was the most crucial parameter for the critical calculation. In this case, the experimental moderator level was 431.16 ± 0.02 mm, corresponding to the MCNP calculation result $k_{ef} = 1.00031 \pm 0.00001$. Regarding this result, there is excellent agreement between the experiment and calculation in case of criticality. It also shows that the developed model is in excellent agreement with the real case.

Reaction rate determination is described in the upper section. The activation foils were measured after the irradiation on the HPGe detector, and then subsequently using Equation (1) and (2), the reaction rate has been determined. All reaction rates, based on measurement and calculation, were normalized to one atom in activation detector volume. Estimated reaction rates based on measurement were normalized using a scaling factor, where this factor represents the neutron emission in the reactor core. The scaling factor was determined based on all activation detector types (Ni, Ta and 1% Au) by averaging the values from position 3-7. The scaling factor is calculated from the experimentally obtained reaction rate multiplied by the self-shielding correction factor and divided by the computed reaction rate from the MCNP code calculation. The scaling factor for this irradiation was determined to be 6.572×10^{11} with 2.6% uncertainty. From the MCNP code, the average emission per one fission was 2.447 neutrons, with the energy released during fission of 180.9034 MeV. Based on these values, the reactor's thermal power during irradiation was calculated to be approximately 7.7 W.

Table 31. Experimentally determined reaction rates of activation foils per one atom in precise axial position of measured materials. The unit (1/s).

Axial height (cm)	Position number	Ta	1% Au	Ni
4.55	1	5.023E-27	1.357E-26	3.483E-30
9.55	2	6.072E-27	1.672E-26	4.335E-30
14.55	3	6.545E-27	1.880E-26	4.918E-30
19.55	4	7.121E-27	1.868E-26	5.252E-30
24.55	5	6.998E-27	1.949E-26	5.106E-30
29.55	6	6.774E-27	1.763E-26	4.767E-30
34.55	7	5.708E-27	1.543E-26	4.210E-30
39.55	8	4.599E-27	1.239E-26	3.443E-30
44.55	9	3.350E-27	8.485E-27	2.530E-30
49.55	10	2.303E-27	5.402E-27	-
78.95	11	1.679E-28	-	-

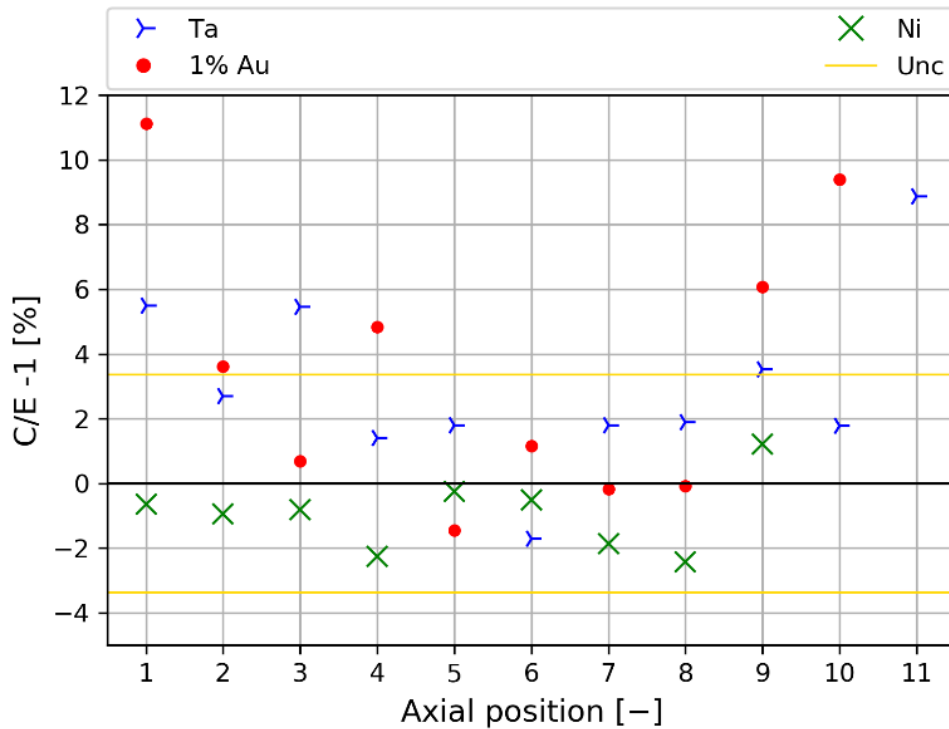


Figure 47. The C/E-1 comparison of calculated reaction rate with experimentally determined for each axial position.

Table 31 shows experimentally determined reaction rates of the activation foils in the defined position on the activation holder. The measurement uncertainty, quantified by the combination of uncertainty of the HPGe detector, uncertainty of the scaling factor, and statistical uncertainty of the calculated spectrum, was determined to be less than 3.37 % for all activation detectors studied. For a better possibility to compare the experimentally obtained results of reaction rates and the calculated result of reaction rates from MCNP, the C/E-1 (calculation/experiment-1) was realized, see Figure 47.

It can be noticed from Table 31 that the maximal reaction rate of all mentioned detectors is reached around position P4. Position P4 corresponds approximately to the middle of the water moderator level. Based on Figure 47 and visualization in Figure 46, the behaviour of the neutron flux can be predicted. Central axial positions P2 to P8 are in very good agreement between calculation and measurement. Position P1 is strongly affected by bottom water and stainless-steel reflector, which deform the neutron flux shape. In the P1 case, the most significant disagreement for the Au of the thermal neutron detector is evident. On the other hand, the highest position P10 in graphite prism also reaches poor agreement in the case of thermal neutrons. This fact can be explained by the large distance from the source of the fission neutrons from the core and by the boundary effect. Another fact that can affect positions P10 and P11 is fission in fuel pins above the moderator level. This phenomenon was previously observed in experiments with graphite blocks. To understand how the axial position affects the shape of the neutron spectrum, the comparison for chosen positions was evaluated, see Figure 48.

The result for the calculated spectrum is in Figure 48. proves that the shape of the neutron spectrum is dependent on its position. Based on the left side chart, position P1 in Figure 48 have the largest share of the thermal neutrons compared to the P4 and P10 position. The percentage of the epithermal neutron is very close. The fast spectrum is more dominant for the upper positions P10. Position P11,

located over the graphite block, is very different from the other positions. It can be seen the very hard neutron flux with a large share of fast neutrons. The maximum of the fast neutron is slightly shifted compared to the positions in the graphite. It is probably caused by leaking the fast neutrons from the core and their subsequent scattering on present materials above water level.

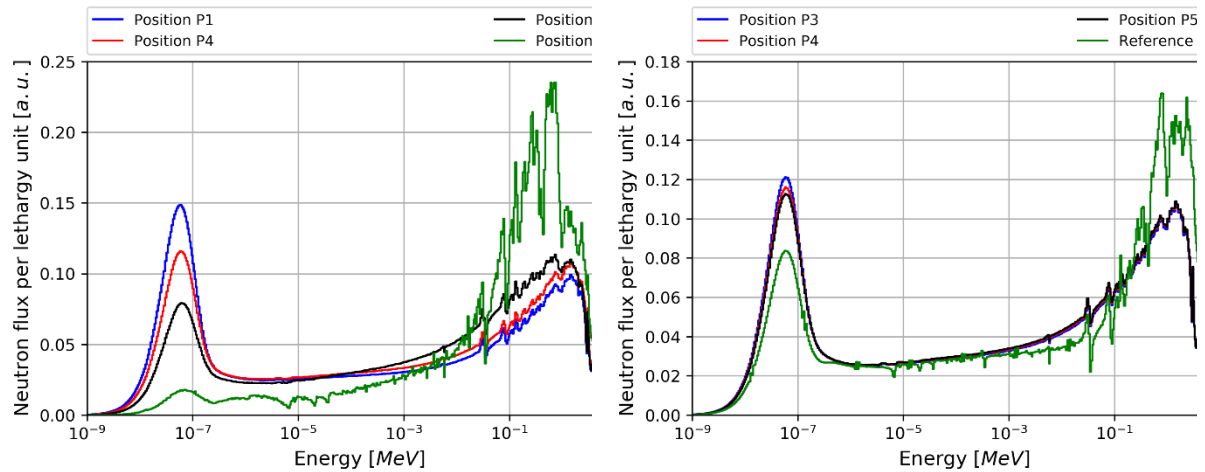


Figure 48. Calculated neutron spectrum in different axial position. Left chart for comparison of farly distant positions, right for comparison differences in central three position compared to the reference neutron field without graphite shaping.

The right chart in Figure 48 represents the comparison of the central positions P3, P4, and P5 in comparison with the reference neutron field on LR-0 [43], [34]. The differences in neutron spectrum shape between positions P3, P4, and P5 are minimal, which is suitable for validation experiments in this area. Positions P3 to P5 are advantageous for another reason, which is the higher absolute neutron flux of the whole graphite prism. This behaviour can be seen from the experimentally obtained reaction rates in Table 31. For better imagination, Figure 49 shows the relative axial neutron flux distribution.

Agreement between experimentally measured activation detectors and the calculation is very close. As a reference position, the P4 was chosen. In the shape of the curve for the calculated neutron profile, there is a change in the curve trend above 43 cm, and the neutron flux almost linearly decreases (positions P9 and P10). This behaviour is caused by the absence of the fission neutrons due to climbing above the critical level of the water moderator. In this region, the discrepancy between experiment and simulation starts increasing, as evident from Figure 47.

The graphite block was inserted into a central dry channel located in the center of the benchmark reference core. The characterization of the cavity in the graphite block performed. As a first validation measurement, the mapping of the reaction rate in a single irradiation experiment was evaluated. A total of 10 axial positions were investigated to find a more suitable position for further use. For thermal mapping the 1% Au activation foils were used, Ta for epithermal and Ni for fast neutron flux mapping. As a more promising axial position for further investigation and validation, the central four position looks promising, position P3 to P6. In this area, the discrepancies between measurement and calculation are below 3% for almost all foils. These positions can be recommended for future experiments, for example with oscillator.

The SACS in various position of small insertion can be found in Table 32 for experiments and for calculations in Table 33. Comparison between both graphite experiments can be seen in Table 34, where the SACS are compared in one reference position. For better understanding how the comparison of the neutron flux shape can be seen in Figure 50.

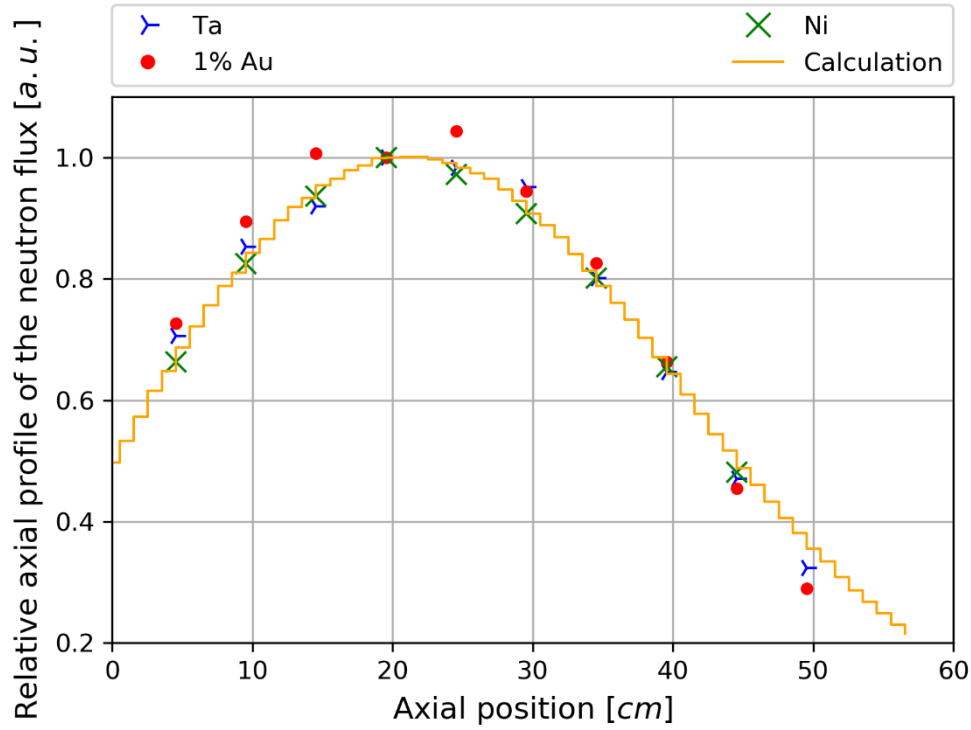


Figure 49. Relative axial neutron flux distribution, comparison between measurement by activation detectors and calculated shape of the neutron flux in central graphite prism.

Table 32: Experimental and SACS in small graphite environment.

Experiment	$^{181}\text{Ta}(n,\gamma)^{182}\text{Ta}$ (b)	$^{197}\text{Au}(n,\gamma)^{198}\text{Au}$ 1% (b)	$^{58}\text{Ni}(n,p)^{58}\text{Co}$ (b)
1	21.0140	56.7636	0.0146
2	21.3772	58.8433	0.0153
3	20.7312	59.5576	0.0156
4	21.5822	56.6096	0.0159
5	21.4681	59.7813	0.0157
6	22.2493	57.9244	0.0157
7	21.3524	57.7203	0.0157
8	21.0098	56.5884	0.0157
9	20.0196	50.7121	0.0151
10	19.1466	44.9185	-
11	7.9774	-	-

Table 33: Calculated SACS in graphite environment (small graphite experiment).

Calculation	$^{181}\text{Ta}(n,\gamma)^{182}\text{Ta}$ (b)	$^{197}\text{Au}(n,\gamma)^{198}\text{Au}$ 1% (b)	$^{58}\text{Ni}(n,p)^{58}\text{Co}$ (b)
1	22.1690	63.0711	0.0145
2	21.9551	60.9721	0.0151
3	21.8635	59.9675	0.0155
4	21.8844	59.3420	0.0156
5	21.8543	58.9166	0.0156
6	21.8683	58.5977	0.0156
7	21.7356	57.6187	0.0155
8	21.4049	56.5435	0.0153
9	20.7251	53.7911	0.0153
10	19.4868	49.1348	-
11	8.6847	-	-

Table 34: Comparison of SACS in both experiments.

Position 4	7 graphite modules		1 graphite module		Reference core [34]
	SACS – CALC (b)	SACS – EXP (b)	SACS – CALC (b)	SACS – EXP (b)	Exp SACS
$^{197}\text{Au}(n,\gamma)^{198}\text{Au}$	88.1426	87.0017	59.3420	56.6096	
$^{63}\text{Cu}(n,\gamma)^{64}\text{Cu}$	1.8585	1.9097	-	-	
$^{58}\text{Fe}(n,\gamma)^{59}\text{Fe}$	0.5408	0.5378	-	-	0.2150
$^{55}\text{Mn}(n,\gamma)^{56}\text{Mn}$	5.5122	5.7667	-	-	
$^{181}\text{Ta}(n,\gamma)^{182}\text{Ta}$	29.7326	29.6577	21.8844	21.5822	
$^{58}\text{Ni}(n,p)^{58}\text{Co}$	-	-	0.0156	0.0159	0.02952

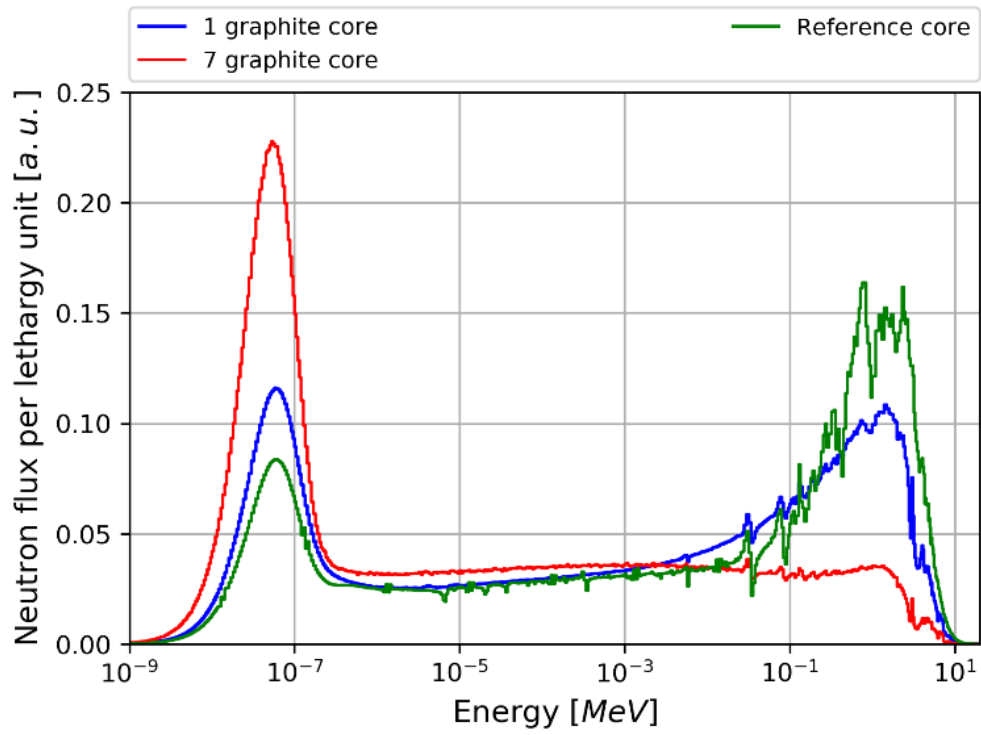


Figure 50: Calculated neutron spectra in current benchmark reference neutron field and in center of modified special core with small graphite insertion and in center of core with large graphite insertion.

6 Summary

The special core has been precisely characterized and now in the center of special core the Benchmark Reference Neutron Field has been identified, being one of 17 benchmark reference neutron fields worldwide. The tail of $^{235}\text{U}(n_{\text{th}}, f)$ PFNS has been monitored by both activation foils and also directly using stilbene measurement. It was proven the previous evaluations also covering JEFF-3.1.1 evaluation is incorrect while new CIELO evaluation which was adopted into ENDF/B-VIII.0 is in good agreement with measured values.

The precisely characterized core surrounding the reference volume was used as driver core in other experiments [41], [36]. When the core is surrounded by stainless steel notable discrepancies are reported. This leads to conclusion that in case of stainless steel still needs to improve cross sections because notable discrepancies were observed.

The kinetic parameters were evaluated as well. Estimated kinetic parameters ($b_{\text{eff}} = 782 \pm 10$ pcm and $L = 39.1 \pm 0.5$ μs) were found very consistent with calculations using MCNP6.1 associated to ENDF-B.VII nuclear data library. Namely 781 pcm for the delayed neutron fraction and 39.05 μs for the neutron generation time). These results are very valuable complements to the characterization of LR-0 reference neutron benchmark field which so far includes only static parameters such as the criticality parameters, the spatial distribution of fission rate and, the spatial and energy distributions of the neutron field in the central cavity. The addition of kinetic parameters highly increases the nuclear data validation potential of LR-0.

The new experiments covering characterization of neutron field in center of graphite insertion has been realized. The agreement with calculation is satisfactory in central position of graphite, while discrepancies are observed in boundary regions. This field are planned to be submitted as new reference neutron field.

The criticality was calculated in three independent codes, MCNP, Serpent, and SCALE. The experiment with a void central block was also realised for evaluating the graphite effect in the reactor core. It is worth noting that a good agreement was reached in the case with the void central block, which confirms a satisfactory description of the driver core. Discrepancies were observed when the central block was filled with graphite.

The spectrum averaged cross section in graphite evaluation was measured in various graphite insertion cores. The experimental values are in good agreement with calculations.

Experimental work done at the LR-0 helped to validate and tune the nuclear data from the new evaluations of IRDFF-II, FENDL-3.2b and ENDF/B-VIII.1 prior to their publication and thus served to the community as intended in frame of this project.

7 References

- [1] Trkov, A., Griffin, P.J., Simakov, S.P., Greenwood, L.R., Zolotarev, K.I., Capote, R., Aldama, D.L., Chechev, V., Destouches, C., Kahler, A.C., Konno, C., Košťál, M., Majerle, M., Malambu, E., Ohta, M., Pronyaev, V.G., Radulović, V., Sato, S., Schulc, M., Šimečková, E., Vavtar, I., Wagemans, J., White, M., Yashima, H., IRDFF-II: A New Neutron Metrology Library, Nuclear Data Sheets, Vol. 163, (2020), pp. 1-108
- [2] G. Schnabel, D.L. Aldama, T. Bohm, U. Fischer, S. Kunieda, A. Trkov, C. Konno, R. Capote, A.J. Koning, S. Breidokaite, T. Eade, M. Fabbri, D. Flammini, L. Isolan, I. Kodeli, M. Košťál, S. Kwon, D. Laghi, D. Leichtle, S. Nakayama, M. Ohta, L.W. Packer, Y. Qiu, S. Sato, M. Sawan, M. Schulc, G. Stankunas, M. Sumini, A. Valentine, R. Villari, A. Žohar, FENDL: A library for fusion research and applications, Nuclear Data Sheets, Volume 193, 2024, Pages 1-78
- [3] Michal Kostal et al., VVER-1000 PHYSICS EXPERIMENTS HEXAGONAL LATTICES (1.275 CM PITCH) OF LOW ENRICHED U(3.3 WT.% U235)O2 FUEL ASSEMBLIES IN LIGHT WATER WITH GRAPHITE AND FLUORIDE SALT INSERTIONS IN CENTRAL ASSEMBLY, IRPhEP, VVER Reactor – VVER, LR(0)-VVER-RESR-003 CRIT-SPEC, NEA/NSC/DOC(2006)1
- [4] Košťál, M., Rypar, V., Juříček, V., The criticality of VVER-1000 mock-up with different H3BO3 concentration, Annals of Nuclear Energy, 2013, 60, pp. 1–7
- [5] Košťál, M., Švadlenková, M., Cvachovec, F., Jánský, B., Milčák, J., Juříček, V., Rypar, V., Kolros, A., Losa, E., Calculation and measurement of neutron flux in internal parts of the VVER-1000 mock-up, Annals of Nuclear Energy, 73, pp. 413-422
- [6] Košťál, M., Rypar, V., Losa, E., Harut, D., Schulc, M., Klupák, V., Matěj, Z., Cvachovec, F., Jánský, B., Novák, E., Czako, T., Juříček, V., Zaritsky, S. The influence of core power distribution on neutron flux density behind a pressure vessel of a VVER-1000 Mock Up in LR-0 reactor, Applied Radiation and Isotopes, 142, pp. 12-21
- [7] M. Košťál, F. Cvachovec, B. Jánský, V. Rypar, V. Juříček, D. Harutyunyan, M. Schulc, J. Milčák, E. Novák, S. Zaritsky, Neutron deep penetration through reactor pressure vessel and biological concrete shield of VVER-1000 Mock-Up in LR-0 reactor, Ann. of Nucl. En., Vol. 94, (2016), pp. 672-683
- [8] Michal Kostal et al., VVER-1000 Mock-up Physics Experiments Hexagonal Lattices (1.275 cm Pitch) of Low Enriched U(2.0, 3.0, 3.3 wt.% 235U)O2 Fuel Assemblies in Light Water with H3BO3, IRPhEP, VVER Reactor – VVER, LR(0)-VVER-RESR-002 CRIT RRATE POWDIS, NEA/NSC/DOC(2006)1
- [9] Kostal M., Cvachovec F., Rypar V., Juříček V., Calculation and measurement of neutron flux in the VVER-1000 mock-up on the LR-0 research reactor, Annals of Nuclear Energy, 2012, 40(1), pp. 25–34
- [10] Szatmary et al., Final report of TIC, Volume 1, Experimental investigations on the physical properties of VVER-type uranium-water lattices, Akademiai Kiado, Budapest 1985, ISBN 963 05 4197 1
- [11] V. Juricek: Experimental workstation “EWS” in the LR-0 reactor control room, UJV Rez Report No. 13044, 2009

- [12] J. Kyncl, V. Rypar, E. Novák: LEU-COMP-THERM-087 „VVER Physics Experiments: Hexagonal Lattices (1.22 cm Pitch) of Low Enriched U(3.6, 4.4 wt.% U235)O2 Fuel Assemblies in Light Water with Variable Fuel Assemblies Pitch”, 2008, NEA/NSC/DOC/(95)03/IV Volume IV
- [13] M. Kostal et al., (2023): Benchmarking of Stainless Steel Cube Neutron Leakage in Research Center Rez, Nuclear Science and Engineering, DOI: 10.1080/00295639.2023.2206770
- [14] L.R. Greenwood, M. Kostal, S. Simakov and A. Trkov, Testing and Improving of the International Reactor Dosimetry and Fusion File, (IRDFF)INDC(NDS)-0731, (<https://www-nds.iaea.org/publications/indc/indc-nds-0731.pdf>)
- [15] J. Wagemans, E. Malambu, and L. Borms, "The Neutron Standard Fields at the BR1 Reactor at SCK•CEN," Journal of ASTM International 9, no. 3 (2012): 1-7
- [16] Košťál, M., Schulc, M., Šimon, J., Burianová N., Harutyunyan D., Losa, E., Rypar, V., Measurement of various monitors reaction rate in a special core at LR-0 reactor, Annals of Nuclear Energy, 2018, 112, pp. 759–768
- [17] E.M.Zsolnay, R. Capote, H.K. Nolthenius, and A. Trkov, Technical report INDC(NDS)-0616, IAEA, Vienna, 2012.
- [18] R. Capote, K.I. Zolotarev, V.G. Pronyaev, and A. Trkov, Journal of ASTM International (JAI)- 9, Issue 4, 2012, JAI104119
- [19] T. Goorley, et al., "Initial MCNP6 Release Overview", Nuclear Technology, **180**, pp 298-315 (Dec 2012).
- [20] P. Dryak, P. Kovar, Experimental and MC determination of HPGe detector efficiency in the 40–2754 keV energy range for measuring point source geometry with the source-to-detector distance of 25 cm, Appl. Rad. and Isot., Vol. 64, Issues 10–11, 2006, pp. 1346-1349
- [21] V.Radulovic V., Jaćimović R., Pungeričič A., Vavtar I., Snoj L., Trkov A., Characterization of the neutron spectra in three irradiation channels of the JSI TRIGA reactor using the GRUPINT spectrum adjustment code, Nuclear Data Sheets, Volume 167, July–August 2020, Pages 61-75
- [22] M. Košťál, Z. Matěj, E. Losa, O. Huml, M. Štefánik, F. Cvachovec, M. Schulc, B. Jánský, E. Novák, D. Harutyunyan, V. Rypar, On similarity of various reactor spectra and ²³⁵U Prompt Fission Neutron Spectrum, Appl. Rad. and Isot., Vol. 135, (2018), pp. 83–91
- [23] V.I. Kuchtevic, O. A. Trykov, L.A. Trykov, Odnokrystalnyj scintillacionnyj spektrometr, Atomizdat, Moscow 1971, (in Russian)
- [24] Willem G.J. Langeveld, Andrew M. Glenn, Steven A. Sheets, Dan A. Strellis, Natalia P. Zaitseva, Comparison of pulse shape discrimination performance of stilbene and liquid scintillator under high count-rate active interrogation conditions, Nuclear Instruments and Methods in Physics Research Section A: Accelerators, Spectrometers, Detectors and Associated Equipment, Vol.954, 2020, 161204,
- [25] Cvachovec, F., Cvachovec, J., Tajovsky, P., Anisotropy of light output in response of stilbene detectors, Nuclear Instruments and Methods in Physics Research, Section A: Accelerators, Spectrometers, Detectors and Associated Equipment, Vol. 476 (1-2), pp. 200-202, 2002

- [26] Košťál, M.; Šoltés, J.; Viererbl, L.; Matěj, Z.; Cvachovec, F.; Rypar, V.; Losa, E.; Measurement of neutron spectra in a silicon filtered neutron beam using stilbene detectors at the LVR-15 research reactor, *Appl. Rad. and Isot.*, 128, 2017, pp. 41-48
- [27] Matej et al., The methodology for validation of cross sections in quasi monoenergetic neutron field, *Nuclear Inst. and Methods in Physics Research*, A 1040 (2022) 167075
- [28] Košťál, M., Losa, E., Matěj, Z., Juříček, V., Harutyunyan, D., Huml, O., Štefánik, M., Cvachovec, F., Mravec, F., Schulc, M., Czako, T., Rypar, V., Characterization of mixed N/G beam of the VR-1 reactor, *Annals of Nuclear Energy*, 122, (2018), pp. 69-78.
- [29] Košťál, M., Rypar, V., Losa, E., Harut, D., Schulc, M., Klupák, V., Matěj, Z., Cvachovec, F., Jánský, B., Novák, E., Czako, T., Juříček, V., Zaritsky, S., The influence of core power distribution on neutron flux density behind a pressure vessel of a VVER-1000 Mock Up in LR-0 reactor, *Applied Radiation and Isotopes*, 142, (2018), pp. 12-21.
- [30] Matej, Z., Kostal, M., Novak, E., Alexa, P., Uhlár, R., Mravec, F., Jancar, A., Cvachovec, F., Prenosil, V., Jancar, P., Characterization and comparison of neutron generators of IEC and linear D-T by the spectrometric system NGA-01, (2020) *International Conference on Physics of Reactors: Transition to a Scalable Nuclear Future, PHYSOR 2020*, 2020-March, pp. 2786-2793.
- [31] Michal Kostal, Martin Schulc, Evzen Novak, Tomas Czako, Zdenek Matej, Frantisek Cvachovec, Filip Mravec, Bohumil Jansky and Luiz Leal, Validation of heavy water cross section using AmBe neutron source, *EPJ Web Conf.*, 239 (2020) 18008
- [32] Jansky, B., Novak, E., Neutron spectrometry with spherical hydrogen proportional detectors, *Nuclear Instruments and Methods in Physics Research, Section A: Accelerators, Spectrometers, Detectors and Associated Equipment*, 2014, 735, pp. 390–398
- [33] Košťál M., Rypar V., Schulc M., Losa E., Baroň P., Mareček M., Uhlíř M.; Measurement of $^{75}\text{As}(n,2n)$ cross section in well-defined spectrum of LR-0 special core, *Ann. of Nucl. En.*, Vol. 100, Part 2, 2017, pp 42-49
- [34] M. Košťál et al., Measurement of spectrum averaged cross sections in LR-0 benchmark reference neutron field, *Ann. of Nucl. En.*, 206, (2024), 110616
- [35] M. Kostal et al., Measurement of the High Energy Gamma Spectrum Up to 13 MeV in the Special Core of the LR-0 Reactor, *Proceedings of International Conference on Physics of Reactors (PHYSOR 2024) | San Francisco, CA, April 21-24, 2024*, Pages 306-313
- [36] Košťál, M., Švadlenková, M., Baroň, P., Rypar, V., Milčák, J., Determining the axial power profile of partly flooded fuel in a compact core assembled in reactor LR-0, *Annals of Nuclear Energy*, Vol. 90, 2016, pp. 450-458, ISSN 0306-4549
- [37] Košťál M., Švadlenková M., Milčák J., Absolute determination of power density in the VVER-1000 mock-up on the LR-0 research reactor, *Applied Radiation and Isotopes*, Vol. 78, 2013, pp 38-45, ISSN 0969-8043, pp. 10.1016/j.apradiso.2013.03.094

- [38] Bergmann, U.C., Chawla, R., Jatuff, F., Murphy, M.F., Optimised non-invasive method to determine ^{238}U -captures-to-total-fissions in reactor fuel, Nuclear Instruments and Methods in Physics Research, Section A: Accelerators, Spectrometers, Detectors and Associated Equipment, 556(1), pp. 331–338
- [39] Owen T.D., Measurement of power and burn-up in irradiated nuclear reactor fuel by a non-destructive method, Br. J. Appl. Phys., 14 (1963), pp. 456-458
- [40] Adimir dos Santos, Leda C.C.B. Fanaro, Graciete S. de Andrade e Silva, Arlindo G. Mendonça, The experimental determination and evaluation of the three-dimensional fission density distribution of the IPEN/MB-01 research reactor facility for the IRPhE project, Annals of Nuclear Energy, Vol. 38, Issues 2–3, 2011, pp. 418-430,
- [41] Košťál, M., Losa, E., Czako, T., Schulc, M., Simon, J., Juricek, V., Rypar, V., Ulmanova, J., Trkov, A., Capote, R., The effect of heavy reflector on neutronic parameters of core, Annals of Nuclear Energy, 2022, 168, 108898
- [42] Czako, T., Košťál, M., Simon, J., Soltés, J., Mareček, M., Capote, R., Comprehensive validation of silicon cross sections, Nuclear Engineering and Technology, Vol. 52, (2020), pp. 2717-2724
- [43] Košťál, M., Schulc, M., E. Losa, E., Simon, J., Burianova, N., Novak, E., Mareček, M., Uhlir, J., Czako, T., Rypar, V., Juricek, V., Capote, R., Trkov, A., A reference neutron field for measurement of spectrum averaged cross sections, Ann. of Nucl. En., Vol. 140, (2020), 107119
- [44] Michal Kostal et al., VVER-1000 PHYSICS EXPERIMENTS HEXAGONAL LATTICES (1.275 CM PITCH) OF LOW ENRICHED U(3.3 WT.% U235)O2 FUEL ASSEMBLIES IN LIGHT WATER 75AS(N, 2N), 23NA(N,2N), 90ZR(N,2N), 89Y(N,2N) REACTION RATES, Fundamental - FUND, LR(0)-FUND-RESR-001 CRIT-RRATE, NEA/NSC/DOC(2006)1
- [45] Burianova, N., Kostal, M., Schulc, M., Simon, J., Mareček, M., Uhlir, J., Measurement of selected differential cross sections in ^{235}U spectrum, (2019) Journal of Nuclear Engineering and Radiation Science, 5 (3), art. no. 030906
- [46] Kostal, M., Czako, T., Losa, E., Schulc, M., Juříček, V., Šimon, J., Rypar, V., Mareček, M., Capote, R., Trkov, A., Measurement of integral cross sections of selected dosimetry reactions in LR-0 reactor, (2020) International Conference on Physics of Reactors: Transition to a Scalable Nuclear Future, PHYSOR 2020, 2020-March, pp. 1857-1864.
- [47] Košťál, M., Schulc, M., Rypar, V., Losa E., Burianová N., Šimon J., Mareček, M., Uhlíř, J., Validation of zirconium isotopes (n,g) and (n,2n) cross sections in a comprehensive LR-0 reactor operative parameters set, Applied Radiation and Isotopes 128 (2017) 92–100
- [48] A. BRUGGEMAN, W. Maenhaut, and J. HOSTE, "The Total Average Cross Section for the Reactions $^{58}\text{Ni}(n,np)^{57}\text{Co}$, $^{58}\text{Ni}(n,pn)^{57}\text{Co}$, and $^{58}\text{Ni}(n,d)^{57}\text{Co}$ in a Fission Type Reactor Spectrum," Radiochem. Radioanal. Lett., 18, 87 (1974).
- [49] R. WÖLFLE and S. M. QAIM, "Measurement of Fission Neutron Spectrum Averaged Cross-Sections for Some (n, p), (n, n'p) and (n, a) Reactions on Nickel and Chromium," Radiochim. Acta, 27, 65 (1980).

- [50] O. HORIBE and H. CHATANI, "Cross Section for the Reactions $^{55}\text{Mn}(n,2n)^{54}\text{Mn}$, $^{58}\text{Ni}(n,2n)^{57}\text{Ni}$ and $^{58}\text{Ni}(n,np)^{57}\text{Co}$ Averaged over the ^{235}U Fission Neutron Spectrum," Proc. Int. Conf. Nuclear Data for Science and Technology, Jülich, Germany, 1991, S. M. QAIM, Ed., Springer Verlag, Berlin, Germany (1992).
- [51] J.H. ZAIDI, H.M. A. KARIM, M. ARIF, I.H. QURESHI, and S.M. QAIM, "Measurement of Fission Neutron Spectrum Averaged Cross-Sections on Nickel: Small Scale Production of ^{57}Co in a Nuclear Reactor," *Radiochim. Acta*, 60, 169 (1993)
- [52] M.A. Arribére, S. Ribeiro Guevara, P.M. Suárez, A.J. Kestelman, Threshold Reaction Cross Sections of Nickel Isotopes, Averaged Over a ^{235}U Fission Neutron Spectrum", *Nuclear Science and Engineering*, 139, 2001, pp. 24–32
- [53] M. Kostal, E. Losa, M. Schulc, J. Simon, T. Bily, V. Rypar, M. Marecek, J. Uhlír, T. Czako, R. Capote, A. Trkov, S. Simakov, Validation of IRDFF-II library in VR-1 reactor field using thin targets, *Ann. of Nucl. Energy* 158, (2021), 108268
- [54] Košťál M. et al., Impact of reactor neutron spectrum on measured spectrum averaged, *Ann. of Nucl. En.*, Vol. 179, (2022), 109418
- [55] D.A. Brown, M.B. Chadwick, R. Capote et al, "ENDF/B-VIII.0.0: The 8th Major Release of the Nuclear Reaction Data Library with CIELO-project Cross Sections, New Standards and Thermal Scattering Data", *Nucl. Data Sheets*, 148 (2018), pp. 1–142.
- [56] V. Radulovic et al., INDC(NDS)-0746 (<https://www-nds.iaea.org/publications/indc/indc-nds-0746.pdf>)
- [57] M. Schulc, Michal Kostal, Jan Simon, Filip Brijar, Tomas Czako, Jiri Maly, Constraining high energy tail of $^{235}\text{U}(n_{th},f)$ prompt fission neutron spectrum, *Applied Radiation and Isotopes*, Vol. 166, (2020), p. 109313
- [58] Michal Košťál, Vojtěch Rypar, Ján Milčák, Vlastimil Juříček, Evžen Losa, Benoit Forget, Sterling Harper, Study of graphite reactivity worth on well-defined cores assembled on LR-0 reactor, *Ann. of Nucl. En.*, Vol. 87, 2016, pp. 601-611, ISSN 0306-4549
- [59] Kostal, M., Losa, E., Schulc, M., Simon, J., Bily, T., Rypar, V., Marecek, M., Uhlír, J., Czako, T., Capote, R., Trkov, A., Simakov, S., Validation of IRDFF-II library in VR-1 reactor field using thin targets, *Ann. of Nucl. Energy* 158, (2021), 108268
- [60] Schulc, M., Košťál, M., Šimon, J., Novák, E., Mareček, M., Kubín, R., Validation of IRDFF-II library by means of ^{252}Cf spectral averaged cross sections, *Applied Radiation and Isotopes*, 155, (2020) , 108937,
- [61] Košťál, M., Losa, E., Schulc, M., Czako, T., Peltan, T., Simon, J., Juricek, V., Rypar, V., Thiollay, N., Destouches, Ch., Radulovic, V., Trkov, A., Capote, R., Testing of various neutron filters in reference neutron field in LR-0 reactor for nuclear data validation and verification, *Applied Radiation and Isotopes*, 2021, 169, 109566

- [62] Košťál, M., Losa, E., Schulc, M., Šimon J., Matěj Z., Antoš M., Vadják Š., Cuhra M., Cvachovec F., Mravec F., Brijar F., Czako, T., Rypar, V., The methodology of characterization of neutron leakage field from PET production cyclotron for experimental purposes, *Nuclear Inst. and Methods in Physics Research, A*, vol. 942, (2019), 162374
- [63] J.-L. Munoz-Cobo, G. Verdu, "Neutron stochastic transport theory with delayed neutron," *Ann. Nucl. Energy*, Vol.14 n°7, 1987.
- [64] E. F. Bennet, "An experimental method for reactor noise measurement of effective beta," Argonne National Laboratory report, ANL-81-72, 1981.
- [65] B Geslot et al., A pile noise experiment in the reference core of the nuclear research reactor LR-0, *Ann. of Nucl. En.*, 189, (2023), p. 109833
- [66] T. Peltan et al., Validation of graphite cross section in various integral experiments, THE PROCEEDINGS OF THE INTERNATIONAL CONFERENCE ON NUCLEAR ENGINEERING (ICONE) 2019.27:2083, [HTTPS://DOI.ORG/10.1299/JSMEICONE.2019.27.2083](https://doi.org/10.1299/jsmeicone.2019.27.2083)

Appendix: gamma spectrometry data

Used parameters

			peak	Branch ratio	gamma	Efficiency of detection	True summation correction	Concentration	isotopic comp.	Mr [g/mol]	A / A sat
	197Au(n,g)		411	0.95	8E-2.9					196.	2.9
Au)	198Au	EG3	.8	6	8.30E-02	0.998	1.00	1.000	54	0E-01
			EG3 - Ni	810		1.1				966	1.4
Ni	58Ni(n,p)		EG3 - Ni	.75	0.99	3E-07	4.54E-02	0.937	0.681	58.6	7E-02
Fe			folie 1 x 1	93	5	07		99.5		934	3.3
0.1m	54Fe(n,p)	EG3 - Fe1 x 1cm,		.84	1.00	7E-08	4.43E-02	1.000	0.058	55.8	7E-03
Fe		tl 0.1mm		8	0	08		100.		45	9.5
0.4m	56Fe(n,p)	EG3 - Fe1 x 1cm,		.76	0.98	7E-05	4.30E-02	0.939	0.918	55.8	2E-01
		tl 0.4mm		76	9	05		100.		45	9.5
				181	0.26	7E-05		100.		55.8	2E-01
				0.7	9	05	2.30E-02	0.814	0.918	45	3.3
				834		2.5		100.		55.8	7E-03
	54Fe(n,p)	EG3 - Fe1 x 1cm,		.84	1.00	7E-08	4.35E-02	1.000	0.058	45	2.3
		tl 0.4mm		8	0	08		100.		55.8	7E-03
						1.8		100.		45	2.3
	58Fe(n,g)	EG3 - Fe1 x 1cm,		109	0.56	0E-07	3.46E-02	1.000	0.003	55.8	2E-02
		tl 0.4mm		9.2	5	07		100.		45	6.1
						1.2		100.		55.8	2E-02
Al	27Al(n,A)	24Na	Al plate	136	1.00	8E-05	2.90E-02	0.863	1.000	26.9	9E-01
				8.6	0	05		100.		82	1.4
				810		1.1		100.		934	0.2
Ni	58Ni(n,p)	58Co	16x16 x1	.75	0.99	3E-07	4.61E-02	0.933	0.681	58.6	7E-02
				93	5	07		100.		934	3.8
						2.9		100.		58.6	7E-03
				122	0.85	5E-08	1.48E-01	1.000	0.681	934	5.4
						4.1		100.		58.6	7E-04
				117	0.99	7E-09	3.44E-02	0.825	0.262	934	5.4
				3	9	09		100.		58.6	7E-04
						4.1		100.		934	0.4
				133	1.00	7E-09	3.10E-02	0.819	0.262	934	0.4
				2	0	09		100.		180.	9.1
Ta	181Ta(n,g)	182Ta	EG3	112	0.35	9E-08	3.56E-02	0.867	1.000	99	0E-03
				1	1	08		100.		947	2E-03
				122		6.9		100.		180.	9.1
				1.3	0.27	9E-08	3.31E-02	0.940	1.000	99	2E-03
				95	1	08		100.		947	2E-03
Mo	92Mo(n,p)92*	EG3		934	0.99	0E-07	3.98E-02	1.000	0.148	95.9	6E-02
in				.4	2	07		100.		5	0E-02
EG3						7.9		100.		92.9	9.5
Nb	93Nb(n	EG3		934	0.99	0E-07	4.10E-02	1.000	1.000	063	6E-02
pelle	92Nb	,2n)92*	D=18, th.	.4	2	07		100.		7	0E-02
t			1	898	0.93	2E-07		100.		88.9	1E-02
						7.5		100.		06	0E-03
Y	89Y(n,2n)	88Y	D=2.57, tl=1.27	.04	0.93	2E-08	4.15E-02	0.846	1.000	88.9	1E-03
plate				2	7	08		100.		06	0E-03

Measured data

End of irradiation		6.8.20 19:38		Geom	NPA	uncertainty	Start	Live time	Real time	
	AF	pozi	m (mg)	erie	coun	measur	(s)	(s)	(s)	
		ce			ts	ement				
411 keV	Au5	1_4	3.26	foil in EG3	D=3.6m m th 0.1	1136 9	108.12	7.8.20 9:57	644.1	644.5
411 keV	Au11	2_4	3.47	foil in EG3	D=3.6m m th 0.1	8216 1286	92.20	7.8.20 11:44	477.3	477.6
411 keV	Au13	3_4	3.31	foil in EG3	D=3.6m m th 0.1	0 2304	115.65	7.8.20 10:27	724.0	724.4
411 keV	Au32	4_4	3.29	foil in EG3	D=3.6m m th 0.1	6 1688	153.91	7.8.20 11:08	1350.	1351.
810 keV	Ni1-A	1_4	61.8	foil in EG3	1 x 1 x 0.1mm	6 4733	139.03	06.10.202 0 9:28	2175	2176
810 keV	Ni-1B	1_4	63.3	foil in EG3	1 x 1 x 0.1mm	0 4310	238.53	06.10.202 0 15:39	6091	6092
810 keV	Ni-2A	2_4	61.8	foil in EG3	1 x 1 x 0.1mm	9 5911	228.81	07.10.202 0 18:31	5704	5705
810 keV	Ni-2B	2_4	72.5	foil in EG3	1 x 1 x 0.1mm	80.39 4331	80.39	08.10.202 0 11:35	6617.	6618.
810 keV	Ni-3A	3_4	71.9	foil in EG3	1 x 1 x 0.1mm	4331 3422	70.73	09.10.202 0 14:52	5038.	5039.
810 keV	Ni-3B	3_4	62.6	foil in EG3	1 x 1 x 0.1mm	62.27 4688	62.27	09.10.202 0 16:15	4735.	4736.
810 keV	Ni-4A	4_4	66.1	foil in EG3	1 x 1 x 0.1mm	72.56 2614	72.56	12.10.202 0 15:01	6318.	6319.
810 keV	Ni-4B	4_4	70.5	foil in EG3	1 x 1 x 0.1mm	161.34 1997		18.8.20 9:55	2541.	2549.
1121 keV	Ta-1	1_5	21.01	foil in EG3	D=3.6m m th 0.1	1 2	161.34	18.8.20 9:55	2541.	2549.
1221,395 keV	Ta-1	1_5	21.01	foil in EG3	D=3.6m m th 0.1	2 7274	155.73	18.8.20 9:55	2541.	2549.
1231,395 keV	Ta-1	1_5	21.01	foil in EG3	D=3.6m m th 0.1	101.62 3656	101.62	18.8.20 9:55	2541.	2549.
1121 keV	Ta-2	2_5	21.23	foil in EG3	D=3.6m m th 0.1	7 2816	190.51	18.8.20 10:40	3490.	3501.
1221,395 keV	Ta-2	2_5	21.23	foil in EG3	D=3.6m m th 0.1	3 1033	187.57	18.8.20 10:40	3490.	3501.
1231,395 keV	Ta-2	2_5	21.23	foil in EG3	D=3.6m m th 0.1	9 2744	131.98	18.8.20 10:40	3490.	3501.
1121 keV	Ta-3	3_5	21.2	foil in EG3	D=3.6m m th 0.1	5 2086	165.44	18.8.20 11:40	2623.	2631.
1221,395 keV	Ta-3	3_5	21.2	foil in EG3	D=3.6m m th 0.1	6 7881	160.70	18.8.20 11:40	2623.	2631.
1231,395 keV	Ta-3	3_5	21.2	foil in EG3	D=3.6m m th 0.1	105.46 4831	105.46	18.8.20 11:40	2623.	2631.
1121 keV	Ta-4	4_5	21.13	foil in EG3	D=3.6m m th 0.1	1 3769	219.57	18.8.20 12:24	4756.	4770.
1221,395 keV	Ta-4	4_5	21.13	foil in EG3	D=3.6m m th 0.1	6 1381	217.03	18.8.20 12:24	4756.	4770.
1231,395 keV	Ta-4	4_5	21.13	foil in EG3	D=3.6m m th 0.1	131.70 1	131.70	18.8.20 12:24	4756.	4770.

810 keV	Ni-1	1_6	68.8	foil in EG3	1 x 1 x 0.1mm	1049 6	109.64	05.10.202 0 11:04	1146 2.3	1146 4.5
834 keV	Fe-1	1_6	87.9	foil in EG3	1 x 1 x 0.1mm	4648	127.34	19.8.20 16:21	1470 21.1	1470 40.3
810 keV	Ni-2	2_6	69.8	foil in EG3	1 x 1 x 0.1mm	1004 0	108.41	05.10.202 0 14:16	1126 3.3	1126 5.3
834 keV	Fe-2	2_6	71.1	foil in EG3	1 x 1 x 0.1mm	5289	133.80	24.8.20 9:50	1912 18.9	1912 44.1
810 keV	Ni-3	3_6	69.2	foil in EG3	1 x 1 x 0.1mm	4841 5	232.31	05.10.202 0 17:26	5759 0.7	5760 0.9
834 keV	Fe-3	3_6	90.8	foil in EG3	1 x 1 x 0.1mm	5346	145.68	26.8.20 15:01	1595 48.8	1595 69.3
810 keV	Ni-4	4_6	68.2	foil in EG3	1 x 1 x 0.1mm	4884 9	343.25	12.10.20 16:44	6297 7.8	6298 8.8
834 keV	Fe-4	4_6	78.7	foil in EG3	1 x 1 x 0.1mm	6834	161.70	28.8.20 11:36	2612 67.7	2613 03.5
411 keV	Au15	1_7	3.12	foil in EG3	D=3.6m m th 0.1	2290 8	154.25	7.8.20 9:34	1342. 2	1343. 0
411 keV	Au26	2_7	3.22	foil in EG3	D=3.6m m th 0.1	1591 4	127.95	7.8.20 10:10	937.3	937.9
411 keV	Au27	3_7	3.23	foil in EG3	D=3.6m m th 0.1	1062 9	104.29	7.8.20 10:55	630.7	631.1
411 keV	Au53	4_7	3.46	foil in EG3	D=3.6m m th 0.1	1199 4	111.11	7.8.20 10:42	712.6	713.1
411 keV	Au45	4_4 -2	3.15	foil in EG3	D=3.6m m th 0.1	1343 6	117.79	7.8.20 11:53	852.7	853.1
411 keV	Au46	4_7 +2	3.63	foil in EG3	D=3.6m m th 0.1	8097	91.40	7.8.20 11:35	491.5	491.8
810 keV	Ni-5A	1_7	63.9	foil in EG3	1 x 1 x 0.1mm	1065 3	109.51	07.10.202 0 8:32	1332 0.7	1332 3.1
810 keV	Ni-5B	1_7	64.7	foil in EG3	1 x 1 x 0.1mm	3145	59.19	08.10.202 0 10:25	3988. 8	3989. 6
810 keV	Ni-6A	2_7	65	foil in EG3	1 x 1 x 0.1mm	4479 1	225.85	08.10.202 0 17:39	5677 5.4	5678 5.4
810 keV	Ni-6B	2_7	73.2	foil in EG3	1 x 1 x 0.1mm	1698 2	137.95	09.10.202 0 9:32	1912 3.0	1912 6.5
810 keV	Ni-7A	3_7	65.1	foil in EG3	1 x 1 x 0.1mm	1777 69	451.99	09.10.202 0 17:39	2306 81.3	2307 21.6
810 keV	Ni-7B	3_7	66.5	foil in EG3	1 x 1 x 0.1mm	1469 1	127.84	12.10.202 0 9:46	1870 2.9	1870 6.2
810 keV	Ni-8A	7_7	66.9	foil in EG3	1 x 1 x 0.1mm	1073 1	114.07	13.10.202 0 10:17	1429 0.5	1429 2.9
810 keV	Ni-8B	7_7	68	foil in EG3	1 x 1 x 0.1mm	5658	83.57	13.10.202 0 14:14	7340. 9	7342. 2
1368 keV	Al1	Ref	998.15	End cap	D=1.27 th=3mm	8868	98.24	06.08.202 0 22:59	933.9	935.6
1368 keV	Al2	Ref	1000.5	End cap	D=1.27 th=3mm	1075 8	108.03	06.08.202 0 23:16	1128. 3	1130. 2
1368 keV	Al4	Ref	7	End cap	D=1.27 th=3mm	9328	101.60	06.08.202 0 23:43	1018. 6	1020. 3
1368 keV	Al6	Ref	991.76	End cap	D=1.27 th=3mm	1096 4	108.87	07.08.202 0 0:02	1173. 0	1175. 0
159,4 keV	Ti D5	Ref	742.9	End cap	Ti-D5 1x1.2x0.1	1272 95	378.61	07.08.202 0 12:15	8378. 8	8383. 3

889,3 keV	Ti D5	Ref	742.9	End cap	Ti-D5 1x1.2x0.1	1518	60.44	07.08.2020	8378.8	8383.3
983,5 keV	Ti D5	Ref	742.9	End cap	Ti-D5 1x1.2x0.1	6232	91.68	07.08.2020	8378.8	8383.3
1037,5 keV	Ti D5	Ref	742.9	End cap	Ti-D5 1x1.2x0.1	5733	92.91	07.08.2020	8378.8	8383.3
159,4 keV	Ti1		176.1			1142		07.08.2020	3074	3075
889,3 keV	Ti1		176.1			58	387.31	07.08.2020	3074	3075
983,5 keV	Ti1		176.1			1292	74.99	07.08.2020	3074	3075
1037,5 keV	Ti1		176.1			5978	99.27	07.08.2020	3074	3075
159,4 keV	Ti2	Ref	184.4	End cap		1087		10.08.2020	6133	6134
889,3 keV	Ti2	Ref	184.4	End cap		19	377.68	10.08.2020	6133	6134
983,5 keV	Ti2	Ref	184.4	End cap		2477	77.22	10.08.2020	6133	6134
1037,5 keV	Ti2	Ref	184.4	End cap		2934	85.03	10.08.2020	6133	6134
834 keV	Mn	Ref	1995.5	End cap		2518	86.35	10.08.2020	6133	6134
1173 keV	Cu kolecko	Ref	17590.	End cap		7316	152.95	02.10.2020	2379	2380
1332 keV	Cu kolecko	Ref	17590.	End cap		0		0 16:44	92.4	22.5
1173 keV	Cu plisek	Ref	23076.	End cap		2171	89.38	22.09.2020	5818	5819
1332 keV	Cu plisek	Ref	23076.	End cap		0		0 17:02	8.3	6.4
934,4 keV	Nb-111	Ref	198.09	foil in EG3		2012	71.72	22.09.2020	5818	5819
934,4 keV	Nb-kolecko	Ref	2228.6	End cap		1	1.04190	23.09.2020	6889	6890
810 keV	Ni-222	Ref	2184.4	End cap	16 x 16 x 1mm	3344	E+02	23.09.2020	6889	6890
122 keV	Ni-222	Ref	2184.4	End cap		2997	7.57500	23.09.2020	6889	6890
1173 keV	Ni-222	Ref	2184.4	End cap				0 12:53	0.6	0.8
1332 keV	Ni-222	Ref	2184.4	End cap				0 12:53	0.6	0.8
934,4 keV	Mo	Ref	264.11	foil in EG3		2340		10.08.2020	2648	2649
898 keV	Y-7	Ref	2944.7	End cap	D=2.57, tl=1.27	6	360.24	0 10:20	0	6.4
1836 keV			2944.7			2742		31.08.2020	7085	7106
						696	1738.36	0 14:35	8.9	0.8
						5483	710.86	0 14:35	8.9	0.8
						1146		31.08.2020	7085	7106
						9	169.93	0 14:35	8.9	0.8
						1027		31.08.2020	7085	7106
						2	124.62	0 14:35	8.9	0.8
						2026	1.73870	11.08.2020	9227	9253
						0	E+02	0 10:48	3.4	0.5
						1158		18.09.2020	3274	3274
						5	193.86	0 15:55	38.6	83.4
						6951	116.96	18.09.2020	3274	3274
								0 15:55	38.6	83.4

	Fe 4									
846 keV	platky v EG3	Ref .	330.9	foil in EG3	1 x 1 x 0.4mm	1379 9	1.23530 E+02	06.08.202 0 21:44	4333. 6	4335. 3
1810 keV			330.9			1702	4.57700 E+01	06.08.202 0 21:44	4333. 6	4335. 3
834 keV			330.9			564	38.54	06.08.202 0 21:44	4333. 6	4335. 3
834 keV			330.9			3048	2.38050 E+02	14.08.202 0 10:59	2604 19.7	2604 57.6
1099 keV			330.9			4006	2.77750 E+02	14.08.202 0 10:59	2604 19.7	2604 57.6
834 keV	54Fe	Ref .	127.3	foil in EG3		6270 5	271.17	17.08.202 0 11:20	8122 5.1	8123 8.3
320 keV			127.3			1096	106.49	17.08.202 0 11:20	8122 5.1	8123 8.3
834 keV	54Fe	Ref .	127.3	foil in EG3		6996	8.97050 E+02	04.09.202 0 15:10	9472 58	9474 14.3
320 keV			127.3			8244	4.48640 E+02	04.09.202 0 15:10	9472 58	9474 14.3
983.5 keV	V	Ref .	495.5	foil in EG3		6879	1.63020 E+02	07.08.202 0 14:36	2425 34.6	2425 69.7
1037.5 keV			495.5			6175	1.59870 E+02	07.08.202 0 14:36	2425 34.6	2425 69.7
333 keV	Au	Ref .	2555.8	End cap		1100 1	1401.96	1.9.20 12:14	8026 7.5	8151 3.8
355 keV			2555.8			5429 4	1480.42	1.9.20 12:14	8026 7.5	8151 3.8

Appendix: data fitting results

Before fitting, PSD were calculated using Bartlett's method (average periodogram) and rescaled to the average currents of the detectors. The resolution of the spectrum is 1 Hz, and the frequencies range to 150 Hz. PSD were then fitted using Matlab R2020b (non linear *fit* function with trusted-region algorithm). Results are given in the following tables. APSDs were fitted using equation (3), whereas CPSDs were fitted without the constant. In the following tables, the term "uncertainty" refer to come the statistical error associated to the measurement.

Table 35: Results for Detector 2 (APSD).

Run	Amplitude (/Hz)		Decay constant (s ⁻¹)		Constant (/Hz)		Delayed neutron fraction (pcm)		Generation time (μs)	
	Value	Uncer.	Value	Uncer.	Value	Uncer.	Value	Uncer.	Value	Uncer.
1	6.83E-07	9.55E-09	2.01E+02	4.53E+00	5.38E-07	3.30E-09	784.2	5.5	39.0	0.9
8	6.92E-07	4.13E-09	2.00E+02	1.91E+00	5.41E-07	1.42E-09	781.0	2.3	39.1	0.4
9	1.07E-07	5.30E-10	2.01E+02	1.59E+00	8.31E-08	1.82E-10	774.7	1.9	38.5	0.3
2	6.89E-07	6.80E-09	2.00E+02	3.28E+00	7.03E-07	2.53E-09	780.0	3.8	39.0	0.7
7	6.87E-07	7.25E-09	1.99E+02	3.50E+00	7.10E-07	2.70E-09	780.0	4.1	39.2	0.7
6	6.74E-07	7.13E-09	2.07E+02	3.72E+00	7.04E-07	2.82E-09	785.2	4.2	37.9	0.7
3	6.87E-07	7.81E-09	2.08E+02	4.02E+00	7.01E-07	3.08E-09	777.9	4.4	37.4	0.8
4	6.92E-07	7.07E-09	2.04E+02	3.51E+00	7.05E-07	2.72E-09	776.8	4.0	38.1	0.7
5	6.83E-07	9.55E-09	2.01E+02	4.53E+00	5.38E-07	3.30E-09	784.2	4.0	39.0	0.7

Table 36: Results for Detector 1 (APSD).

Run	Amplitude (/Hz)		Decay constant (s ⁻¹)		Constant (/Hz)		Delayed neutron fraction (pcm)		Generation time (μs)	
	Value	Uncer.	Value	Uncer.	Value	Uncer.	Value	Uncer.	Value	Uncer.
1	7.10E-07	1.1E-08	191.634	4.83687	6.09E-07	3.74E-09	769.5	6.1	40.2	1.1
8	6.86E-07	4.2E-09	200.353	2.04886	6.51E-07	1.56E-09	784.4	2.4	39.2	0.4
9	1.07E-07	5.7E-10	201.378	1.76504	1.00E-07	2.08E-10	776.7	2.1	38.6	0.4
2	6.81E-07	6.1E-09	206.17	3.07555	5.97E-07	2.29E-09	784.6	3.5	38.1	0.6
7	6.80E-07	6.1E-09	205.259	2.99373	5.42E-07	2.18E-09	784.1	3.5	38.2	0.6
6	6.79E-07	7.0E-09	201.414	3.40681	6.10E-07	2.54E-09	782.7	4.0	38.9	0.7
3	6.83E-07	9.2E-09	206.98	5.02294	1.25E-06	4.17E-09	780.3	5.2	37.7	0.9
4	7.37E-07	2.5E-08	191.938	12.1043	3.21E-06	1.18E-08	753.1	12.7	39.2	2.6
5	6.70E-07	5.0E-08	204.949	30.2917	8.83E-06	2.79E-08	789.0	29.5	38.5	5.9

Table 37 : Results for Detector 1 & 2 (CPSD).

Run	Amplitude (/Hz)		Decay constant (s ⁻¹)		Constant (/Hz)		Delayed neutron fraction (pcm)		Generation time (μs)	
	Value	Uncer.	Value	Uncer.	Value	Uncer.	Value	Uncer.	Value	Uncer.
1	6.91E-07	7.20E-09	195.221	3.2518	3.03E-09	2.42E-09	780.0	4.1	40.0	0.4
8	6.86E-07	3.07E-09	198.604	1.44163	-4.27E-10	1.08E-09	784.2	1.8	39.5	0.2
9	1.06E-07	4.02E-10	200.376	1.23875	-1.99E-10	1.42E-10	781.0	1.5	39.0	0.2
2	6.84E-07	4.97E-09	200.329	2.40387	-4.29E-10	1.82E-09	783.1	2.8	39.1	0.3
7	6.83E-07	4.39E-09	199.893	2.10547	1.17E-09	1.58E-09	782.1	2.5	39.1	0.3
6	6.74E-07	5.13E-09	202.301	2.55885	3.26E-10	1.92E-09	785.2	3.0	38.8	0.3
3	6.85E-07	6.01E-09	204.937	3.14303	-1.05E-09	2.51E-09	780.0	3.4	38.1	0.4
4	6.82E-07	8.38E-09	197.619	4.31434	5.63E-09	3.58E-09	783.1	4.8	39.6	0.6
5	6.54E-07	1.32E-08	194.483	7.09929	1.58E-08	5.80E-09	798.8	8.1	41.1	0.9